University of Sussex

Optimisation of the Coupling of Ion Strings to an Optical Cavity

Stephen Patrick Begley

Submitted for the degree of Doctor of Philosophy

University of Sussex

September 2015

Declaration

I hereby declare that this thesis has not been and will not be submitted in whole or in part to another University for the award of any other degree.

Signature:

Stephen Patrick Begley

UNIVERSITY OF SUSSEX

Stephen Patrick Begley, Doctor of Philosophy

Optimisation of the Coupling of Ion Strings to an Optical Cavity

Summary

In this work, I detail the reconstruction and upgrades performed on the axial cavity ion trap in the ITCM group at the university of Sussex, and the measurement of the coupling of multiple ions to the cavity mode. This enables the optimal coupling between the ions and the cavity by adjusting the ions position in the radial and axial positions. This covers new ground in extending the optimal coupling beyond two ions which is of great importance for experiments with several ions in an optical cavity.

The thesis outlines the background theory of light-matter interaction and cavity QED, before describing the physical ion trap hardware and its assembly. A description of the laser and cavity systems is provided, including techniques for locking both to stable references. A number of novel measurement techniques for measuring and maximising the stability of the ions and cavities are presented, including micromotion minimisation, spectroscopy, magnetic field compensation using the ground state Hanle effect, and Raman spectroscopy. These techniques enable the measurement of crucial parameters of the atomic transitions and the cavity. The work culminates in a description of the optimisation of the coupling between ion strings and the cavity first by adjusting the radial trap position by means of variable capacitors attached to RF electrodes, and then axially by means of adjusting the endcap potentials and therefore the spacing between ions to obtain the greatest localisation while still positioning the ions close to the antinodes of the cavity field.

Acknowledgements

The work in this thesis has been carried out between October 2011 and September 2015 in the ITCM group at the University of Sussex, under the supervision of Dr. Matthias Keller and Prof. Wolfgang Lange. It has as its foundation the support and assistance of the ITCM and wider AMO group, and that of my family and friends.

I would like to thank Matthias for providing a constant source of direction, new ideas, and guidance. I would like to thank Professor Barry Garraway, my second supervisor, for his helpful advice and assistance in dealing with the administrative elements of the PhD. I would like to thank Nicolas Seymour-Smith and Dan Crick, who worked on this experiment before me and laid much of the groundwork for what is presented here. I gratefully thank Markus Vogt, my lab partner, who came up with many novel ideas and arrangements for experimental implementations. My thanks also go to the post-doctoral researchers closely associated with this experiment, Hiroki Takahashi and Gurpreet Kaur, whose theoretical insight and technical skill were a tremendous asset in the lab. I would like to thank Mr. Alan Butler, our chief mechanical engineer, whose surpassing skill will be sorely missed in the university upon his retirement and without whom none of the experimental designs implemented in the lab would be possible. My appreciation goes forth to all group members and students, past and present, who I have interacted with, for their friendship and assistance in the lab or in group meetings, including Andrew Riley-Watson, Lizzy Brama, Kevin Sheridan, Amy Gardner, Jack Morphew, Sahar Hejazi, William Groom, Ezra Kassa, and the many project students who spent time in the group. Finally I am thankful for the regrettably short time I had to work alongside Wolfgang. His knowledge and intellect were surpassed only by his sheer joy and enthusiasm for life and the experiment, and he is surely missed. May he rest in peace.

I would like to thank Regina, Stephen, Joseph, Gerard, Catherine and Cormac Begley for their love, encouragement, and support during my studies.

I am very grateful to all those friends I have made outside of my studies, whose friendship revitalised my energies and spurred me on to achieve all that I can. I include especially the University of Sussex Catholic Chaplaincy and Live Action Roleplaying Societies, and the Wellspring Community in Brighton.

I thank my fiancée Emma for her continual love, patience, and affection during the stressful times and the not-as-stressful times. I could not have dreamed of a more perfect partner with who to share all of life's endeavours.

Finally, I would like to thank the LORD God for creating such an amazing universe to inhabit and explore, and for giving us the capability and the means to appreciate the wonders of creation at the most fundamental levels. Thank you for the atoms and the light.

Contents

List of Tables

List of Figures

Chapter 1

Introduction

It has been a matter of intense theoretical and experimental interest since the late 20^{th} century to harness the power of quantum mechanics to supplement and expand the tremendous capabilities brought about by the valve and silicon chip as elements of the classical computer [1, 2]. While the speed, precision, and reproducibility of classical computational algorithms and their hardware implementations have enabled an explosion in technological growth, their relative lack of parallelism leaves several important problems intractable with even the most advanced hardware and software available today. *Quantum Information Processing* (QIP) renders certain important problems, like integer factorisation [3] and simulation of quantum systems [4, 5].

There are many candidate physical systems for the realisation of a functional, scalable quantum computer, including neutral atoms [6], Josephson junctions [7], quantum dots [8], and ions [11]. Each implementation has its strengths and weaknesses. The DiVincenzo criteria [12] have traditionally be considered to specify the properties necessary for a successful implementation. The system must possess well defined qubits which are initialisable, measurable, and have long coherence times. It must be possible to perform a *universal* set of operations upon these qubits; i.e. it must be possible to perform any QIP operation using a finite sequence of a subset of possible gates. If these systems are to be able to communicate with other systems, they must be able to convert between *stationary* and *flying* qubits, and it must be possible to controllably transmit these flying qubits between different locations.

We use a combined ion-photon system in the form of a high-finesse optical cavity positioned within a linear Paul trap. The ions and cavity are coupled to enable the interconversion between ionic and photonic qubits. Hence the system combines the long coherence times and easy state manipulation of the ions with the easy readout and transmission of

photonic qubits. Cavity Quantumelectrodynamics (cQED) is becoming an increasingly popular avenue for research into QIP [13], and the related field of Quantum Key Distribution (QKD) [14]. Their ease of coupling and long coherence times make cQED systems attractive quantum memories [9, 10], but they are also capable of being used as quantum information processors.

Most QIP schemes adopt the *circuit model* of quantum computation, in which the qubits are initialised as the degrees of freedom of a physical system, which are then acted upon by a series of unitary quantum gates until the operation is complete and the state can be read. Due to the unitary nature of these processes, they are entirely reversible up until the point of readout. We ultimately aim to make use of a different scheme known as *measurement-based* or *one-way* quantum computing. In such schemes [15], the act of measurement of a qubit can be used to feed-forward in the QIP process and affect how the remaining qubits are processed. Due to the wavefunction collapse involved in these schemes, they are not reversible. Rather than encoding the individual qubits in the degrees of freedom of a physical system, the measurement-based scheme operates on a large-scale entangled state or *cluster state* [16, 17]. Algorithms are implemented by performing measurements on individual nodes and feeding forward the results to further measurement operations [18]. The output can then be read from measurement qubits which hold the result of the algorithm upon its completion. Schemes for generating cluster states between large number of nodes are also being actively researched [19, 20]. While utilising a different paradigm for QIP, due to the factors mentioned above our system is also compatible with other processors of quantum information via the photon/cavity interface.

While the ion-trap cavity system possesses many strengths, it also presents unique challenges. While in neutral-atom cavity systems [21, 22] one cannot confine the atoms to as small a volume nor hold them within the cavity for periods of more than $\sim$ 1s, in ion traps the perturbation caused to the trapping potential by the dielectric cavity mirrors can prevent the ions being stably trapped. Traditional systems of this kind [23, 24] used as single photon sources have positioned cavities transverse to the ions, far from the trapping electrodes but with a small waist in order to achieve strong coupling with only one or two at a time using a small mode volume. We deal with this issue by placing the mirrors behind the DC endcap electrodes, shielding them from the trap potential. This also enables us to overlap many ions in a string with the cavity mode simultaneously. While our mode volume is larger due to the greater separation of the mirrors, the number of ions we couple to is also larger and the probabilistic measurement-based scheme we aim to use does not

require the system to be in the strong coupling regime.

Multiple ions have been coupled to cavities [25] to study the effects of coupling photons to the collective system of ions, but our implementation differs due to the ability to address individual ions and to ensure each ion is individually optimally coupled to the cavity. This enables us to implement effective interactions between ions using the measurement-based scheme, while still allowing us to approach the collective strong-coupling regime by coupling many ions to the cavity, with an effective ion number equal to the actual number of ions in the string.

The two-photon entanglement scheme has already been confirmed to work [26] in a transverse trap capable of entangling a single pair of ions. Our trap geometry and degree of control over the ion position and spacing allow us to simultaneously couple multiple ions in a string to the cavity mode without translating either the cavity or the ions during the experiment - an operation which would disturb the system and take a long time on experimental timescales. By having many ions coupled to the cavity, we aim to form large-scale entangled states that can be used to perform measurement-based quantum computations.

This chapter has provided some background and motivation for the work to be presented in this thesis. Chapter 2 presents the basic theory required to understand ion trapping and cavity Quantumelectrodynamics. Chapter 3 describes the trap hardware, electronics, and surrounding optics. Chapter 4 details the systems used to stabilise and control the lasers and cavities used to address load, cool, manipulate, and read out from the ions. The characterisation of and methods of optimisation of the ion trap parameters are described in chapter 5, and chapter 6 presents the methods used to ensure the optimal interaction between strings of trapped ions and the cavity mode. Conclusions and the outlook for future work are presented in chapter 7.

The work presented in this thesis resulted in the publication of

Optimized Multi-Ion Cavity Coupling, S. Begley, M. Vogt, G. Kaur Gulati, H. Takahashi, and M. Keller, *Phys. Rev. Lett.* 116, 223001 (2016).

Chapter 2

Theory

In this chapter, the basic theory underpinning the experimental setup and procedures will be described. I begin with an overview of ion trapping theory, followed by an explanation of the light-matter interactions involved in cooling and interrogating the ions. Optical cavities are first discussed from a classical perspective, before the fully quantum-mechanical cQED perspective is introduced. This chapter finishes with an overview of the quantum-mechanical schemes for single photon production and entanglement of ions which motivates this research and gives direction to future work to be carried out on this experiment.

2.1 Trapping theory

At the beginning of the 20^{th} century, the existence of the atom had not been conclusively proven, or universally accepted, and little was known about their internal structure. Since then, a number of techniques have been developed which allow individual atoms (or atomic ions) to be localised, decoupled from their environments, and coherently manipulated and observed. Such devices are referred to as atom or ion traps, of which there are several kinds; Penning traps [29], magneto-optical traps [30] and Paul traps [31] to name but a few. The Paul trap was developed by Wolfgang Paul in 1953. This work uses a linear Paul trap to confine atomic ions to a region of smaller than a half-wavelength of the experimental photons of interest. It consists of four parabolic electrodes defining the corners of a square at their tips and pointing toward the centre of the square such that maximum symmetry is achieved. A confining RF field is applied to either one opposing pair of electrodes while the other pair is held at ground (the *antisymmetric configuration*), or to both opposing pairs in antiphase (the *symmetric configuration*). A pair of DC electrodes at either end of axial

extent of the parabolic electrodes provide an axial confining potential. The configuration allows for a high degree of control over an ion or string of ions with a trapping time of several hours. It is shown in figure 2.1.

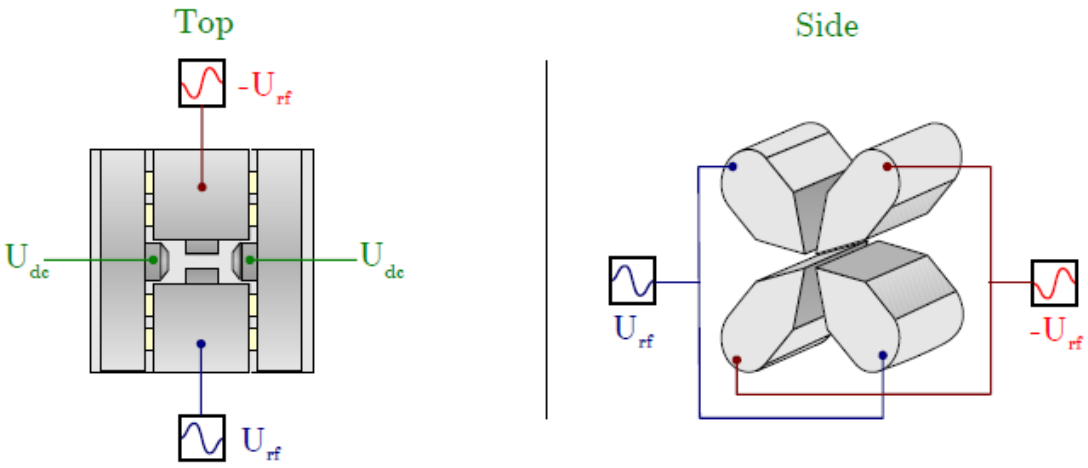

Figure 2.1: A schematic of a Paul trap in the symmetric configuration. The top view shows the DC endcaps and RF electrode superstructure, the side view shows only the tips of the RF electrodes at the trapping region. [46].

Earnshaw's theorem states that a collection of point charges cannot be maintained in a stable stationary equilibrium configuration solely by the electrostatic interaction of the charges in three dimensions [32]. This is a result of Gauss' law, which states that the divergence of an electric field is 0 in free space. If the field arises from a potential U, we obtain Laplace's equation $\nabla^2 U = 0$. This implies that there can be no local minimum of a field in free space, only saddle points which provide unstable equilibrium.

In order to get around this restriction, we apply a time-varying field to the parabolic electrodes, which varies on timescales much shorter than the motional timescales of the ion so the ion sees an averaged-out *pseudopotential* which is confining in the radial direction. The axial confinement is supplied by a repulsive static DC potential.

The alternating potential applied to the parabolic electrodes is given by

$$U(t) = \pm\frac{1}{2}U_{RF}\cos\left(\Omega_{RF}\cdot t\right), \tag{2.1}$$

where U_{RF} is the peak to peak amplitude, Ω_{RF} is the angular frequency and t is time and the two sets of opposite electrodes oscillate in antiphase. For parabolic electrodes with static DC endcap potentials, close to the trap centre we obtain the following potential:

$$U(x,y,t) = -\frac{1}{2}U_{RF}\cdot\cos\left(\Omega_{RF}\cdot t\right)\cdot\left[\frac{(x^2-y^2)}{r_0^2}\right] + \frac{1}{2}\eta U_{DC}\left[\frac{(x^2+y^2)}{z_0^2}\right], \tag{2.2}$$

where r_0 refers to the distance between each RF electrode and the trap centre and defines the radius of the trap, and the second term comes from the DC potential and is anti-trapping. U_{DC} is the DC endcap voltage, η is a geometry-dependant scaling factor, and z_0 is the distance between the endcap electrode and the ion. The axial confinement is given by the static DC potential of the endcap electrodes, and is simply

$$\phi(z) = -\eta U_{DC} \frac{z^2}{z_0^2}. \tag{2.3}$$

Using these potentials, we can now develop the equations of motion for a particle of mass $m(= m_{\mathrm{Ca}}$ for consistency) and charge Q. In the x (and equivalently y) direction:

$$F = m_{\mathrm{Ca}}\ddot{x}, \tag{2.4}$$

$$-Q\frac{\partial U(x,t)}{\partial x} = m_{\mathrm{Ca}}\ddot{x}, \tag{2.5}$$

into which we substitute $\tau = \frac{\Omega_{RF}t}{2}$ to give:

$$\frac{d^2x}{d\tau^2} + \frac{4Q}{m_{\mathrm{Ca}}\Omega_{rf}^2}\frac{\partial U(x,t)}{\partial x} = 0. \tag{2.6}$$

Substituting:

$$q = \frac{2QU_{RF}}{m_{\mathrm{Ca}}\Omega^2 r_0^2} \text{ and} \tag{2.7}$$

$$a = \frac{-4\eta QU_{DC}}{m_{\mathrm{Ca}}\Omega_{rf}^2 z_0^2}, \tag{2.8}$$

we obtain

$$\frac{d^2x}{d\tau^2} + (a - 2q\cos(2\tau))x = 0. \tag{2.9}$$

Similarly in the y direction we obtain

$$\frac{d^2y}{d\tau^2} + (a + 2q\cos(2\tau))y = 0. \tag{2.10}$$

The above equations have the form of a Mathieu equation, which is a Hill equation [33] with just a single harmonic mode. The Mathieu equation has stable solutions for differential equations which are separable in elliptical cylindrical coordinates and a range of q and a values as shown by the shaded areas in figure 2.2. These stable solutions correspond to situations in which the ion is stably confined within the trap. For $a \ll q \ll 1$ as is typically the case in linear Paul traps, the solutions may be approximated by

$$x(t) = (1 - q\cos\Omega_{RF}t) \cdot \cos\left[x_0\cos(\omega_r t) + x_{DC}\right], \tag{2.11}$$

$$y(t) = (1 - q\cos\Omega_{RF}t) \cdot \cos\left[y_0\cos(\omega_r t) + y_{DC}\right], \tag{2.12}$$

where x_0 and y_0 are the amplitudes of motion, x_{DC} and y_{DC} represent offsets from the trap centre and ω_r is the radial oscillation frequency or radial *secular frequency* and is given by

$$\omega_r = \frac{\sqrt{\frac{q^2}{2} + a}}{2} \cdot \Omega_{RF}. \tag{2.13}$$

The secular frequency is proportional to the other characteristic frequency seen in equa-

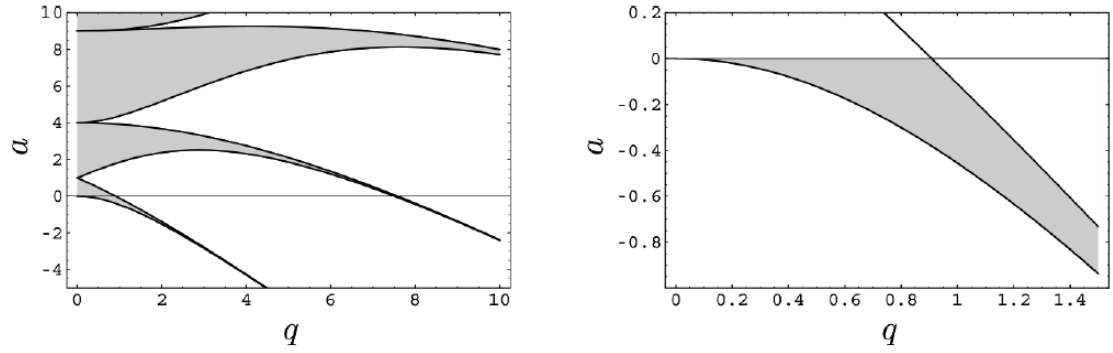

Figure 2.2: The stable regions of the Mathieu equations. In ion trapping applications, we are generally interested in a very small a and $q \leq 1$ [46].

tions 2.11 and 2.12, the RF trapping frequency. We note in these equations that there is a constant term, and a term proportional to the driven motion at the trap frequency. This second term describes the ion's *micromotion* which provides an additional contribution to the ion's temperature. It is possible to minimise this micromotion to an unremovable component by reducing x_{DC} and y_{DC} to 0.

Axially, the confinement is simply given by equation 2.3, which straightforwardly produces the equation of motion

$$\ddot{z} + \frac{a}{2}\Omega_{RF}^2 = 0, \tag{2.14}$$

with solution

$$z(t) = z_0 cos(\omega_z t), \tag{2.15}$$

$$\text{with } \omega_z = \sqrt{\frac{-a}{2}}\Omega_{RF}. \tag{2.16}$$

In the pseudopotential approximation, we average the micromotion term in equations 2.11 and 2.12 to 0 over many periods, giving a three-dimensional potential

$$\Phi(x, y, z) = \frac{1}{2} m_{\mathrm{Ca}} \left(\omega_r^2(x^2 + y^2) + \omega_z^2(z^2)\right), \tag{2.17}$$

which is that of a 3D harmonic potential well with secular frequency ω_r in the radial direction and ω_z in the axial direction for a particle of mass m_{Ca}.

2.2 Light-Matter Interactions

Before discussing the laser schemes used in the experiment, it will be helpful to establish the fundamentals of light-matter interactions. All ion trapping and cQED phenomena emerge from the relatively simple laws underpinning the interaction between ions and time-varying electric fields.

2.2.1 Scattering Theory

We model our atom as a closed two-level system consisting of a pair of non-degenerate energy levels with energies $\hbar\omega_1$ and $\hbar\omega_2$ respectively. The system is driven by a laser of frequency $\hbar\omega$. The Hamiltonian of the two-level system is:

$$H_0 = \hbar\omega_1 |1\rangle \langle 1| + \hbar\omega_2 |2\rangle \langle 2| . \tag{2.18}$$

The interaction between the two-level system and the laser can be described in a semi-classical model as:

$$H_I = (\hat{\sigma}_+ + \hat{\sigma}_-)\mu_{12}E, \tag{2.19}$$

where $\hat{\sigma}_\pm$ are the raising and lowering operators($|1\rangle \langle 2|$ and $|2\rangle \langle 1|$), μ_{12} is the atomic dipole transition element for our system, and E is the electric field of the laser beam. It is given by

$$E = E_0 \cdot \frac{\left(e^{-i\omega t} + e^{+i\omega t}\right)}{2}, \tag{2.20}$$

where E_0 is a constant and ω is the frequency. Substituting this into eq. (2.19) we obtain

$$H_I = (\hat{\sigma}_+ + \hat{\sigma}_-)(e^{-i\omega t} + e^{+i\omega t})\mu_{12}\frac{E_0}{2}, \tag{2.21}$$

$$= \frac{\hbar\Omega}{2}(\hat{\sigma}_+ + \hat{\sigma}_-)(e^{-i\omega t} + e^{+i\omega t}), \tag{2.22}$$

where $\Omega = \mu_{12}.E_0/\hbar$ is the Rabi frequency of the transition. Changing to the interaction picture and applying the rotating wave approximation, we obtain

$$H_I = \frac{\hbar\Omega}{2}(\hat{\sigma}_+ e^{-i\delta t} + \hat{\sigma}_- + e^{+i\delta t}), \tag{2.23}$$

with $\delta = \omega - \omega_{12}$. Putting this all together, we obtain the general Hamiltonian for a driven two-level system without dissipation:

$$H = H_0 + H_I \tag{2.24}$$

$$= \hbar\omega_1 |1\rangle \langle 1| + \hbar\omega_2 |2\rangle \langle 2| + \frac{\hbar\Omega}{2}(\hat{\sigma}_+ e^{-i\delta t} + \hat{\sigma}_- e^{+i\delta t}). \tag{2.25}$$

Assuming our two-level system begins in a pure state with normalised amplitudes $C_1(t)$ and $C_2(t)$, we can express the state of the system as:

$$|\Psi\rangle = C_1(t)\,|1\rangle + C_1(t)\,|2\rangle\,. \tag{2.26}$$

Putting this into Schrödinger's equation with the Hamiltonian defined in (2.24) we obtain the relations

$$\frac{d}{dt}C_1(t) = -i\omega_1 C_1(t) + \frac{i\omega}{2}e^{i\omega t}C_2, \tag{2.27}$$
$$\frac{d}{dt}C_2(t) = -i\omega_2 C_2(t) + \frac{i\omega}{2}e^{i\omega t}C_1, \tag{2.28}$$

where the first term is the normal phase evolution of a state with energy $\hbar\omega_{1,2}$ and the second term is the driven oscillation between the states. We can obtain the time-evolution of the density matrix ρ without spontaneous decay by noting the relations

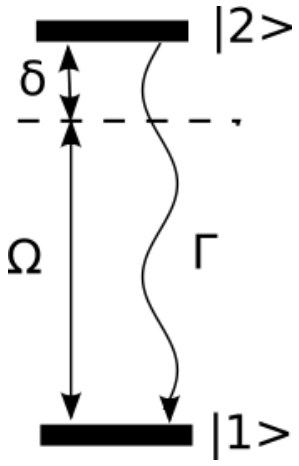

Figure 2.3: A two-level atomic system consisting of ground state $|1\rangle$ and excited state $|2\rangle$ interacting with a classical electromagnetic wave detuned from resonance by δ. Ω is the Rabi frequency of the dipole transition and Γ is the spontaneous decay rate from the excited state.

$$\rho_{x,x} = |C_x(t)|^2, \tag{2.29}$$
$$\rho_{x,y} = C_x(t)C_y^*(t), \tag{2.30}$$

where x and y may represent 1 or 2. Using eqs. (2.27) we obtain

$$\frac{d}{dt}\rho_{22} = -\frac{d}{dt}\rho_{11} = \frac{i\Omega}{2}(e^{(-i\omega t)}\rho_{21} - e^{(i\omega t)}\rho_{12}), \tag{2.31}$$
$$\frac{d}{dt}\rho_{21} = \frac{d}{dt}\rho_{12}^* = -i\omega_{21}\rho_{21} + \frac{i\Omega}{2}e^{(-i\omega t)}(\rho_{11} - \rho_{22}). \tag{2.32}$$

However, this is not a complete description of the system as in reality it also contains a dissipative decay through spontaneous emission. In order to fully describe the system, we must use the density matrix evolution relation adding the spontaneous decay rate $\Gamma = \frac{\omega_{12}^3\mu_{12}^2}{\pi\epsilon_0\hbar c^3}$.

A schematic of a 2-level system with spontaneous emission is shown in figure 2.3. It is a simple matter to add a decay from $|2\rangle$ to $|1\rangle$ at rate Γ to obtain

$$\frac{d}{dt}\rho_{22} = -\Gamma\rho_{22} + \frac{i\Omega}{2}(e^{-i\omega t}\rho_{12} - e^{i\omega t}\rho_{21}), \tag{2.33}$$
$$\frac{d}{dt}\rho_{11} = +\Gamma\rho_{22} + \frac{i\Omega}{2}(e^{-i\omega t}\rho_{21} - e^{i\omega t}\rho_{12}), \tag{2.34}$$
$$\frac{d}{dt}\rho_{21} = -(i\omega_{21} + \frac{\Gamma}{2})\rho_{21} + \frac{i\Omega}{2}e^{-i\omega t}(\rho_{22} - \rho_{11}). \tag{2.35}$$

These equations are known as the optical Bloch equations [37] for a two level system. The Bloch equations may be rewritten substituting $\rho' = \rho_{12}e^{i\omega t} = \rho_{21}^* e^{-i\omega t}$.

$$\frac{d\rho_{22}}{dt} = -\frac{d}{dt}\rho_{11} \tag{2.36}$$

$$= -\Gamma(\rho_{22}) + i\frac{\Omega}{2}(\rho'^* - \rho'), \tag{2.37}$$

$$\frac{d\rho'}{dt} = \left(i\delta - \frac{\Gamma}{2}\right)\rho' - \frac{i\Omega}{2}\left(\rho_{11} - \rho_{22}\right). \tag{2.38}$$

In the steady-state $\frac{dw}{dt} = \frac{d\rho'}{dt} = 0$, these equations give us:

$$-\Gamma\left(\rho_{11} - \rho_{22}\right) + i\Omega(\rho'^* - \rho') = \Gamma \qquad \text{and} \tag{2.39}$$

$$\left(i\delta - \frac{\Gamma}{2}\right)\rho' = \frac{i\Omega}{2}\left(\rho_{11} - \rho_{22}\right). \tag{2.40}$$

Remembering that $\rho_{11} = 1 - \rho_{22}$ and defining the saturation parameter s as

$$s = \frac{2\Omega^2}{\Gamma^2}, \tag{2.41}$$

the solutions to the above equations are:

$$\rho_{22} = \frac{s_0/2}{1 + s_0 + 4\left(\delta/\Gamma\right)^2} \tag{2.42}$$

$$\rho' = \frac{i\Omega}{2\left(\Gamma/2 - i\delta)(1 + \frac{s}{1+4(\delta/\Gamma)^2}\right)}. \tag{2.43}$$

The saturation parameter s can also be expressed as $s = I/I_{\text{sat}}$, where I is the laser intensity and $I_0 = \frac{4\pi^2\hbar c\Gamma}{\lambda^3}$ is the saturation intensity, at which the transition becomes saturated [34, 35]. The scattering rate Γ_s of a single ion is equal to the upper state population times the spontaneous decay rate:

$$\Gamma_s = \Gamma \cdot \frac{s_0/2}{1 + s_0 + 4\left(\delta/\Gamma\right)^2}. \tag{2.44}$$

For large s and $\delta = 0$, the scattering rate saturates to $\frac{\Gamma}{2}$, in keeping with the expectation at high above saturation the populations of a 2-level system become equal. For a constant s, the fluorescence rate is a Lorentzian function of the laser detuning δ, as we expect for atomic spectra of 2-level transitions. For a constant δ, the fluorescence broadens as s is increased, an effect known as *power broadening*. This may be seen more clearly by rewriting 2.44 as

$$\Gamma_s = \frac{s}{1+s}\frac{\Gamma/2}{1 + 4\left(\delta/\Gamma'\right)^2}, \tag{2.45}$$

$$\text{with } \Gamma' = \Gamma\sqrt{1+s}. \tag{2.46}$$

The effective linewidth Γ' becomes wider the greater the power incident on the atom. This is relevant when it comes to cooling the ion, as we shall see in the next section, as the cooling rate is proportional to the slope of 2.44. The effect of power broadening is illustrated in figure 2.4.

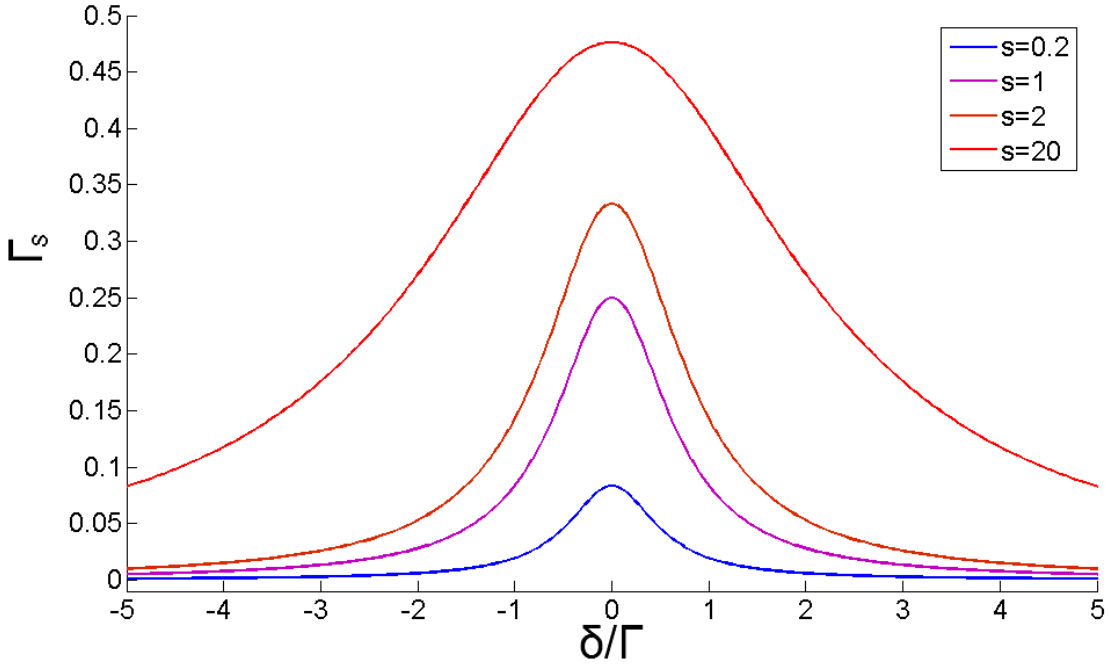

Figure 2.4: Variation in the lineshape of a 2-level transition for incident intensity below, at, and above the saturation intensity.

2.2.2 Doppler Cooling

Ions held in a trap will not remain there indefinitely - they are confined in a potential of finite depth, and are constantly being given energy by collisions with background atoms and heating from the trap electrodes and driven micromotion. Once the thermal energy of the ion exceeds the trap depth, it will leave the trapping region and be lost. The ion must be constantly cooled to ensure it remains well localised, and also that its transitions are not thermally broadened. We utilise Doppler cooling to maintain the ion's temperature at sub-milliKelvin levels.

When a photon absorbs an ion from a laser, it receives a momentum kick of $\mathbf{\Delta p} = \hbar\mathbf{k}$, where $\mathbf{k}$ is along the direction of the laser. For an ion moving with velocity $\mathbf{v}$and a laser

of detuning detuning δ, the scattering force experienced by the ion can be expressed as

$$\mathbf{F}(\delta + \mathbf{k}\cdot\mathbf{v}) = \mathbf{\Delta p}\Gamma_s, \tag{2.47}$$

$$= \hbar\mathbf{k}\Gamma_s, \tag{2.48}$$

$$= \frac{\hbar\mathbf{k}\Gamma}{2}\cdot\frac{s_0}{1+s_0+4\left(\frac{\delta+\mathbf{v}\cdot\mathbf{k}}{\Gamma}\right)^2}. \tag{2.49}$$

This results in a force on the atom in the direction of the laser beam, which can be used to slow the atom's motion. In an atomic trap, which has weaker confinement, in order to slow the atom's motion in both the $\pm\mathbf{k}$ directions, a second counterpropagating laser is added to provide a cooling force in the opposite direction. In ion traps, the ion oscillates at the secular frequency on timescales orders of magnitude shorter than the absorption and emission timescales, and so a single laser in a given direction can be treated as a pair of counter-propagating lasers from the ion's perspective.

The amplitude of the scattering force experienced by an ion in a trap illuminated by a laser of detuning δ is given by

$$F_{\text{scatt}} = F(\delta - kv) - F(\delta + kv), \tag{2.50}$$

$$\approx F(\delta) - kv\frac{\partial F}{\partial\omega} - \left[F(\delta) + kv\frac{\partial F}{\partial\omega}\right], \tag{2.51}$$

$$= -2\frac{\partial F}{\partial\omega}kv, \tag{2.52}$$

$$= -\beta v, \tag{2.53}$$

where v is the component of the velocity along the last direction and is taken to be small. F_{scatt} describes a frictional force acting on the atom with a coefficient of damping β, which from 2.48 can be expanded as follows:

$$\beta = 2k\frac{\partial F}{\partial\omega}, \tag{2.54}$$

$$= 2k\frac{\hbar}{c}\left(\Gamma_s + \omega\frac{\partial\Gamma_s}{\partial\omega}\right). \tag{2.55}$$

The first term here is proportional to Γ_s, while the second is proportional to ω, typically eight orders of magnitude larger. Neglecting the first term, we conclude

$$\beta \sim 2\hbar k^2\frac{\partial\Gamma_s}{\partial\omega}, \tag{2.56}$$

$$= \left(\frac{16\delta}{\Gamma^2}\right)\cdot\left(\frac{-1}{1+s_0+4\left(\frac{\delta}{\Gamma}\right)^2}\right)\cdot\frac{\Gamma_s s_0}{2}\hbar k^2, \tag{2.57}$$

$$= -8\hbar k^2\frac{\delta}{\Gamma}\cdot\frac{s_0}{\left[1+s_0+4\left(\frac{\delta}{\Gamma}\right)^2\right]^2}. \tag{2.58}$$

The cooling rate of the atom's motion along the laser's direction can be expressed as

$$\left(\frac{dE}{dt}\right)\Big|_{\text{cooling}} = F_{\text{scatt}} v, \tag{2.59}$$

$$= -\beta v^2. \tag{2.60}$$

Equation (2.59) implies that the temperature of a Doppler-cooled ion may decrease monotonically to zero, but we have not yet accounted for heating of the ion. Even without taking into consideration the heating effects of the RF potential, the ion's minimum temperature is limited by the stochastic nature of the scattering process.

The total force an ion undergoing scattering experiences may be expressed as the sum of the absorption and spontaneous emission contributions, as follows:

$$\mathbf{F}_{\text{total}} = \mathbf{F}_{\text{abs}} + \delta\mathbf{F}_{\text{abs}} + \mathbf{F}_{\text{emit}} + \delta\mathbf{F}_{\text{emit}}, \tag{2.61}$$

where $\mathbf{F}_{\text{total}}$ refers to the total force, $\mathbf{F}_{\text{abs}}$ to the average force resulting from the absorption of photons, $\mathbf{F}_{\text{emit}}$ refers to the average force experienced as the result of spontaneous emission, δ pertains to the fluctuations in these forces, and we once again consider the forces as vectors in three dimensions.

Assuming that emission is isotropic, the net force arising from spontaneous emission averages to zero; $\mathbf{F}_{\text{emit}=0}$. However, as each emission results in a momentum kick in a random momentum, the particle's momentum under the influence of spontaneous emission alone follows a random walk in momentum space. Following a period of time t, the ion's velocity increases as

$$|\mathbf{v_z}|^2_{\text{emit}} = \eta v_r^2 \Gamma_s t, \tag{2.62}$$

where $\mathbf{v_z}$ refers to the ion's velocity in one dimension, v_r is the recoil velocity from a single emission, and η is a geometric factor equal to $\frac{1}{3}$ for isotropic emission in three dimensions. This expression describes the effect of the $\delta\mathbf{F}_{\text{emit}}$ term.

$\delta\mathbf{F}_{\text{abs}}$ can be accounted for by noting that the rate of absorption of photons from the laser is not constant, but follows Poissonian statistics. This produces a 1-dimensional random walk in momentum space along the laser direction, yielding an increase in ion velocity of

$$|\mathbf{v_z}|^2_{\text{abs}} = v_r^2 \Gamma_s t. \tag{2.63}$$

Therefore the total heating rate of the ion due to stochastic fluctuations is given by:

$$\left(\frac{dE}{dt}\right)\Big|_{\text{heating}} = (\eta + 1)\frac{m_{\text{Ca}}}{2} v_r^2 \Gamma_s t, \tag{2.64}$$

$$= \left(\frac{1+\eta}{2}\right)\left(\frac{\hbar k}{m_{\text{Ca}}}\right)^2 m_{\text{Ca}} \Gamma_s t, \tag{2.65}$$

as $v_r = \hbar k/m_{\mathrm{Ca}}$. In an isotropic atomic trap cooling may be applied by lasers in three orthogonal directions to achieve 3D cooling. The ion tap potential is not perfectly symmetric in any dimension, so with a single laser at an angle to the principal trap axes 3D cooling may be achieved. This corresponds to a tripling of the η factor, producing a factor of $(1+3\eta) = 2$. In addition, as described above a single laser cooling a trapped ion may be treated as equivalent to two counter-propagating lasers cooling a trapped atom, producing an effective doubling of the scattering rate, and so:

$$\left(\frac{dE}{dt}\right)\Big|_{\mathrm{heating}} = 2\frac{(\hbar k)^2\Gamma_s}{m_{\mathrm{Ca}}}. \tag{2.66}$$

The cooling rate constant β is dependent on both the detuning and power of the cooling beam. Figure 2.5 illustrates the impact of varying both parameters on β. We can observe that β is maximal at $\delta = -\Gamma/2$ from resonance and at saturation intensity. At $\delta = +\Gamma/2$ the heating of the ion due to the laser is largest - fast moving ions will be more likely to absorb photons travelling in the same direction and hence acquire more energy. At $\delta = 0$, on resonance, there is no net cooling. As the saturation parameter s increases, cooling and heating rates both decrease as power broadening decreases the slope of the Lorentzian linewidth which according to (2.54) will decrease the amplitude of β.

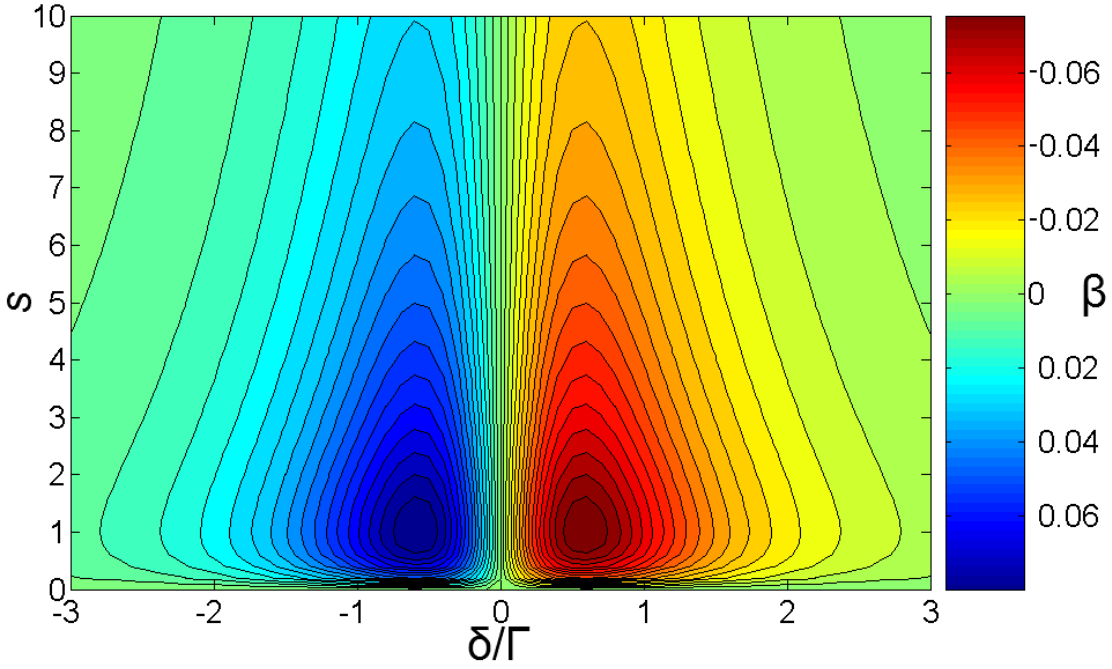

Figure 2.5: The variation in the cooling rate constant β with detuning δ and saturation parameter s.

In equilibrium, $\left(\frac{dE}{dt}\right)\Big|_{\text{cooling}} + \left(\frac{dE}{dt}\right)\Big|_{\text{heating}} = 0$ and so

$$\beta v^2 = 2\frac{(\hbar k)^2\Gamma_s}{m_{\text{Ca}}}, \tag{2.67}$$

$$v^2 = 2\frac{(\hbar k)^2\Gamma_s}{\beta m_{\text{Ca}}}; \tag{2.68}$$

$$k_B T = \frac{1}{2}m_{\text{Ca}}v^2 = \frac{(\hbar k)^2\Gamma_s}{\beta}, \tag{2.69}$$

$$= \hbar\frac{\Gamma^2\left(1 + s_0 + 4(\frac{\delta}{\Gamma})^2\right)}{8\delta}. \tag{2.70}$$

This function is minimised with $\delta = \Gamma/2$ and $s_0 \to 0$, giving the minimum achievable temperature, known as the Doppler Temperature, as

$$T_D = \frac{\hbar\Gamma}{2k_B}. \tag{2.71}$$

2.3 Cavity QED

Quantum Electrodynamics - QED - refers to the study of the interactions of charged particles and photons in the quantum limit. Cavity QED (cQED) refers to the specific case where a resonant cavity is placed around the system. The cavity consists of a pair of conductors (or dielectrics) which define boundary conditions for the electric field. The presence of a cavity introduces much interesting physics and renders the quantumelectrodynamical behaviours of the system more readily measurable in the lab. In our experiment, the cQED environment is realised as a system of trapped ions located at the antinodes of an optical cavity tuned into resonance with one of the ion's optical transitions.

2.3.1 Optical Cavities

An optical cavity can refer to any system of mirrors which supports standing waves of electromagnetic radiation. For QIP applications, one mirror typically has a slightly lower reflectivity to act as the "output" mirror of the cavity through which most light leaves. The intensity distribution of light within a resonant cavity is referred to as a cavity mode. A cavity may support many modes of different spatial distributions for light of a given wavelength, as long as they satisfy the boundary conditions given by the cavity mirrors. There are also several different classes of cavity exhibiting different behaviours. The simplest arrangement of mirrors is a pair of plane mirrors oriented parallel to each other and tuned such that there is a whole number of half-wavelengths between them.

In order to obtain optimal coupling between the light and an atom in the experiment, it is desirable for the photon to undergo the maximum number of round trips possible

before it leaves the cavity, and for the supported modes to narrow at the centre of the cavity, in order to maximise the mode density in this region to achieve optimal atom-light coupling. For these reasons, in our experiment the cavity is formed of two hemi-spherical dielectric mirrors of radius of curvature 1 cm, and a cavity length of 5.25 mm. The resulting longitudinal mode is of the form of a focussed Gaussian beam with diffraction-limited cavity waist w_0 at the cavity centre, as shown in figure 2.6.

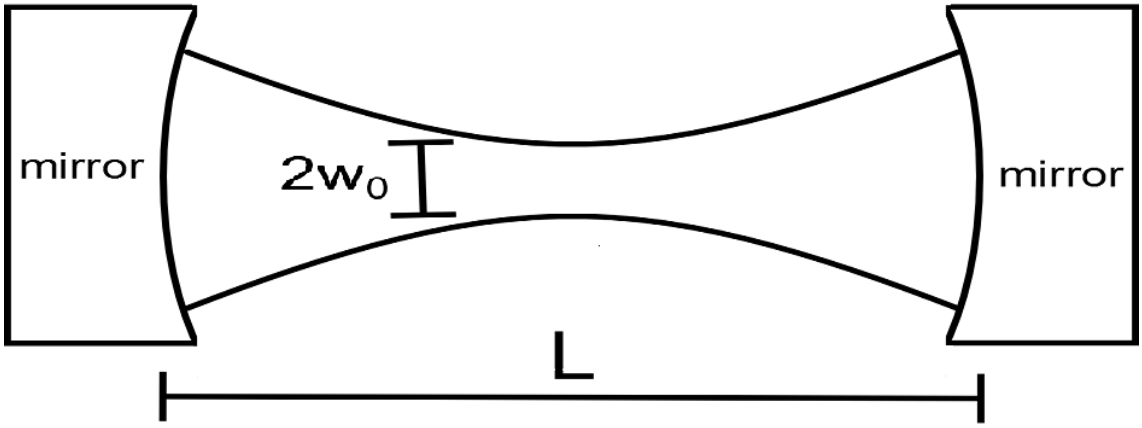

Figure 2.6: The longitudinal profile of a cavity mode with cavity length L and waist w_0.

The modes supported by our cavity are Hermite-Gaussian modes, with a spatial distribution which can be described by the following equations:

$$E_{n,m}(x,y,z) = E_0 \Psi_n(x,y)\Psi_m(x,y)\Phi(z), \tag{2.72}$$

where the Ψ functions refer to the *transverse* modes, and $\Phi(z)$ refers to the longitudinal mode. In theory, for perfectly symmetrical mirrors, the $\Psi_n(x,z)$ and $\Psi_m(y,z)$ modes would be degenerate in n and m and always be excited simultaneously; in practise small imperfections lead to the $\Psi(x)$ and $\Psi(y)$ transverse modes being slightly non-degenerate and therefore capable of being excited separately. The transverse functions are described as:

$$\Psi_n(v,z) = \sqrt{\frac{w_0}{w(z)}} H_n\left(\frac{\sqrt{2}}{w(z)}\exp\left(-\frac{v^2}{w(z)^2}\right)\right), \tag{2.73}$$

where v represents x or y, H_n is the Hermite polynomial of order n and $w(z)$ is the cavity-mode waist (the radial distance from the centre of the mode to where the mode density drops to $\frac{1}{e^2}$ of its maximum value) at a given coordinate and w_0 is the minimum waist of the mode. $w(z) = w_0\sqrt{1+\left(\frac{z}{z_R}\right)^2}$, where z_R is the Rayleigh range, the longitudinal distance over which the beam waist doubles, given by $z_r = \frac{\pi w_0}{\lambda}$. Figure 2.7 [46] illustrates the lowest-order accessible modes, though high-order modes with many nodes and more

complex structures can be readily observed by adjusting the coupling of the input light to the cavity.

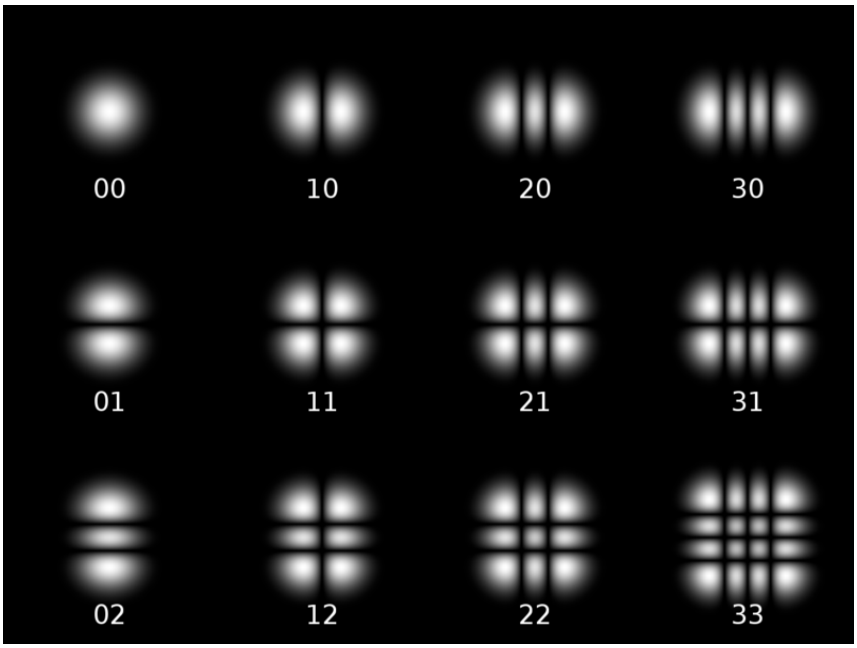

Figure 2.7: Low-order Hermite-Gaussian Modes. [46]. These modes are usually labelled by a pair of numbers, which refer to the number of nodal planes crossing the orthogonal horizontal and vertical axes.

Longitudinally, the boundary condition imposed by the cavity mirrors is that the phase acquired by the light on a round trip through the cavity must be an integer multiple of 2π; any other phase leads to complete destructive interference. The phase of the lightfield varies with the longitudinal coordinate within the cavity, and on the n and m numbers describing the transverse mode. The longitudinal field can be expressed as

$$E(x,y,z) = \sin\left(kz - (1+n+m)\arctan\frac{z}{z_r} + \frac{k(x^2+y^2)}{2R(z)}\right), \tag{2.74}$$

where $k = \frac{2\pi}{\lambda}$ and $R(z)$ is the wavefront curvature at a specified z coordinate, given by $R(z) = z\left[1 + \left(\frac{z_R}{z}\right)^2\right]$.

For our experiments, we are concerned only with the lowest-order transverse mode, the TEM_{00} mode with a simple Gaussian intensity distribution. We use this mode because it features a maximum in the centre, and has the smallest mode-volume (and therefore intensity at the centre) of all Hermite-Gaussian modes. The mathematical form of our mode of interest is therefore:

$$\Psi_{\mathrm{TEM00}}(x,y,z) = \frac{w_0}{w(z)}\exp\left(-\frac{x^2+y^2}{w(z)^2}\right)\sin\left(kz - \arctan\left[\frac{z}{z_r}\right] + \frac{k(x^2+y^2)}{2R(z)}\right). \tag{2.75}$$

2.3.2 Cavity Parameters

Cavity QED systems are usually described in terms of three parameters:

- g - the strength of the coupling between the cavity field and the atom. It is proportional to the mode function: $g = g_0\Psi(x, y, z)$.
- Γ - the rate of loss of photons by emission from the atom into channels other than the cavity mode, i.e. spontaneous decay.
- κ - the rate of loss of photons by dissipation or transmission through the cavity mirrors.

These quantities are usually referred to in units of radians per second. Other relevant parameters include:

- The cavity length, l.
- The free-spectral range (FSR), which is the difference in frequency between equivalent longitudinal modes of the cavity. It can be obtained from the cavity length by applying FSR $= \frac{c}{2l}$, where c is the speed of light in the cavity medium.
- The finesse $\mathcal{F}$, which is the average number of round trips a cavity photon will make before leaving the cavity. It is dependent on the reflectivities of the cavity mirrors R_1 and R_2 in the following way: $\mathcal{F} \approx \frac{\pi(R_1R_2)^{1/4}}{(R_1R_2)^{1/2}}$. It can also be obtained from κ and l or the FSR: $\mathcal{F} = \frac{\pi c}{2l\kappa} = \frac{\pi.\text{FSR}}{\kappa}$.
- The cooperativity, which can be thought of as the ratio of the coupling to the losses, and is dependent on the atomic component of the cQED system as well as the cavity. It is given by $C_0 = \frac{g^2}{\kappa\Gamma}$.

We can refer to regimes in which one or more of g, κ or Γ dominate the dynamics. In the limit of $g >> \Gamma, \kappa$, the *strong coupling regime*, the loss terms are negligible and the system behaviour is dominated by the oscillatory excitation exchange between the cavity and the atom. The *bad cavity regime* is defined as that in which $\kappa >> g >> \Gamma$. In this regime photons are likely to be emitted from the atom into the cavity mode, but are not likely to undergo the reverse process before leaving the cavity. Assuming κ is mostly due to the loss of photons by transmission from the mirror and not dissipative losses, this is the regime interesting to us - in the case of the measurements and goals of this thesis, absorption of a photon from the cavity mode by the ion is highly undesirable, but transmission and

collection of the emitted photons is desirable. We require only that $\kappa \sim O(g)$. As $\kappa \propto l^{-1}$ and $g \propto l^{-3/4}$, a compromise must be found when designing the cavity. κ is fixed and g is limited by our mirror substrates and geometry. Spontaneous emission out of the cavity mode leads to a loss of coherence, therefore to $g \gg \Gamma$. In order to approach the regime of interest, we must maximise the ratio of g/Γ. This can be achieved by detuning the cavity from the atomic resonance. From (2.44), we can see that for large detunings δ :

$$\frac{\Gamma_s}{\Gamma} \propto \left(\frac{\Omega}{2\delta}\right)^2, \tag{2.76}$$

where Ω is the Rabi frequency of the pump transition used to drive the Raman process. The effective g factor decreases with detuning[39, 40] as

$$g_{\text{eff}} \propto \frac{\Omega}{2\delta}, \tag{2.77}$$

so we can increase the g/Γ ratio by a factor of δ. In principal, this ratio could be made arbitrarily high, however the dynamics of the system would become very slow.

2.3.3 Atoms in Cavities - The Jaynes-Cummings model

The Jaynes-Cummings model describes the interaction of a two-level system with the mode of an optical cavity. It is an extremely powerful tool for describing the dynamics of cQED systems involving both atoms and cavities. We will describe it briefly here.

The Jaynes-Cummings Hamiltonian involves three contributions: the Hamiltonian of the atom, $\hat{H_a} = \hbar\omega_a\hat{\sigma}_+\hat{\sigma}_-$, where $\hat{\sigma}_\pm$ are the atomic raising and lowering operators and ω_a described the energy difference between states; the Hamiltonian of the lightfield, $\hat{H_f} = \hbar\omega_c\hat{a}^\dagger\hat{a}$, where $\hat{a}^\dagger$ and $\hat{a}$ define the cavity photon creation and annihilation operators and ω_c describes the frequency of the single photon cavity field; and finally the interaction Hamiltonian $\hat{H_i} = \hbar g(\hat{\sigma}_+ + \hat{\sigma}_-)(\hat{a}^\dagger + \hat{a})$, where g is the ion-cavity coupling strength described in section 2.3.2 and $g = g_o\Psi(x, y, z)$ where $g_0 = \sqrt{\frac{\mu_{ab}\omega_c}{2\hbar\epsilon_0 V}}$ and $V = \int_0^\infty \Psi(\mathbf{r}, z)dV$ is the mode volume. We have set the zero-point energy to 0 and μ_{ab} is the dipole matrix element for the transition between levels a and b.

$$\hat{H}_{JC} = \hat{H}_a + \hat{H}_f + \hat{H}_i, \tag{2.78}$$

$$= \hbar\left(\omega_a\hat{\sigma}_+\hat{\sigma}_- + \omega_c\hat{a}^\dagger\hat{a} + g(\hat{\sigma}_+ + \hat{\sigma}_-)(\hat{a}^\dagger + \hat{a})\right). \tag{2.79}$$

The terms in $\hat{\sigma}_+\hat{a}^\dagger$ and $\hat{\sigma}_-\hat{a}$ oscillate rapidly (i.e. much more quickly than the absorption or emission timescales of interest) close to resonance, and using the rotating wave approximation we neglect them, yielding the standard Jaynes-Cummings Hamiltonian for

a 2-level atom [41]

$$\hat{H}_{JC2} = \hbar\left(\omega_a\hat{\sigma}_+\hat{\sigma}_- + \omega_c\hat{a}^\dagger\hat{a} + g(\hat{a}^\dagger\hat{\sigma}_- + \hat{a}\hat{\sigma}_+)\right). \tag{2.80}$$

For a cavity tuned to resonance with a two-level system starting with a single cavity photon and an unexcited atom, we see that the excitation may be transferred between the cavity and the atom, and with no decay channels this oscillation will continue with frequency g.

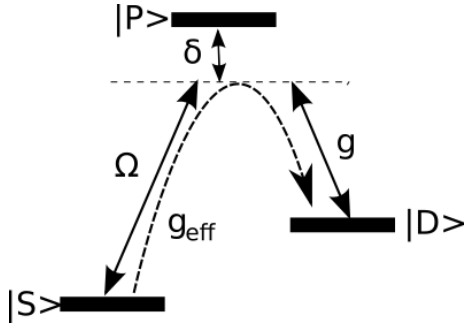

Figure 2.8: A 3-level cavity-coupled system. By applying a detuning δ to both the cavity and the laser, an effective coupling of $g_{\text{eff}} = \frac{g\Omega}{2\delta}$ can be obtained between the S and D state while suppressing population of the P state.

Let us now consider a 3-level λ system coupled to an optical cavity, as we shall use in practice. The atomic states shall be referred to as $|S\rangle, |P\rangle$, and $|D\rangle$, as illustrated in figure 2.8. The relevant transition frequencies are $\omega_{SP} = \omega_P - \omega_S$, and $\omega_{PD} = \omega_P - \omega_D$. The $|S\rangle \rightarrow |P\rangle$, transition is driven by a laser of frequency ω_L and Rabi frequency ω. The $|P\rangle \rightarrow |D\rangle$ transition is cavity coupled. At the Raman resonance, the laser and cavity detunings equal are both equal to δ. Defining $\sigma_S = |P\rangle\langle S|$ and $\sigma_D = |P\rangle\langle D|$, the interaction Hamiltonian becomes [27]

$$\hat{H}_{JC3} = \hbar\delta(|D\rangle\langle D| + |S\rangle\langle S|) - \hbar\frac{\Omega}{2}(\sigma_S + \sigma_S^\dagger) - \hbar g_0(a\sigma_D^\dagger + a^\dagger\sigma_D) \tag{2.81}$$

with eigenstates

$$\phi_0 = \cos\Theta\,|S,0\rangle - \sin\Theta\,|D,1\rangle, \tag{2.82}$$

$$\phi_+ = \cos\Phi\sin\Theta\,|S,0\rangle - \sin\Phi\,|P,0\rangle + \cos\Theta\cos\Phi\,|D,1\rangle, \tag{2.83}$$

$$\phi_- = \sin\Phi\sin\Theta\,|S,0\rangle + \sin\Phi\,|P,0\rangle + \sin\Theta\cos\Phi\,|D,1\rangle, \tag{2.84}$$

for a single photon in the system. The mixing angles are given by

$$\Theta = \arctan\left[\frac{\Omega}{2g_0}\right], \text{ and} \tag{2.85}$$

$$\Phi = \arctan\left[\frac{\sqrt{4g_0^2+\omega^2}}{\sqrt{4g_0^2+\omega^2+\delta^2}-\delta}\right] \tag{2.86}$$

The state ϕ_0 does not involve any $|P\rangle$ state population and is hence a dark state of the system. If the cavity photon does not decay or if the system is driven at ω_c, the system may remain stably in this state without undergoing spontaneous emission. By driving the $|S\rangle \rightarrow |P\rangle$ transition with a detuning δ to match the detuning of the cavity from the $|P\rangle \rightarrow |D\rangle$ transition, a Raman transition from $|S\rangle \rightarrow |D\rangle$ may be coherently driven, with the emission of a photon into the cavity. This is the basic process used to generate photons in our experiment and which will ultimately be used to generate entanglement between pairs and chains of ions. Such a scheme was first proposed by Kimble and Law [42].

2.4 Applications of the cQED system and their implementations.

Cavity-coupled ions are highly versatile systems which combine the long coherence times and easy state manipulation of atomic qubits with the easy readout and quantum-information transfer properties of photonic qubits. Several schemes exist to harness the unique capabilities of such a system, some of which will be outlined here.

2.4.1 Generation of Single Polarised Photons

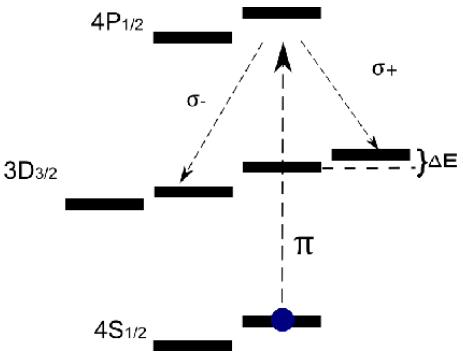

Figure 2.9: Experimental scheme for the generation of single photons of given polarisation.

This setup has several novel applications, including acting as a source of single polarised photons. An illustration of this scheme is shown in figure 2.9.

While for most applications the applied magnetic field need only be strong enough to lift the degeneracy between the angular-momentum states, in this case the field should be strong enough that the splitting between states ΔE is greater than the cavity linewidth. The cavity may then be tuned to a specific transition, selecting only $\hat{\sigma}_+$ or $\hat{\sigma}_-$ photons. By driving a single ion coupled to the cavity with an appropriately shaped pulse, single photons of this polarisation may be produced [43]. The emitted photons may then be rotated to give any other orthogonal set of polarisations.

2.4.2 Deterministic State Mapping

The transfer of quantum information from stationary to flying qubits is an important objective in any QIP system design. The scheme presented in figure 2.10[44] illustrates how an ionic qubit in the Calcium 40 ground state may be mapped to the polarisation state of a cavity photon. Such a photon could then be collected by an optical fibre and transferred to another system where the quantum information would be mapped back into a stationary qubit.

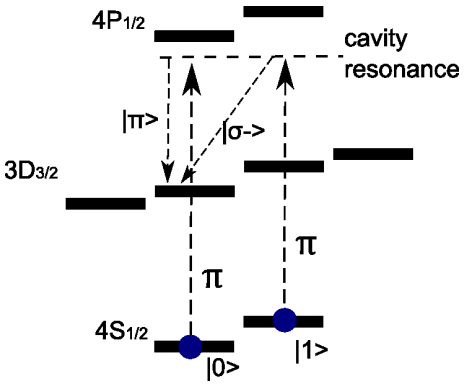

Figure 2.10: Experimental scheme for mapping an ionic qubit to a photonic qubit.

This scheme involves driving the ion with two different frequency π-pulses simultaneously. The frequency difference should be equal to the energy difference between the two ground states divided by $\hbar$. These will transfer ions in the $|0\rangle, |1\rangle$, or superposition states to the $3d_{-\frac{1}{2}}$ state, while producing a $\hat{\sigma}_+, \hat{\sigma}_-$, or superposition state photon. The quantum information is thereby transferred from the ion to the photon.

2.4.3 Probabilistic Entanglement and cluster state generation

The ultimate future goal of this experiment is to generate entanglement between strings of ions to create a *Cluster State*. While entanglement is an interesting resource by itself, large scale entangled states allow for quantum information processing (QIP) in the one-way or measurement-based paradigm. In this model, rather than the information being stored in the quantum bits, it is stored in the correlations between them; projective measurements are performed on the qubits (hence the operation is "one way" rather than unitary), and information may also be teleported between nodes using Bell-state measurements. It has been shown that any quantum circuit may be implemented in a measurement-based scheme [36].

In order to create a cluster state, we must be able to generate entanglement between pairs of qubits (or *nodes*), and to fuse these pairs of qubits into a large scale entangled state. The proposed entanglement scheme [45] is probabilistic; however as the size of the entangled state grows exponentially it should be possible to efficiently generate a large scale entangled state.

We take advantage of the λ system of singly ionised calcium 40 to implement our

entanglement scheme. The basic principal is illustrated in figure 2.11a below.

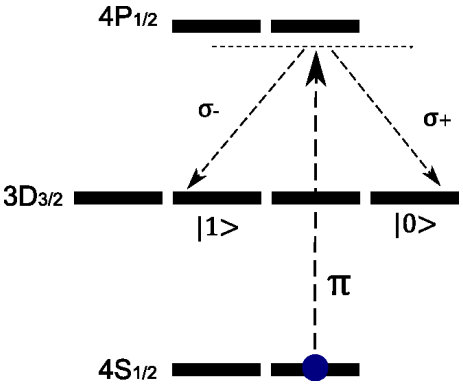

(a) Entanglement scheme for 2 ions

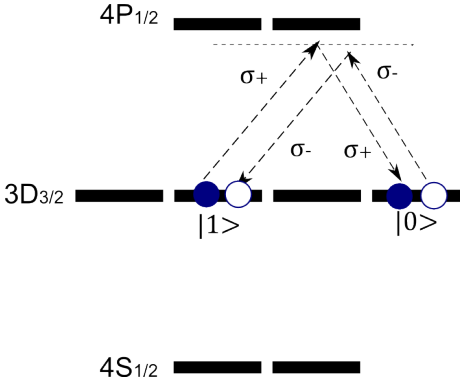

(b) The fusion operation for growing the entangled state.

Figure 2.11: Scheme for generation of a large-scale entangled state.

A pair of cavity-coupled ions are initially prepared in the $m = +\frac{1}{2}$ state of the ground level manifold. The magnetic field is sufficiently small to ensure that the level-splitting is less than the cavity linewidth. A π-pulse drives a cavity-assisted Raman transition to the $D_{\frac{3}{2}}$ level. The ions may probabilistically end up in either the $m = -\frac{1}{2}$ or $+\frac{3}{2}$ states, emitting either a left or right circularly polarised photon into the cavity mode in the process. The polarisation of the produced photons is then detected. In the case that both polarisations are the same, we know that the two ions are in the same final state, and what that state is. If the two detected polarisations are different, we know that the two ions are in different final states. The cavity erases the positional information about the photon's origins, meaning that as long as the photons are identical in all other respects (frequency, amplitude, time-bin), they will be indistinguishable. This indistinguishability means that in the process of measuring the photons, the individual ion-photon entanglements are destroyed but entanglement is generated between the ions, as it is impossible to tell which ion emitted each photon. The detected photons are known as heralds, and this kind of scheme is referred to as "heralded entanglement" as it is probabilistic and successful cases are heralded by the arrival of two differently polarised photons.

This scheme can be used to entangle many pairs of ions, but not to create larger entangled states as that would involve destroying the current state of the ion. A similar scheme to fuse pairs or strings of entangled ions is illustrated in figure 2.11b. Here, adjacent ions of different entangled pairs are simultaneously driven with a detuned 866 nm $(\hat{\sigma}_+ + \hat{\sigma}_-)$-pulse, which drives the ion to a virtual level close to the P level and back down to the D state again. If both ions are successfully excited, we may observe the emission of

two similarly polarised photons if both ions decay to the same state, or of two differently polarised photons if the ions decay to opposite states (bearing in mind that each individual ion is in a superposition of two states initially as part of an entangled state!) As before, in the case of identical polarisations no entanglement is generated and the entanglement process must begin again, but if differently polarised photons are produced entanglement is generated between the ions without destroying the pre-existing entanglement they share with the other ions, thereby producing a 4-ion entangled state. This same scheme can be used to fuse two 4-ion entangled states to an 8-ion entangled state and so on, to the limit of the number of ions that may be trapped in a string in the trap.

A number of considerations affect the indistinguishability of the photons. Principally, excitation of the P state leading to spontaneous emission will cause decoherence and destroy the entangled state. In order to minimise the chance of populating the P-state, the cavity must be detuned from resonance. The spontaneous emission rate, Γ_s is proportional to the inverse of the detuning squared. The cavity coupling g is proportional to the inverse of the detuning, and so the ratio of cavity photons to spontaneous emission may be increased arbitrarily in principal; in practise to values of g which yield results on the experimental timescale. The ions must also be cooled to the highest degree possible, as any motional excitation can lead to a frequency shift which would render the photons partially distinguishable. The ions must be driven to produce a single photon at the same time; if one ion cycles around the $S \rightarrow P$ transitions multiple times before emitting a photon while the other emits a photon immediately following the initial excitation each photon will be received in a different time bin. Detuning the cavity helps with this but pulse-shaping is also important. Each ion must experience an equal intensity of the driving field, so for long chains of ions an Electro-Optic Deflector may be necessary to move the laser spot to the region currently being entangled. Similarly, each ion must be identically coupled to the cavity (i.e. g should be the same for both ions). Ideally they will also be maximally coupled to yield a high experimental efficiency. Ensuring the equal coupling of multiple ions to the cavity mode is therefore an important objective and this thesis culminates in an illustration of the achievement of this.

Chapter 3

The ion trap

In order to study cavity QED in an ion trap, a complex system is involved. This chapter describes the individual components of the ion trap and cavity, the methods used in its preparation, the electronics used outside the trap to control and manipulate the ions and cavity, and finally the layout functionality of the optics surrounding the trap. Further detail of how these systems are optimised are given in chapter 5.

3.1 Trap hardware and assembly

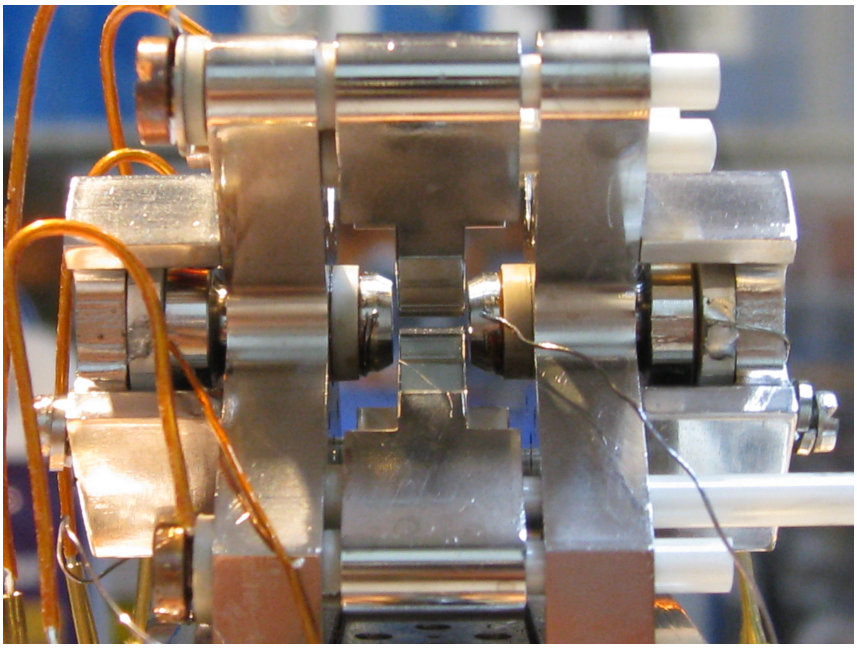

Figure 3.1: The fully assembled trap outside the vacuum chamber.

3.1.1 The trap mount

The trap mount (highlighted in figure 3.2) is the superstructure which holds in place and maintains the alignment of the many component subsystems of the trap, broadly the RF electrodes, DC electrodes, atomic oven, and cavity. It is cut from a single piece of stainless steel by Electrical Discharge Machining (EDM). The structural stability and accurate placement of the screw holes is of paramount importance in order to form a stable, reliable trap. It is connected firmly to the feedthrough flange by two screws, and electrically grounded through it. It is insulated from all other conductive parts of the trap by ceramic spacers or MACOR films.

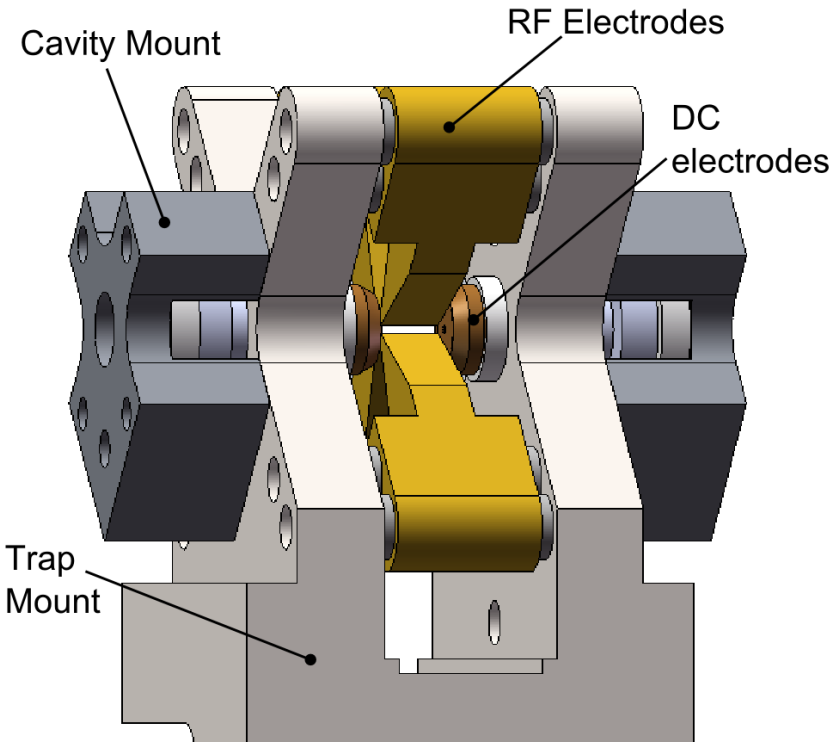

Figure 3.2: Schematic of the trap. The mounting structure is shown in white. It provides support and stability for the other experimental components, including the RF Electrodes, the DC electrodes, the cavity mount, and also features space below for the atomic oven and collimator.

3.1.2 The RF electrodes

The four RF electrodes were machined from the same single piece of stainless steel as the trap mount. The structure was cut out as a whole and drilled before the 5 mm electrodes were cut from the mount, ensuring precise alignment between the mount and electrode holes. They are tapered to a point which allows them to be placed more closely together

and allows greater optical access, while still allowing us to operate in the approximation of parabolic electrodes used in section 2.1. Each electrode features a pair of holes through which ceramic dowel pins are inserted to define the electrode's position and alignment within the trap. One dowel pin extends through one side of the trap mount, through the electrode and out the other side; the other goes only through one side of the trap mount and half-way into the electrode. Into the remaining space is screwed a copper screw to which the wire carrying that electrode's RF voltage is attached. The screw has a hole drilled through the centre to allow any trapped air to be evacuated. MACOR spacers prevent the electrodes from sliding axially along the dowel pins, and insulate the electrodes and screws from the trap mount. These components are shown in figure 3.3.

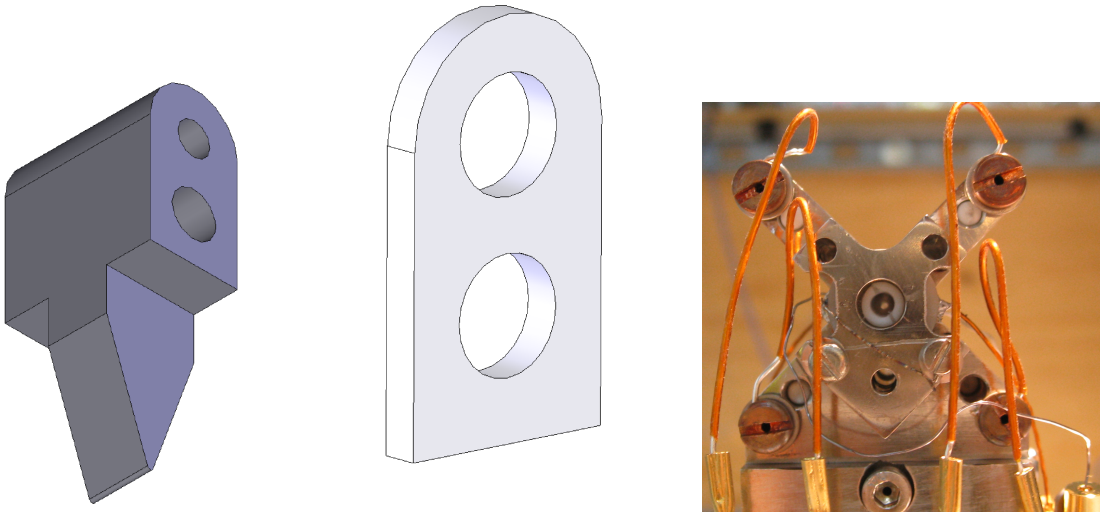

(a) A single RF electrode.

(b) An RF electrode spacer.

(c) The mounting screws connected to the RF voltage input wires and isolating spacers visible.

Figure 3.3: RF electrode assembly.

Great care must be taken when inserting the electrodes that they do not clash with each other, which may damage the sharp edge of the blade leading to local variations in the trapping potential. This means the electrodes must be moved radially into position in the correct orientation, rather than trying to roughly position them and rotate them later. The electrode-electrode distance at the trap centre is 660 μm when all electrodes are in position. The distance from the trap-centre to the electrodes is 465 μm[1].

[1]In the case that the amplitudes on each of the RF electrodes are equal. Later the trap centre shall be deliberately moved, as described in section 6.2.2

3.1.3 The DC Electrodes

The trap DC electrodes are held at a constant voltage and close the trap potential in the axial direction, as the RF field defines an almost purely radial pseudopotential. They consist of a conical trapezoid of steel bonded to a PEEK spacer using UHV compatible glue. The spacer is necessary to isolate the electrodes from the trap mount structure. The voltage is supplied to the electrodes via tantalum wires that have been spot-welded onto the side and connect to two of the trap feedthroughs.

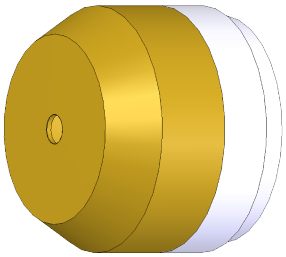

Figure 3.4: A single DC electrode. The electrode material is highlighted; it is mounted on an insulating PEEK spacer.

Unlike in the design of most linear Paul traps, these DC electrodes feature a 1 mm hole which allows the cavity mode to pass through the trap centre, with mirrors situated just behind the electrodes. These holes are sufficiently small that the axial potential is not significantly affected. When mounted, the DC electrodes are separated by 5 mm.

3.1.4 The oven mount

The atomic oven consists of a tantalum tube wrapped in tantalum wire through which currents on the order of 2 A may be passed to cause vaporization of granular calcium within the tube. A schematic is shown in figure 3.5a. The supply voltage for this component must be kept electrically isolated from the trap mount. While it would in principal be possible to use the trap mount body as the ground for the oven, we decided to maintain an independent ground channel to avoid the possibility of creating ground loops through the trap and to provide the option of greater flexibility with respect to how the trap electronics are wired. This isolation is achieved using ceramic cases, into which are mounted steel mounting washers spot-welded to the wire which wraps around the oven. Copper wire of diameter 2.5 mm attached to the oven-current feedthrough is pressed against this washer by means of a ceramic spool and a metal screw which screws into the trap mount and maintains good electrical contact between the oven feedthrough wire and the oven supply itself. This arrangement is illustrated in figure 3.5b.

In order to avoid coating the trap with deposits of calcium and other impurities, a collimator is used to ensure only a thin stream of calcium ions is permitted to pass to the trap centre. The oven itself is not tightly held or clamped onto any component of the trap

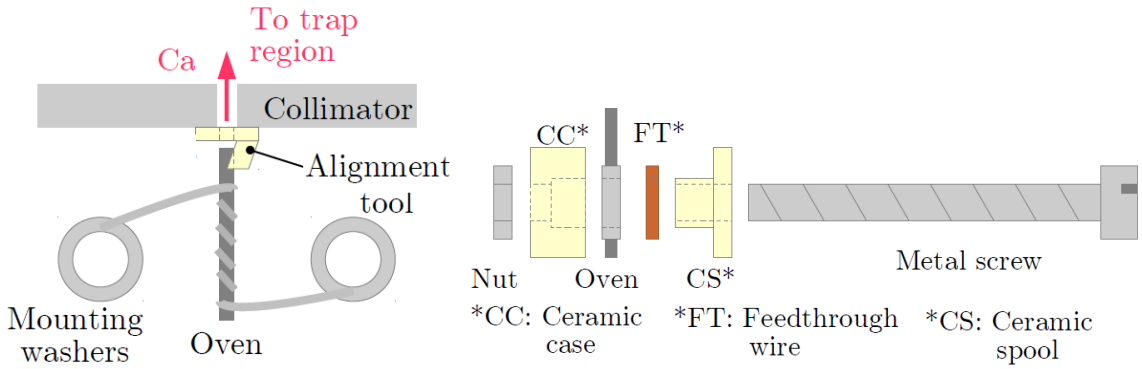

(a) The trap oven connection and alignment.

(b) The screw assembly to connect the oven to the feedthroughs while isolating it from the trap body.

Figure 3.5: The oven.

(as this would provide electrical and thermal contact, neither of which is desirable), so further measures are required to ensure that the oven is aligned with the collimator, and remains so during the process of resealing and moving the vacuum chamber, and baking, which may take over one week.

The collimator consists of a small hole drilled in a removable metal plate of thickness $\sim 2\,\text{mm}$. The collimation hole originally had 0.3 mm diameter, but due to the difficulty of ensuring alignment through this the first time the trap was prepared and during subsequent trap openings and closings, the hole was widened to 1 mm. A small ceramic groove glued to the underside of the collimator plate (visible in figure 3.5a) is used as an alignment tool to hold the top of the oven so that it rests just below the collimation hole.

The plate itself must be slid into a groove in the trap mount beneath the trap centre, and held in place with a mounting screw once the collimator can be seen to be between the RF electrodes from above. This positioning can be achieved by illuminating the trap from below and looking for transmission of scattered light through the collimator aperture, and then finely adjusted by imaging the plate using a camera and an appropriate lens system focussed on the collimator plane.

Also on this plate is a $1\,\text{cm} \times 1\,\text{cm}$ copper square isolated from the plate and trap body by a layer of Kapton and which is connected to one of the trap feedthroughs. This "excitation plate" allows a perturbing voltage to be applied to the trap from below, and is used to drive the trap radial secular oscillations so that the resonant frequencies can be measured (see section 5.3).

3.1.5 The experimental cavity

The components detailed thus far comprise the entirety of the in-vacuum part of the linear Paul trap, capable of trapping ions for several hours. This experiment also features an optical cavity oriented along the trap axis, which is mounted upon the same mounting structure as the trap.

In order to avoid the problems of distortions of the trapping field by the cavity dielectric mirrors, the mirrors are mounted behind the DC endcap electrodes and the mode passes through two 1 mm diameter holes in the centre of these electrodes. The mirrors themselves have a 1 mm diameter surface area, and reflectivities of 5 and 100 ppm. They are mounted on a cylindrical glass substrate 5mm long which is tapered with a 20° angle to the mirror surface, allowing the structure to be held in place by a mounting collet from which the mirror protrudes, as shown in figure 3.6. A PEEK grub screw with a hole in the centre for optical access screws into the collet from behind the substrate, holding it in place.

Behind the collet is located a piezo-electric transducer (PZT or piezo), which responds to an applied voltage by lengthening or contracting, allowing the mirrors to be moved and hence the cavity length and position to be changed or stabilised. The piezos used were ring piezos, to allow optical access. They were glued to the collet on one side and the outer mirror-mount structure using UHV compatible glue.

The whole structure is affixed to the trap mount behind the DC electrodes by means of screws passing through the mirror mount and into the trap mount. It must be carefully positioned to ensure that a good cavity mode is formed with the other mirror 5.25 mm away, and that the mode is not clipping on the DC endcap electrodes.

The mirrors were cleaned carefully by first blowing any loose debris from the surface with a compressed air blower, and then lifting any remaining particles by applying a layer of 1$^{\text{st}}$ contact rubber solution, and peeling it off once it was set. Residual rubber was removed by wiping once with acetone on lens tissue, and then by placing the mirror and substrate into a sonic bath with acetone for 10 minutes. It was ensured they were exposed to the environment for a minimum amount of time before closing the trap. Gloves, face masks, and optically clean tools were always used while working with them, and whenever they were not being worked on the setup was covered with a clean piece of aluminium foil.

Figure 3.7 shows the cavity mirrors and their substrates out of the trap structure as the finesse was measured. The finesse can be calculated as the ratio of the cavity linewidth to the free spectral range ($\mathcal{F} = \frac{\Delta}{\text{FSR}}$). These can be observed by sweeping the cavity length over 1 FSR while monitoring the transmission on a fast photodiode. Remembering

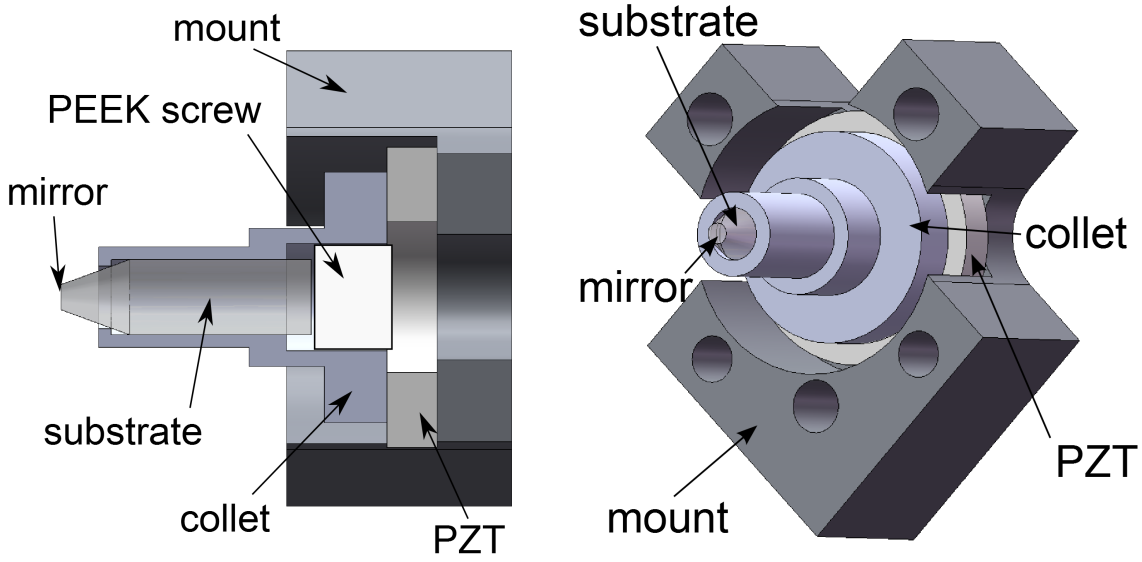

(a) (b)

Figure 3.6: The cavity mount a) in section and b) in perspective.

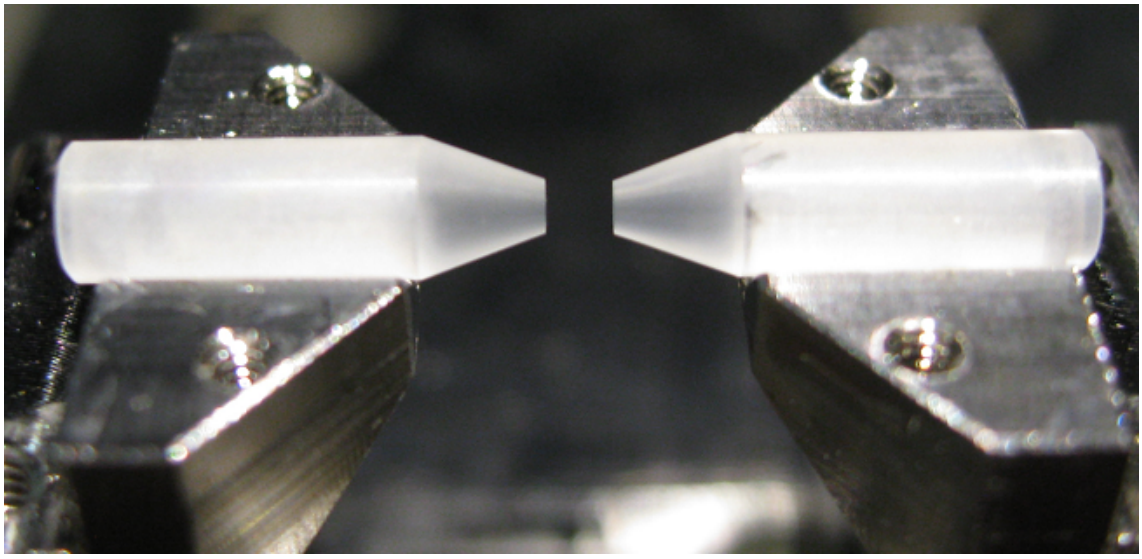

Figure 3.7: The cavity mirrors and substrates.

that $\mathcal{F} = \frac{\pi c}{2l\kappa}$, it is clear that the cavity linewidth is inversely proportional to the mirror separation, and so at the separations used in the trap, the cavity linewidth is much lower than the linewidth of the laser used to measure the finesse, giving an artificially low value. Out of the trap the cavity length can be reduced to much smaller than its in-situ length. The finesse is constant as it is determined only by the mirror reflectivities $R_1 \text{and} R_2 : \mathcal{F} \approx \frac{\pi (R_1 R_2)^{\frac{1}{4}}}{1-(R_1 R_2)^{\frac{1}{2}}}$. By decreasing the cavity length, we may increasing the cavity linewidth to much greater than that of the laser, while decreasing the FSR, to the point

where the finesse can be accurately measured as 60,000.

When the mirrors were inserted into the trap, they were initially aligned using the method that had previously been used in this trap [46]. The cavity was length scanned across the TEM_{00} resonance and the output observed on a CCD. A hypodermic needle was used to probe the mode by scanning the needle's point in space in proximity to the geometric trap centre between the RF electrodes. At the point the needle entered the mode the transmission observed on the CCD vanished. By approaching the mode with the needle from either side, the position of the mode centre in that plane could be determined as the point equidistant between the points where the needle caused the observed output mode to cease to be visible. The radial position of the mode was found by performing this measurement first in the horizontal direction and then in the vertical direction by remounting the needle on a stage perpendicular to the first. The mirror positions were adjusted to ensure that the mode was equidistant from the RF electrodes in the horizontal and vertical directions at either end of the trap. After baking the finesse was still found to be lower than expected, and investigation of the system revealed that the mode was clipping on the DC electrodes. The mirrors were repositioned according to optical imaging in the planes of the mirrors to ensure the mode was central with respect to the endcaps. This was found to yield results consistent with a finesse of 60,000.

3.1.6 Bringing the system to vacuum

Once the trap and cavity had been assembled, the system needed to be sealed and brought to a high vacuum. The vacuum chamber was sealed using a copper gasket and CF 40 flange. The elbow below the trap lead to a T-piece which was similarly sealed, with one port leading to an ion-getter pump which was turned off until baking was complete, and the other port connected to a flexible bellows leading to a turbo pump backed by a roughing pump.

As all parts of the trap and vacuum system had been exposed to the atmosphere for an extended period of time, it was also necessary to "bake" the system to remove any dissolved atoms which may "de-gas" into our system and limit the minimum pressure that could be achieved. Baking typically takes several days. Higher temperatures will lead to a quicker out-gassing, but the temperatures that can be achieved are limited by the trap materials. In our case, the main limitation was the indium seals around the vacuum chamber windows, which have a melting point of 110 °C. If this part of the trap reached this temperature we could compromise our vacuum and cause serious damage to

the experiment.

Heater belts and collars - braids of metal through which high currents could be run to generate high temperatures through resistive heating - were affixed to the trap at the flanges, and wrapped around the bellows of the pumping system. The entire trap and the vacuum connections were covered in aluminium foil, which would prevent heat from radiating out. As the heating elements are distributed non-uniformly, the system will not thermalise to a uniform temperature, so parts of the system far from the windows may be heated to higher temperatures. A total of six thermocouples were attached to the trap by Kapton tape, 2 close to the window on top of the can, 2 close to the windows on the side of the can, and 2 on other less temperature critical parts of the experiment.

Initially the trap was valved off from the vacuum system, and the roughing pump was turned on to provide a 10^{-2} mbar backing pressure for the turbo pump, and to pump down the bellows. Care must be taken to ensure that the bellows are not taut before pumping begins, as they will contract when pumping is applied, possibly causing the trap to shift. The valve to the trap system was slowly opened as the pressure stabilised, and once the entire system had reached 10^{-2} mbar the turbo pump was turned on. This brought the system to 10^{-5} mbar within minutes. The system reached 10^{-10} mbar after baking.

To ensure that the system did not become too hot, the voltage applied to the heating belts and collars was turned up in steps while monitoring the temperature read from the thermocouples. The system thermalised over the course of several hours, and it took about one day to bring the system stably to its maximum temperature. During this time the pressure rose to $O(10^{-2} - 10^{-3}$ mbar). Over the course of a further week at these temperatures, the pressure had dropped to 10^{-8} mbar.

Once the pressure had stopped dropping, the system was returned to operating temperatures. It was also important not to cool the system too quickly or unevenly, to avoid causing dangerous stresses on the windows and joins. Once the system had thermalised with no current flowing through the heating elements, the pressure reached $O(10^{-10}$ mbar). The system was then checked for damage that may have occurred during baking, including a visual check to ensure there had been no major slippage of components within the trap, a test to ensure the electrical feedthroughs were not short-circuited, and a remeasurement of the cavity finesse.

3.2 Trapping electronics

The trap feedthroughs connect the interior of the vacuum chamber with the outside world. Some of the incoming signals come from DAQ cards, some from current or voltage sources, others from RF oscillators and amplifiers. Each feedthrough is connected to the incoming wire by a barrel connector, which acts as a strain relief and avoids the potential dangers of soldering directly to a feedthrough, as they may become damaged or begin to leak if subject to high temperatures or stresses. Some additional structure is required to ensure all the input wires connect to the trap with minimal interference. The trap itself is mounted above an elbow leading to the vacuum system as described in section 3.1.6. A collar attached the base of the trap chamber to an aluminium mounting box, which has been drilled to allow the fixtures for the incoming signals to be mounted below the trap, while providing shielding from the rest of the lab environment. These fixtures and components will be detailed in the following sections.

3.2.1 The RF trap drive electronics

Most of the structure within the mounting box is dedicated to transmitting the RF trapping voltage, without which there would be no confinement and no trap. The trapping circuit is shown in figure 3.8. The trapping voltage is generated by an SRS DS345 function

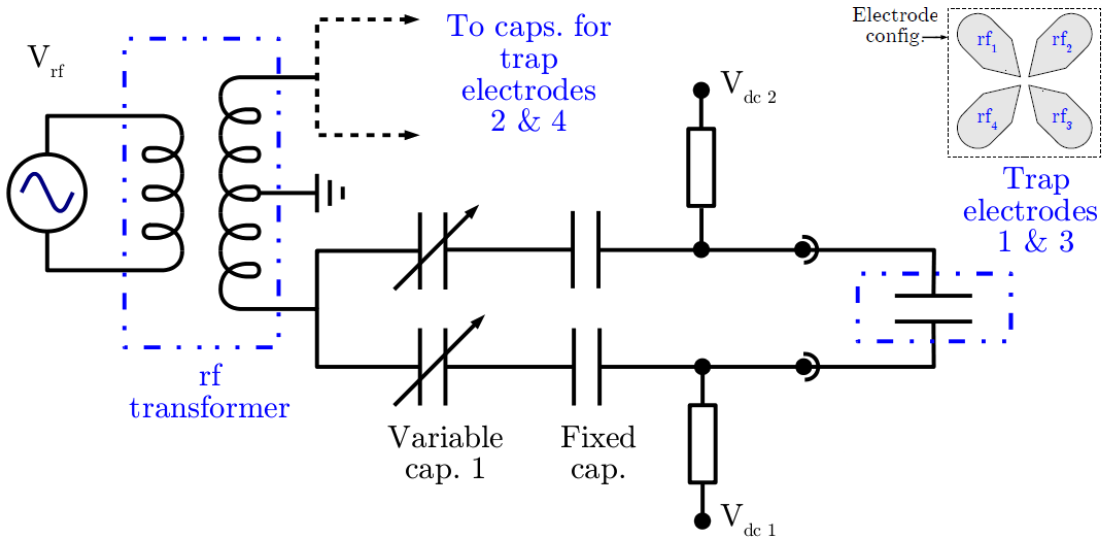

Figure 3.8: The resonant driving circuit for the trap. The variable capacitors allow adjustment of the Voltage amplitude on each electrode, allowing the trap centre to be adjusted to optimise overlap of the trap and cavity axes.

generator, and is amplified by a 5 W amplifier before being sent to the trap. An RF reflec-

tometer is connected after the amplifier during the initial setup of the resonance circuit in order to monitor the power passing through the amplifier. The amplifier feeds a drive coil which is coupled to the resonator coil to form an RF transformer as illustrated in figure 3.8. The favourable ratio of the number of turns on the drive (1 turn) to resonator (10 turns) coil produces a further enhancement of the drive voltage. The coupling between coils depends on the shape and spatial orientation of the drive coil, which is adjusted by hand to obtain optimal impedance matching by minimising the power reflected from the drive coil through the reflectometer.

While the trap electrodes are effectively an open circuit, there are series capacitances and high voltages involved. Bare copper wire of diameter 2.5 mm is used from the resonator onward due to its large surface area and high thermal conductivity so that it will not be damaged by high powers flowing through them. It is ensured that the length of each of the four wires from the resonator coil to the variable capacitors (*varcaps*) and also from the varcaps to the feedthroughs are the same length in order to avoid phase differences arising from a differing travel time of the voltages from the resonator to the electrode.

The resonator coil is grounded in the centre so that the voltages produced between either end and the centre are π-out-of-phase sinusoids, as we are driving the trap in symmetric mode. Diametrically opposite electrodes (1 & 3, 2 & 4) are fed from the same end of the resonator coil and hence oscillate in phase, adjacent electrodes should oscillate π out of phase with each other. There is a second pickup coil of 1 loop located a few centimetres from the resonator coil. It is simply connected to the outside of the mounting box via a BNC connector. Its function is to allow the RF amplitude to be monitored so that the resonant frequency may be adjusted in the case of any changes, either from thermal drift or by direct adjustment.

This trap differs from conventional Paul traps, as a variable capacitor is placed in series before a fixed capacitor which passes the signal to the trap feedthrough and then the electrode. Capacitors in series with the electrodes are not exceptional in Paul traps, as they allow any DC component to be filtered and assist with impedance matching - the trap capacitance is $\sim 25\,\mathrm{pF}$, which is much less than the capacitance of the fixed capacitors - but the variable capacitors have been introduced into the driving circuit in order to enable the amplitude of the RF voltage on each electrode to be individually adjusted by increasing or decreasing the series impedance. This enables the trap centre to be shifted radially, so that the trap axis may be positioned along the cavity axis - with a cavity waist of $36\,\mu$m fine grain control is required to obtain the optimal g factor for

the highest experimental efficiencies and fidelities. A potential difficulty here is that if a large difference in capacitances is required, a large phase difference may arise between the voltages on the individual electrodes, contributing another unremovable micromotion component that limits the minimum achievable temperature or trap stability. In this case, a better phase match may be achieved by adjusting opposite electrodes iteratively while maintaining the ion position, or by introducing phase delays by other means.

The variable capacitors themselves are constructed of discs of copper of 25 mm diameter and 2 mm thickness, mounted on micrometer stages and fixed-position clamps housed within the support structure close to the trap. The copper discs can be separated, and the capacitance increased, by opening the micrometer screw. They may be short-circuited entirely by closing the screw until the plates are in direct electrical contact, or a sheet of Kapton may be placed between the plates to allow the micrometer screws to be fully closed without shorting the circuit.

Following the capacitors, the RF signal is joined by a DC input (V_{dc} in figure 3.8) across a 1 MΩ resistor. These are the micromotion compensation inputs, which add a DC component to the RF signal to nullify any stray field in the trap. The resistor helps avoid the presence of the external circuitry affecting the trap resonance or a large RF signal being transmitted to other parts of the control electronics. In addition, before the resistor all coated wires are taped to the sides of the conductive mounting box with aluminium tape, and kept to the minimum length possible before being sent to a series of low-pass filters, as will be described in section 3.2.2.

3.2.2 Non-RF electronics

Aside from the trap drive, a range of signals of differing voltage, current and frequency must be brought into close proximity and fed to the relevant trap component, without transmitting or receiving interference. Therefore, all wires are kept as short as possible, shielded to the maximum extent, and filtered to remove frequencies outside the range those wires should transmit. The figures 3.9a and 3.9b contrast the wiring within the mounting box before and after the trap was reassembled. All input wires apart from the RF inputs are filtered to permit only frequencies up to the maximum that would be required for that channel. The filter circuitry is mounted within a second stainless steel box to provide additional shielding from the resonator. The filters are bi-directional (see figure 3.10), so that the wiring could neither carry spurious signals into the trap, nor back to the control electronics. Even elements which are insensitive to noise signals, like the oven current

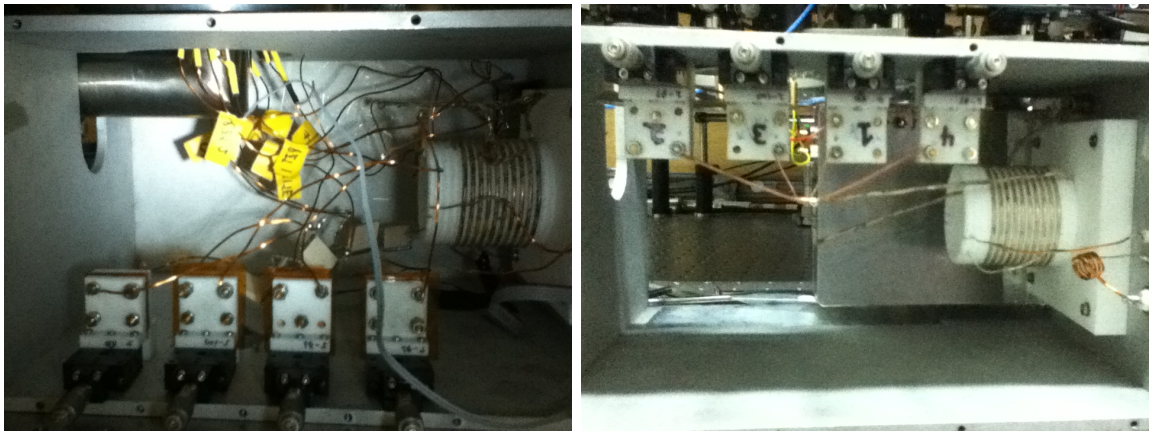

(a) (b)

Figure 3.9: The wiring of the mounting box (a) before and (b) after the trap was disassembled and reassembled. Instabilities in the trap may have been caused by electrical pickup or phase delays caused by wires of differing length.

Circuit	**Cutoff Frequency**
Oven current	1 Hz
DC endcap potentials	1 Hz
Micromotion compensation voltages	1 Hz
Cavity piezos	3k Hz
Excitation plate	10 MHz

Table 3.1: The cutoff frequencies for the filters on the non-RF inputs to the trap.

channel, are filtered to prevent noise entering the trap where it may still interfere with the trap potential. The wires carrying the filtered signals leave the box through a final filter feedthrough and then travel to the trap along the edge of the outer mounting box along the shortest possible path to the feedthrough. Due care was taken to ensure that components appropriate to the voltage or current requirements of the particular circuit were selected. The cutoff frequencies for each input wire is shown in table 3.1.

3.2.3 The magnetic field coils

The magnetic field coils (shown in figure 3.11) surround the trap and are capable of generating a local magnetic field in any direction. These coils may be used to compensate the earth's magnetic field (section 5.5) or to generate a bias field in a specified direction

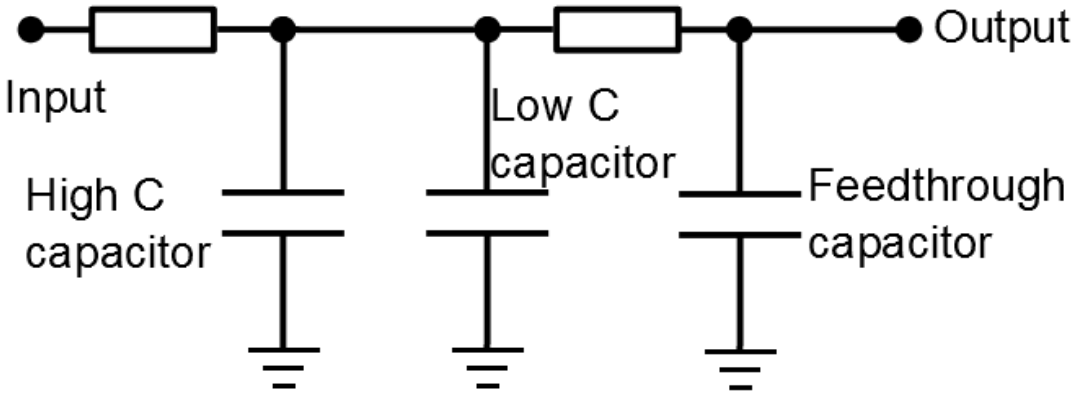

Figure 3.10: The general circuit used to filter spurious signals in either direction on the non-RF trap input wires. An initial high value resistor reduces the amplitude of any noise going back into the input, while a standard low-pass filter of time constant $\tau = \frac{1}{2\pi RC}$ removes high frequency noise from the input. High and low value capacitances are connected to ground in parallel, as the response of large capacitors can fall off at high frequencies. The time constant was determined by the high value capacitor. A feedthrough capacitor removes any additional noise that may have been picked up and helps prevent pickup travelling back through the filter into the control electronics. In choosing components, consideration must be given to the signals propagating through the circuit in terms of expected frequencies, currents and voltages.

to define a polarisation axis or to cause splitting of magnetic sublevels (section 6.1). They consist of 6 coils, 2 perpendicular to each of the 3 axes of the system. In the horizontal plane, rectangular coils of width 40 mm, height 65 mm, and separation 125 mm are used. They can each generate a field of 0.6 mT/A at the trap centre. In the vertical direction circular coils of diameter 125 mm and separation 75 mm generate a field of 2.5 mT/A. The achievable fields are limited by the current that can be supplied, and the resistive heating that can be tolerated by the experiment, though nulling the field generally requires O(100 mA) to be applied to each axis. These currents do not produce a significant temperature rise.

3.3 Trap optics

The entire experiment is mounted on an RS300 sealed hole optical table mounted with tuned damping on four l-2000 series laminar flow stabilisers from Newport. Once the trap

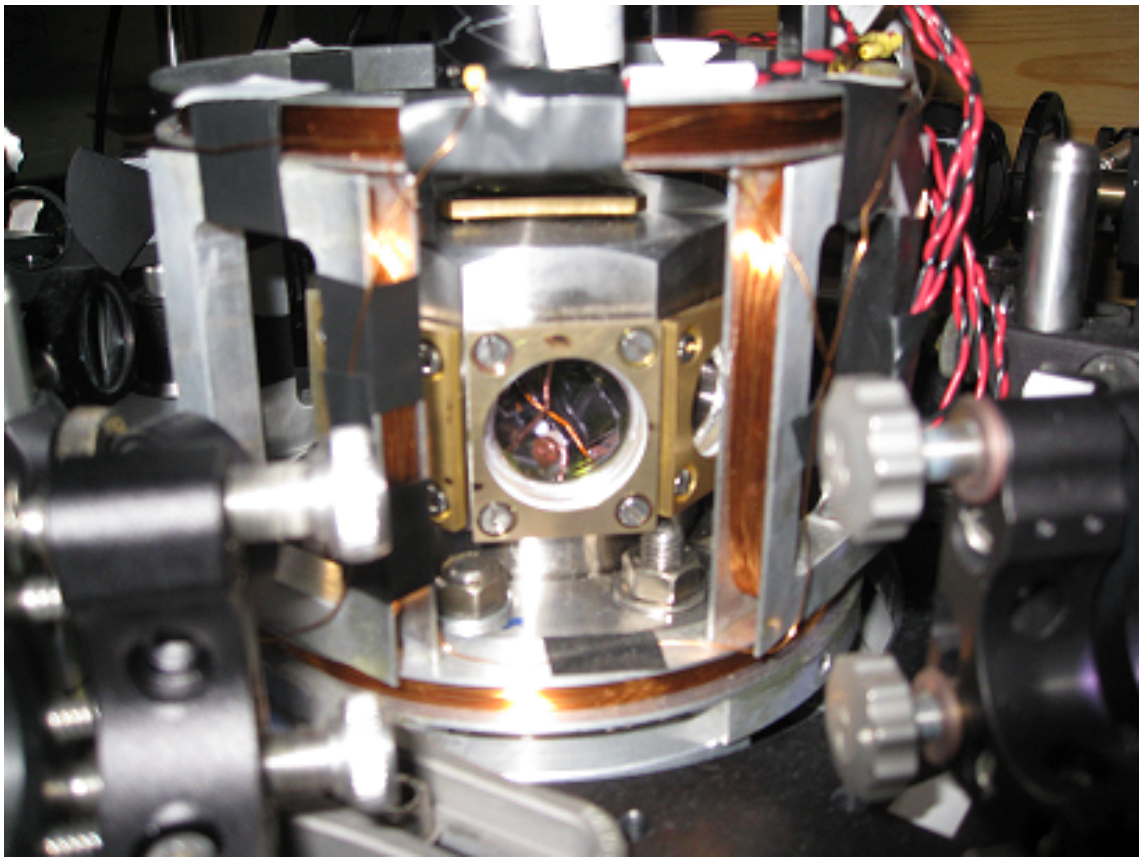

Figure 3.11: The magnetic field coils *in situ* around the trap chamber.

has been brought to a high vacuum and the electronics assembled, the optical inputs may be assembled around it. Most of the optics are mounted on a breadboard supported at the level of the trap chamber, 17 cm above the table. Careful alignment of the lasers, which have beam waists of 10s of μm, is required to ensure that they pass through the trapping area (of extent O(10-100 μm)). A hole in the breadboard allows it to fit around the trap. A breadboard on a second-tier 13 cm above the first mounts the free-space fluorescence detection optics, the CCD and the PMT, which collect light from the trap from above.

The layout of the first level is shown in Figure 3.12 below. The operation of the trap will be described in detail in chapter 5, so only a brief overview explaining the arrangement of optics is given here. The level scheme for $^{40}Ca^{+}$ can be found in figure 5.2.

These optics may be broadly divided into five main systems:

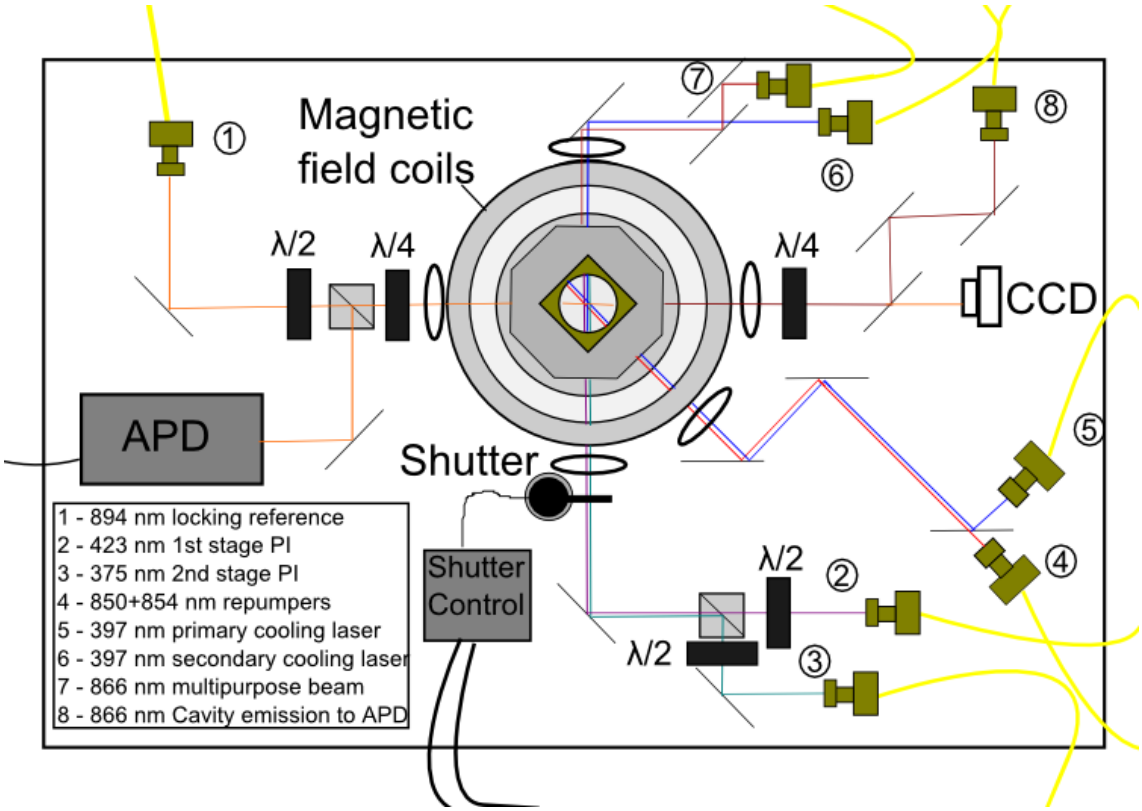

Figure 3.12: Lasers and optics in the trap plane.

1. **The Cs (894 nm) experimental-cavity locking system.**

   A stable reference laser (1) is coupled to the cavity to enable the cavity length to be locked. A mode-matching lens is used to ensure efficient coupling. The $\frac{\lambda}{2}$ waveplate is required to ensure maximal transmission at the polarising beamsplitter, while the $\frac{\lambda}{4}$ waveplate ensures that the polarisation of the reflected light has been rotated by $\frac{\pi}{2}$, and so the light reflected from the cavity may be collected without contamination from the ingoing light. The signal observed on the APD will be used to generate a feedback signal to lock the experimental cavity length. Coupling and locking are facilitated by the CCD to the right of the trap. This system is described in more detail in sections 4.3 and 4.5.

2. **The Photoionisation (PI) system.**

   Our photoionisation scheme is a 2-step process (using a 423 and 375 nm laser), and each beam is only effective in its area of overlap with the other. The two beams (2) and (3) are therefore overlapped spatially and in direction at a polarising beamsplitter (PBS) cube located close to the fibre couplers, by sending each beam into the splitter with orthogonal polarisations. They may then be aimed together at the centre of the trap, while both also being focussed by the same UV-coated lens. As

the photoionisation lasers have been observed to cause some charging effects in the trap, and because their wavelengths are relatively close to the 397 nm fluorescence wavelength such that they may represent an extra source of noise which is not entirely removed by the optical filters, these lasers are cut off when not in use (i.e. when the oven is not running) by means of an electronically controlled shutter. The shutter is controlled by a Data Acquisition card (DAQ). The photoionisation process will be described in more detail in section 5.1.

3. **The ion cooling system**

   Beams (4) and (5) are the repump and cooling lasers respectively. Beam (4) actually consists of two beams (850 and 854 nm) which have been combined before the fibre using a PBS in the same manner as the photoionisation lasers. As these beams already have orthogonal polarisations, it is not possible to use the same method again to overlap this beam with the 397 nm cooling beam. This would also be ineffective as the PBS must be anti-reflection coated for a narrow range of wavelengths and the wavelengths of these beams are too far apart, being in the IR and UV regions of the spectrum. Instead, a dichroic mirror which transmits IR light and reflects UV light can be used to overlap the beams as shown in the figure. The two mirrors following the dichroic mirror allow the position and angle of both beams to be scanned together while maintaining a good overlap. This is particularly useful when initially searching for the trap centre before ion fluorescence has been observed. The lens before the trap is UV-coated, as the spot size of the UV cooling laser is more critical than the IR repump lasers. Doppler cooling has been described in detail in section 2.2.2 and the practical implementation of this in our trap is further described in section 5.2.

4. **The secondary cooling system**

   Lasers (6) and (7) constitute another pair of cooling and repump lasers capable of maintaining the ion at a low temperature independently. They are used for a variety of functions. They provide a "backup" cooling system in case one or both of the primary cooling system beams becomes misaligned or defocussed; it is much easier to find the trap centre again if the secondary system can be used to cool ions there. The second 397 nm laser is not required for cooling if the first is on, as the beam (5) possesses components along each of the principal trap axes, but can be useful for measuring the variation in driven micromotion along a different direction (see section 5.4) in order to null stray DC voltages in the trap; it may also be detuned from resonance and used to precool a warm cloud of ions to the regime where it will

be effectively cooled by the primary cooling system (beams (4) and (5)), without contributing significantly to the heating or cooling of a cold ion crystal (see section 6.2.4). The repump laser is at 866 nm and addresses the $D_{\frac{3}{2}} \rightarrow P_{\frac{1}{2}}$ transition. It is not normally used to repump in experiments as it broadens the 397 nm transition and can result in dark resonances, while being a source of background for our cavity emission signal. However it can be used to identify the $P_{\frac{1}{2}} \rightarrow D_{\frac{3}{2}}$ transition frequency (section 5.6.1), to null the earth's magnetic field by observing the ground-state Hanle effect (section 5.5). Both lasers will be used to perform quantum state manipulation of the ion, as they are perpendicular to the cavity axis which will also be our magnetic field axis.

5. **The cavity emission collection system**.

Experimental (866 nm) fluorescence photons leaking from the cavity must be efficiently collected and channelled to a Single Photon Counting Module, while removing as far as possible background 894 nm photons from the lock reference. A mode matching lens is put in place and the output coupler optimised to the TEM_{00} mode, into which most cavity photons should be emitted due to the central location of the ion in the cavity and the symmetry of the system. The TEM_{70} locking mode is chosen to have little overlap with the TEM_{00} mode to help minimise coupling. A pair of dichroic mirrors is used to filter 894 nm locking light from experimentally interesting 866 nm light. These mirrors transmit 866 nm light with 85% efficiency while only allowing 0.01% of the 894 nm light to pass. This transmissivity is polarisation sensitive, so a $\frac{\lambda}{4}$ waveplate is used to linearise the circularly polarised locking light with a polarisation vector angle that will minimise reflection into the detection system. The layout of these dichroic mirrors has the added benefit that the majority of the locking photons can be passed through the first mirror to a CCD behind it so the resonant mode can be observed. The cavity TEM_{00} mode output is then coupled into an optical fibre using a third mirror. At the fibre output, further filters permit only 1 photon in 10^8 894 nm light to pass, while allowing 72% of 866 nm photons through. Two Single Photon Counting modules are currently installed in anticipation of future applications which will require both. These APDs have a 25 cps dark count rate, and the background from the cavity locking light is 75 cps, for a total background of 100 cps.

3.3.1 The fluorescence photodetection systems

While fibre-coupled APDs are used to detect cavity photons, the 397 nm cycling Doppler transition fluorescence is used to measure and diagnose the conditions of the ions. The detectors for these measurements are mounted on a second breadboard positioned above the majority of the components shown in figure 3.12. Its layout is shown in figure 3.13. It supports a Charge-Coupled Device (CCD) camera, a Photomultiplier Tube (PMT), and the requisite optics to focus light from the experimental plane of interest onto these. Mounted over the edge of the breadboard is a $\times 10$ magnification optical lens, which sits above the top window in the vacuum chamber and images the electrodes and trap centre. It is mounted on a 3D stage allowing x-position, y-position, and focus to be adjusted. A mirror mounted at 45° to the vertical plane reflects the image into the plane of the detection system.

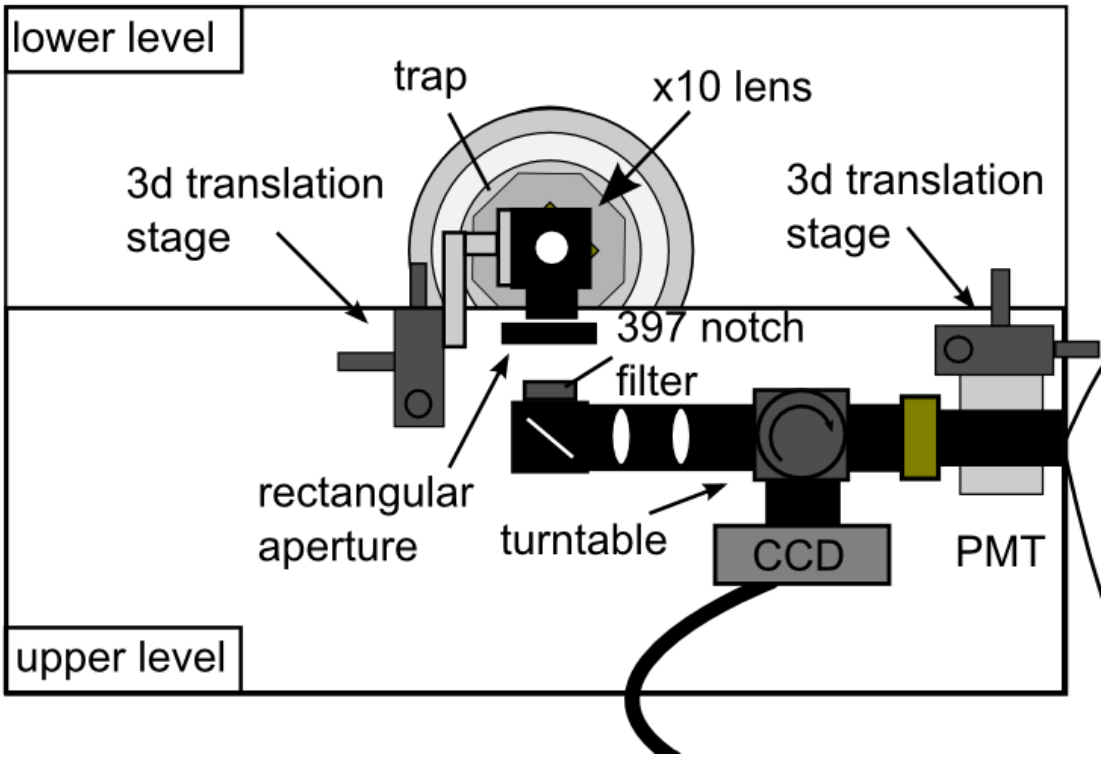

Figure 3.13: The layout of the photodetection optics above the trap plane.

The $\times 10$ lens focuses the plane at the trap centre, where ions are loaded, to a rectangular aperture formed of 4 razor blades, which remove out-of-focus scatter. A 397 nm notch filter removes light at wavelengths other than the fluorescence resulting from the Doppler cooling transition, though this may be removed to image the 423 nm fluorescence in the atomic cloud. The system beyond the filter is light-tight. It consists of a pair of

telescopic mirrors which refocus the image to the detectors. At a junction in the system, a turntable with a mounted mirror either reflects the light onto the CCD chip or permits it to pass to the PMT. The CCD and circular PMT aperture are equidistant from the turntable, so that if a focused image is formed on the CCD, the image will be focused at the PMT aperture, which further cuts down on background scatter. The CCD is a single-photon sensitive Andor Luca S. The PMT is mounted on a 3D translation stage to enable its proper alignment with the rectangular aperture. This is achieved by closing the rectangular aperture around the focussed image of an ion in the trap, and translating the PMT until the measured count rate is maximised.

Chapter 4

Lasers and Cavities

In addressing atomic transitions and collecting emitted photons from trapped atoms, we use laser and cavities which must be carefully frequency controlled and stabilised. These systems are the subject of this chapter.

4.1 Experimental lasers

All lasers used in this experiment are External Cavity Diode Lasers (EDCLs). They consist of a laser diode which receives optical feedback from a cavity to permit lasing at only a single frequency and to allow this frequency to be tuned over the range over which the mode is stable, known as the mode-hop free scanning range. Three of the systems we use (the 375, 423, and 850 nm lasers) were built in-house from basic components; two (the 854 and 793 nm laser and doubling system) are commercial products from Toptica Photonics. In all cases, the cavity portion is formed by a grating positioned so that the $n = -1$ order diffraction is directed back to the diode to provide optical feedback, while the $n = 0$ mode is extracted as the laser beam. This arrangement is known as the *Littrow configuration*, and is illustrated in figure 4.1. Reflection of the relevant beam back onto the diode is first achieved coarsely by adjusting the grating angle and position by hand, and then by tuning the grating angle by means of a screw that can tilt the grating armature.

The angle of this grating with respect to the laser diode can be controlled by a piezo-electric transducer (PZT) mounted behind the flexible armature on which the grating sits. By adjusting this angle, the wavelength fed back to the diode can be changed, therefore changing the lasing wavelength. Two other factors also influence the wavelength - the diode current and temperature. These are normally regulated by a purpose built laser-controller device.

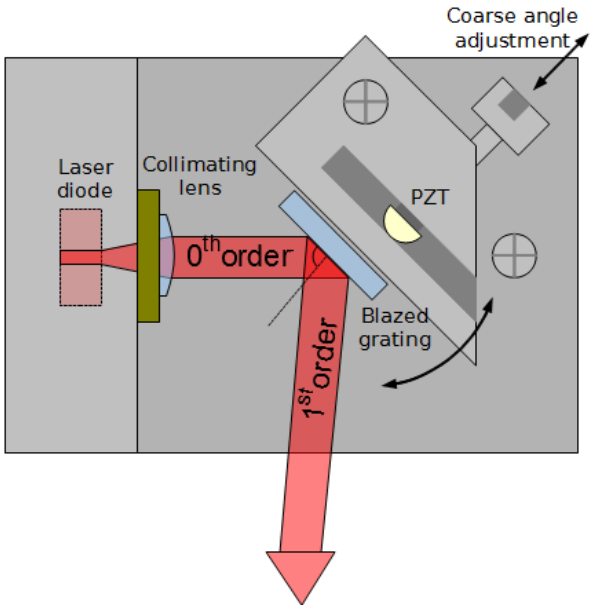

Figure 4.1: Schematic of the built in-house lasers in the lab.

The diode temperature is typically controlled by a Peltier element mounted close to the diode, and measured by either a thermistor or an AD590 temperature sensor. Temperature changes must propagate through the bulk laser mount material from the Peltier to the diode and temperature sensor. Unlike the piezo, therefore, which has a bandwidth of kHz, temperature changes occur on timescales of tens of seconds, and it may take minutes for the temperature to stabilise if feedback is being used. The temperature is usually kept fixed, ideally at a level close to the ambient temperature where small temperature fluctuations may be dealt with without straining the capabilities of the Peltier. Increasing the diode temperature increases the wavelength of a given mode. The current input to the diode typically has a bandwidth of several hundred MHz, making it the fastest form of feedback and also enabling the current input to be used for the purposes of generating sidebands, the uses of which will be discussed more in section 4.3. Increasing the laser current also increases the wavelength of a given mode.

For most experimental purposes a properly tuned diode can provide much more laser power than is required. This means that a single laser may supply power to several different endpoints, if the light in the beam can be split. Light emerging from a laser typically has a fixed linear polarisation, and a slightly elliptical beam profile. This ellipticity is corrected by using a pair of cylindrical lens to ensure good mode-matching to any optical fibres or cavities we wish to couple to.

4.1.1 AOM control

In some cases we want to be able to change the intensity or frequency of a laser during the experiment, and so it is coupled to an Acousto-Optic Modulator (AOM). An AOM is a device which takes two inputs: one a beam which passes through an optical crystal inside it, and another an oscillating voltage which produces phonons of the same frequency as that voltage oscillation within the crystal. This oscillating voltage is supplied by a Voltage Controlled Oscillator (VCO), a device which produces an oscillating voltage, the frequency and amplitude of which may be controlled by applying a DC voltage to its inputs. AOMs work most efficiently on beams with a small waist size, so focussing the beam to a small spot at the centre of the device is desirable.

In the case of the frequency-doubled 397 nm cooling laser, we want to be able to control not only the amplitude of the beam, but also the frequency. We can use an AOM to achieve both these objectives; however, the deflection of the non-zero orders from the AOM is frequency dependent. This means that if we pass our beam only once through the AOM, any coupling further ahead will dramatically change if we vary the frequency. To address this, the beam passing through the AOM must be reflected back through the same AOM (the so-called double pass configuration) so that any deviation in the beam angle may be corrected. As will be seen in section 5.6, a small positional shift does still occur, but it is not large enough to entirely decouple the laser from the fibre coupler. An overall coupling efficiency of around 30 % may be expected for the double-pass configuration. As the output beam will occupy the same space as the input beam, a polarising beamsplitter and quarter-wave plate must be employed to separate the output beam from the input. This setup is illustrated in figure 4.2. The maximum frequency shift that can be applied to a laser using the first order spot produced by the VCOs and AOMs in the lab is ± 200 MHz.

If polarising beamsplitters are used in the power distribution section, two beams of orthogonal polarisation may be combined in the PBS and be simultaneously coupled to one single-pass AOM and fibre coupler. This configuration is used for the 850 and 854 nm repumper lasers, which are close enough in wavelength to travel through a single fibre and must be spatially overlapped to be effective, minimising the number of fibres and couplers required and simplifying the optics needed to overlap the beams at the trap. As we do not need to vary the repumper frequency using the AOM, there is no problem with coupling to the first order of the AOM output in single-pass configuration. It enables us to quickly switch the repumpers on and off through the VCO's amplitude input, which can used

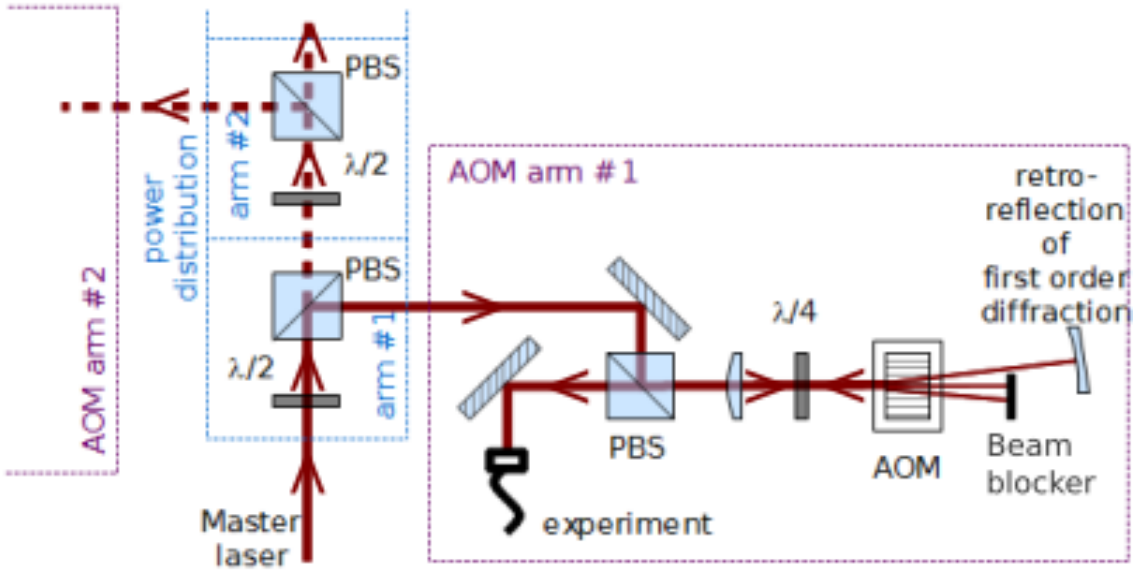

Figure 4.2: Schematic of the laser power distribution system using a double-pass AOM configuration [46]. In a single-pass configuration, AOM is followed by a coupling mirror and a fibre-coupler rather than a retroreflecting mirror.

during pulsed measurements when we only want to drive a single transition within a given timeframe.

4.2 Laser locking

The various lasers and cavities used in this experiment have different stability requirements: the first stage photoionisation laser must only be close enough to resonance to drive the transition sufficiently to ensure ionisation occurs, and the laser may be at high power to facilitate this. The $S_{\frac{1}{2}} \rightarrow P_{\frac{1}{2}}$ 397 nm laser, when used to drive a cavity Raman transition, must be stable to within the linewidth of the experimental cavity, i.e. to 475 kHz. We employ two different feedback mechanisms depending on the required level of stability. Figure 4.3 shows schematically the schemes used to stabilise these systems.

As stated in the previous section, the laser wavelength is dependent on several factors, all of which are prone to drift and to cause a drifting wavelength. This drift must be eliminated to within acceptable bounds for the experiment. Generally, this requires obtaining an *error function* which describes the size and direction of the deviation of the system from resonance, and further feedback electronics to convert this signal into feedback.

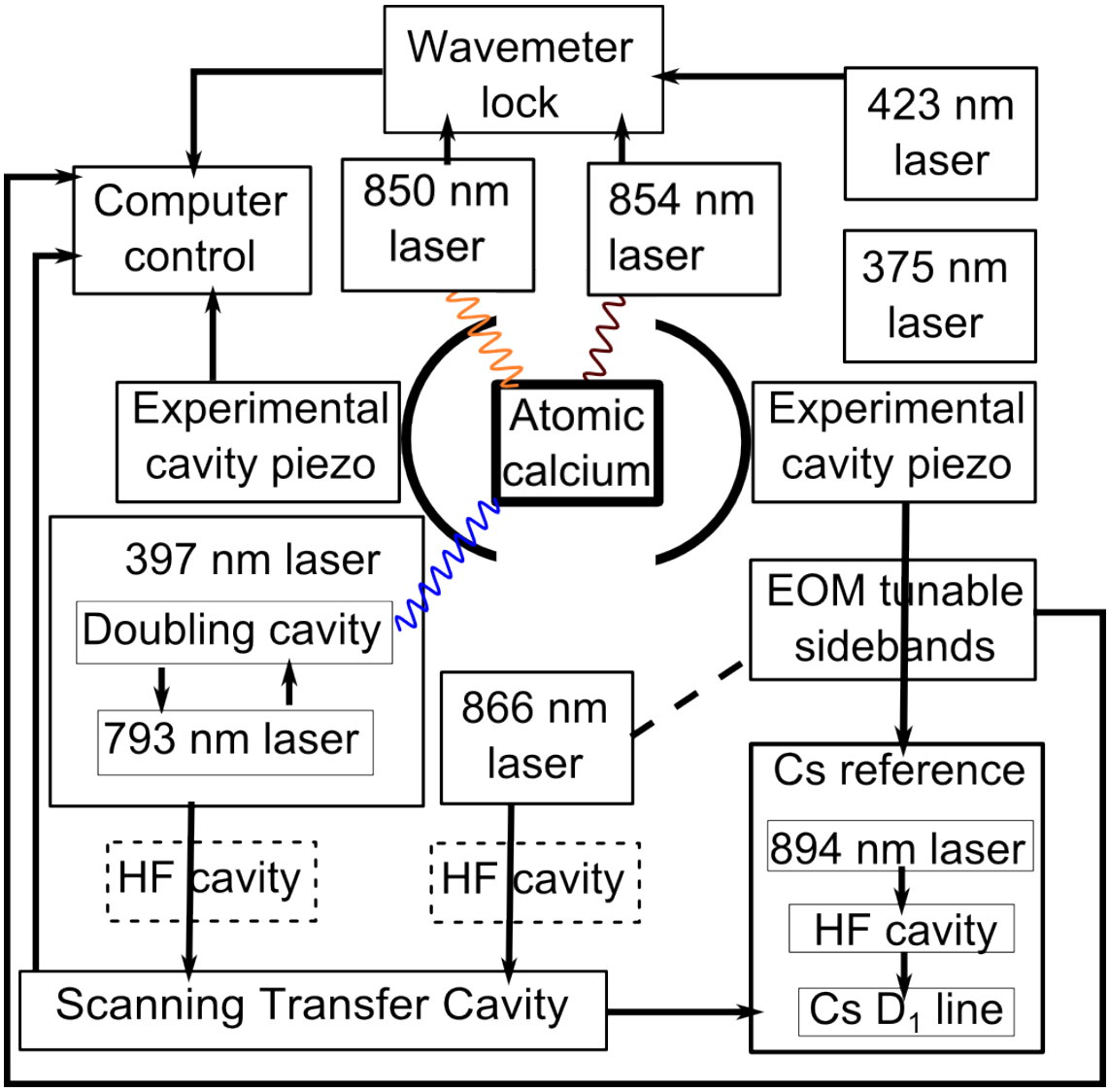

Figure 4.3: The relationship between the various frequency systems used in this experiment. The HF cavities shown in dashed boxes are to be implemented in the near future.

4.2.1 PID feedback

The error signal alone is not generally sufficient to provide useful feedback to a system; gain must be applied or the amplitude may have to be inverted to make it a useful signal, and feedback is most useful if it takes into account not only the instantaneous offset but the overall trends. To this end PID (standing for proportional, integral, and differential) feedback is used. The proportional element of the feedback is a scaled version of the error signal, and this is useful for combating deviations on a frequency of the combined bandwidth of the error signal generation and feedback circuits.

Proportional feedback is not useful for compensating small, constant offsets from resonance, as the signal is by definition small for small deviations. In addition, the response

function of the system is rarely linear or equal across all bandwidths. In order to compensate long-term drift and small, constant offsets in the system, integral feedback is used. This is implemented by passing the signal independently to an integrator circuit. If the system begins to linger on one side of the target value for longer than the other, the integral feedback will increase or decrease to return it to resonance.

Differential feedback attempts to account for the delay between the signal deviation and the feedback being applied (the phase delay) by monitoring the slope of the error signal and applying a compensating voltage based on that gradient. In practise for our purposes differential feedback is generally not required and only PI feedback is used.

PID mechanisms may be implemented in hardware on in software; the wavemeter and scanning cavity lock systems about to be discussed use a programmatic implementation of PID feedback, while the direct locking of cavities to lasers or lasers to cavities use hardware circuits such as that shown in figure 4.4 [46].

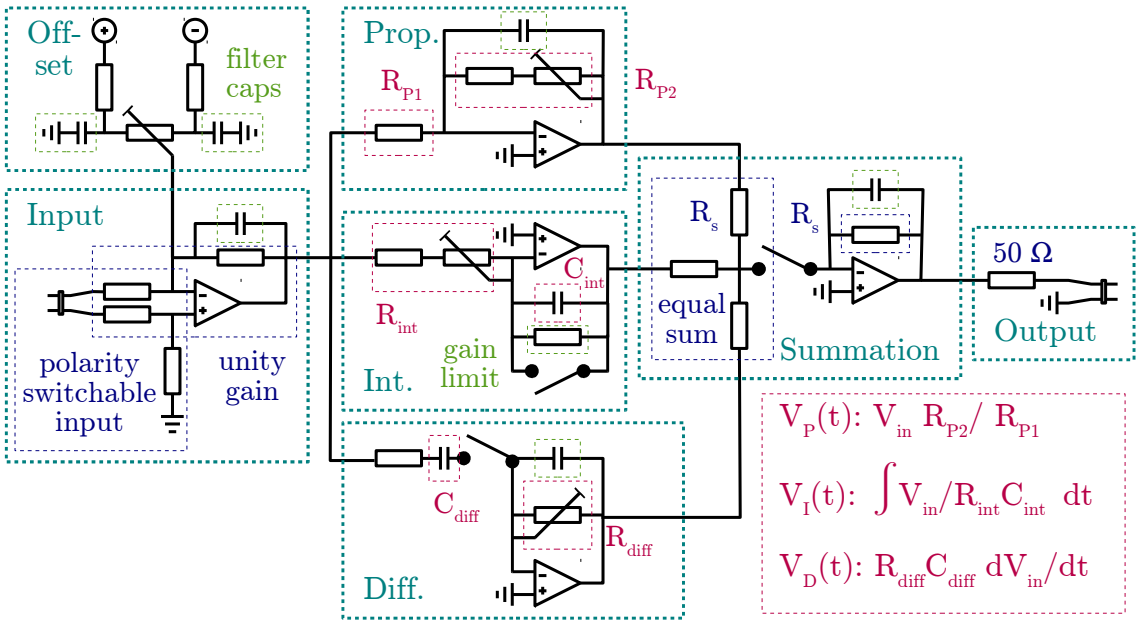

Figure 4.4: Schematic of a PID circuit used for feedback.

4.2.2 The wavemeter lock

Each of our lasers except the 375 nm laser is monitored by a wavemeter, which possesses accuracy of 60 MHz. The value measured by the wavemeter may be extracted from the wavemeter process' memory and fed into a LabView program, which measures the deviation of the measured wavelength from a set value, and generates a feedback signal using a PID algorithm. This feedback goes to the grating piezo control to correct the

frequency. The wavemeter is calibrated daily and before any important experiment using a Helium-Neon standard source in order to remove any systematic frequency measurement offset.

4.2.3 The transfer cavity lock

For applications which require more precise control of the laser wavelength (such as Doppler cooling or identification of the 866 resonance frequency (Section 5.6.1)), a more sophisticated lock must be used. A scanning transfer cavity allows the frequency stability of a reference laser to be transferred to the other lasers. We use an 894 nm laser locked to a caesium transition (see section 4.4) as our stable reference. The stability transfer is implemented in our lab as follows [48]:

1. The stable reference and all lasers to be locked to it (practically up to four or five) are coupled to a confocal cavity of length 250 mm using the setup shown in figure 4.5 [46]. Transmission is measured by a photodiode at the cavity output.

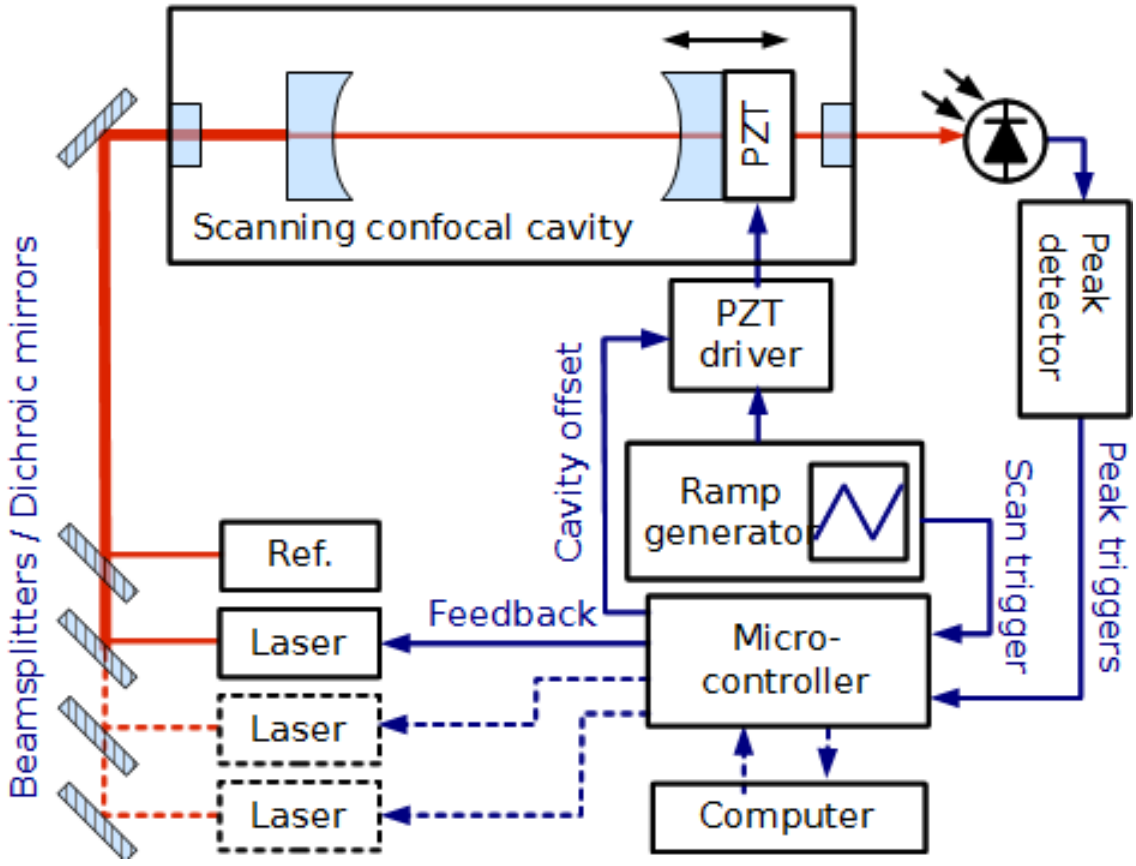

Figure 4.5: Schematic of the scanning cavity stability transfer locking system. The frequency of the experimental lasers are measured relative to a stable reference and feedback is generated to ensure these remain constant. [46]

2. The cavity is scanned across a free spectral range, with two peaks of the 894 reference visible and no peaks overlapping. The blue trace in figure 4.6 shows the cavity piezo voltage. The blue trace shows the cavity transmission.

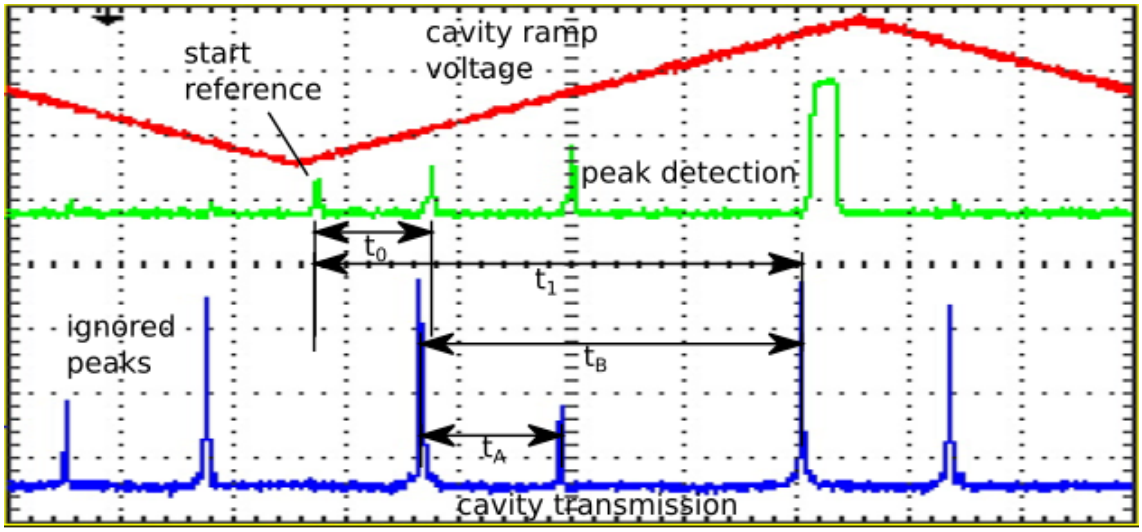

Figure 4.6: Detection and labelling of peaks by the scanning cavity. The large peaks at either end of the voltage ramp are 894 nm reference laser transmission, and the smaller peak in the centre is light from a 793 nm laser to be locked to the reference.

3. An external ADWIN GOLD DAQ system detects the peaks and generates a reference signal which labels the peaks by generating pulses of increasing height as peaks are detected across a sweep of the cavity length. This is the green trace in figure 4.6.

4. The ratio of the time-interval between the scan start and the first and second reference peaks are measured as t_0 and t_1. By feeding back to the cavity to keep $\frac{t_0}{t_1}$ constant, the cavity length will be kept the same.

5. The time interval between the first reference peak and each laser (t_A) to be locked is measured, and recorded as a fraction of the time interval between the two reference peaks t_B.

6. A PI feedback signal is generated from the deviation of this ratio from that originally recorded and sent to the relevant laser. The error signal may be described as

$$\Delta r = \frac{t_A}{t_B} - r_0, \tag{4.1}$$

where r_0 is the initially recorded ratio. Δr can then be manually adjusted to tune the laser frequency.

This system compensates long-term drift of the lasers effectively, but is limited in bandwidth as it scans at a rate of 1 kHz and has a Finesse between 70 and 120 for wavelengths between 780 and 894 nm. The -3 dB bandwidth for the feedback signal is 380 Hz [48].

Further developments in the stabilisation of these lasers is underway, in implementing a scheme whereby the lasers are locked to high-finesse $O(\sim 1000)$ cavities in vacuum for short-term, linewidth narrowing stabilisation, while the high finesse cavities are locked to the scanning transfer cavity for long-term drift compensation. The lasers will be locked to these high-finesse cavities using the technique described in the next section.

4.3 Cavity and laser locking with the Pound-Drever-Hall technique

Sections 4.2.2 and 4.2.3 refer to feedback generated from an error signal which is given by the deviation of a measured frequency from a target frequency. In order to implement locks of higher bandwidths, a different technique which does not depend on measurements taken on the order of Hz is required. A widely used scheme is that developed by Ron Drever based on the earlier work of R. V. Pound while in the group of Jan Hall, in which an error signal of the form shown in figure 4.7 [46] is generated from the reflection of a laser from a cavity. This technique is known as the Pound-Drever-Hall technique (PDH).

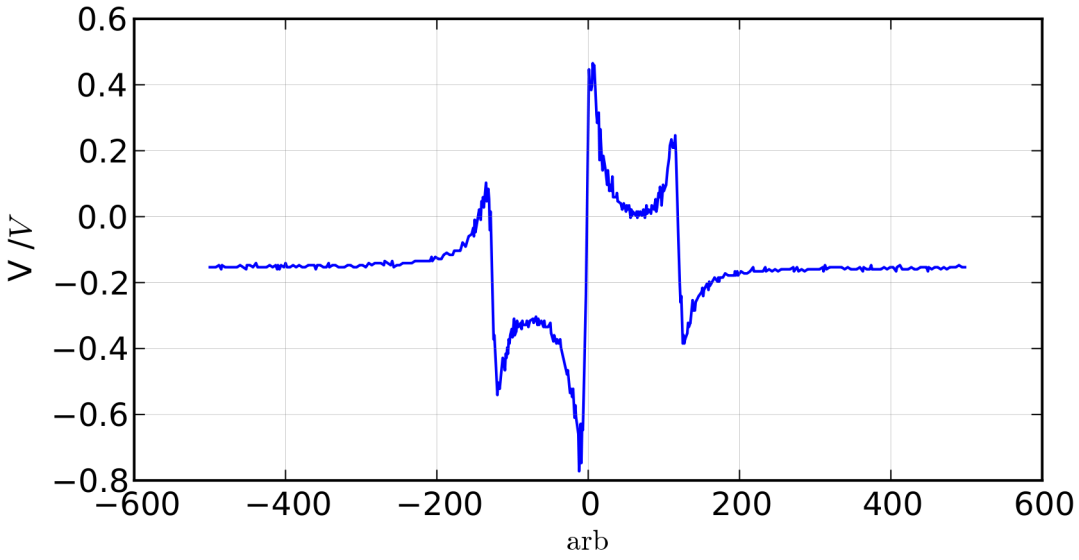

Figure 4.7: The form of the PDH error signal. [46]

In this technique, the laser phase or amplitude is modulated at an RF frequency ω_{RF} greater than the combined laser-cavity linewidth Γ to generate sidebands at $\pm\omega_{\mathrm{RF}}$ from

the carrier frequency. These sidebands are reflected from the cavity when it is on resonance with the carrier, and the beating of the sidebands is monitored by a photodiode. A mixer extracts the amplitude of the signal oscillating at ω_{RF}, which yields the error signal. If the power in the laser carrier and sidebands are denoted by P_c and P_s respectively, and the complex reflection coefficient R is frequency dependent (as it clearly is in the case of a system close to resonance), the reflected amplitude at ω_{RF} is given by:

$$\epsilon = 2\sqrt{P_c P_s}\mathrm{Im}\left[R(\omega)R^*(\omega+\omega_{\mathrm{RF}}) - R^*(\omega)R(\omega-\omega_{\mathrm{RF}})\right], \tag{4.2}$$

if the carrier frequency is ω. We know from the Kramers-Kronig relations that we can expect the phase and hence $\mathrm{IM}\left[R(\omega)\right]$ to pass through 0 at resonance, and indeed we find that within the linewidth Γ of the laser the amplitude of ϵ varies linearly, and within $\pm\omega_{\mathrm{RF}}$ is of a consistent sign to generate a feedback signal that drives the system back to resonance. Deviations from resonance of less than around one linewidth can therefore generate a linearly proportional error signal which will keep the system locked.

In order to collect the reflected signal from the cavity, light incident on the cavity will often pass through a polarising beamsplitter. As it travels toward the PBS, its polarisation axis will be aligned using a $\frac{\lambda}{2}$ waveplate, so that all the light passes through the cube. It will then pass through a $\frac{\lambda}{4}$ waveplate, which circularises it, before being reflected off the cavity and travelling through the same $\frac{\lambda}{4}$ waveplate, now with its polarisation axis rotated by $\frac{\pi}{2}$. It will then be reflected at the polarisation beamsplitter rather than continuing to travel along the path of the incident light, and can be collected by a photodetector (see figure 4.8).

4.4 The stable Cs reference cavity

In 4.2.3 a stable reference laser was referred to as providing a basis for the stability of the most frequency-sensitive lasers in the lab. This laser is locked to a high finesse optical cavity, which is in turn locked to the Lamb dip on the D_1 line at 894 nm in Doppler-free caesium spectroscopy. It is also used as the stable reference for the experimental cavity due to its stability and frequency separation from the 866 nm calcium fluorescence into the cavity. This shall be described in more detail in section 4.5.

The optical setup for the caesium reference laser is shown in figure 4.9 [46]. There are two main components to this system: the high finesse cavity (top left), which feeds back to the laser, and the saturation spectroscopy (bottom centre), which feeds back to the cavity. Sidebands at 10 MHz are generated by oscillating the current input. In order to

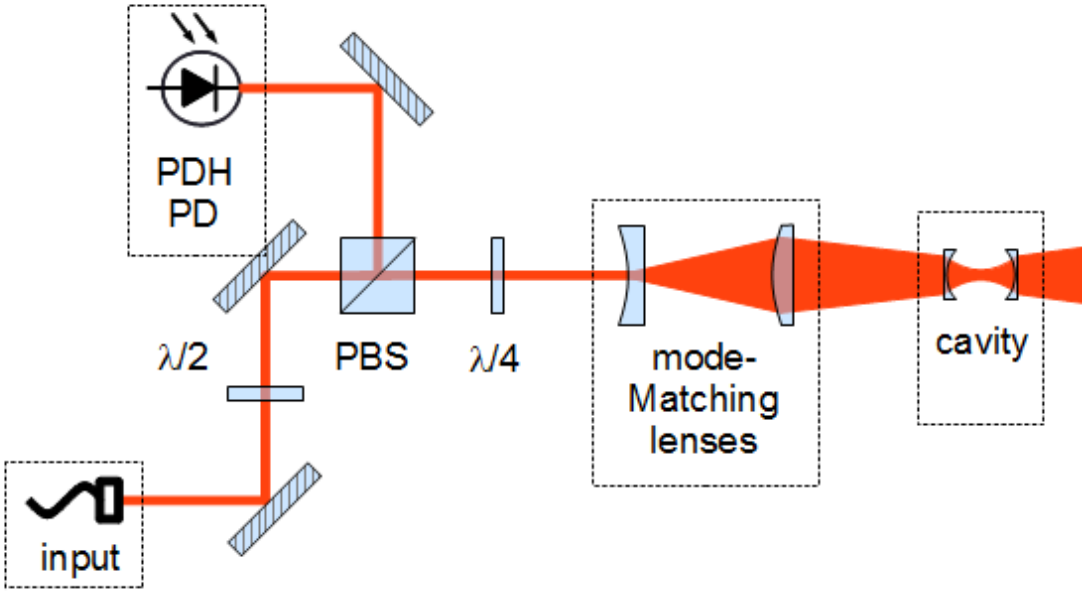

Figure 4.8: The typical optical setup for PDH locking.

shield the system from thermal, mechanical, or acoustic disturbances within the lab, it is mounted on a stabilising stage and surrounded by a heavy wooden box, coated with an inch of foam on the interior.

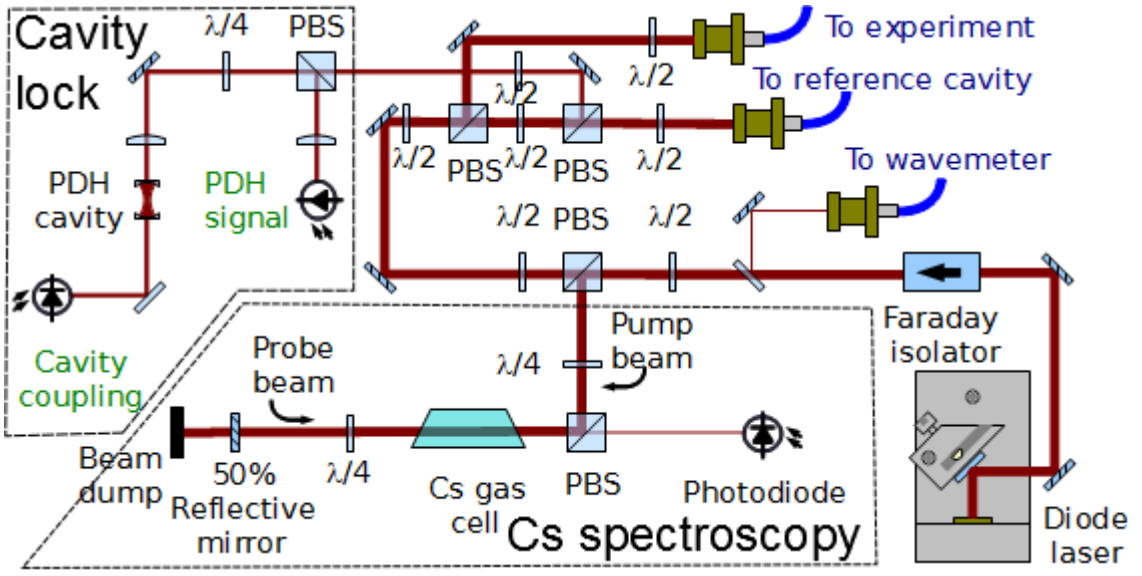

Figure 4.9: The optical setup of the stable Cs reference laser.

In the first step of locking the system, the 894 nm laser is tuned to the Cs resonance wavelength of 894.60530 nm, in the centre of a mode-hop-free scanning range. The wavelength is measured by a wavemeter using light picked off using a glass wedge plate just after the Faraday isolator. The TEM_{00} mode of the cavity is brought into resonance

with the laser at this frequency. A field programmable gate array (FPGA) switches from scanning across the resonance, allowing the transmission amplitude to be verified, to locking to the PDH error signal once the lock is engaged and a peak is detected. PI Feedback is initially sent to the current input of the laser, however over long periods drift may require large constant feedback signals to be applied. These would result in a changing laser power, and potentially a shortening of the lifetime of the laser diode if high currents were involved. The feedback signal is therefore fed through another PI circuit to the piezo grating angle control. The bandwidth of the grating piezo is much lower than the current bandwidth of the laser, but will compensate long-term drifts without resulting in changes to the average laser current.

Once the laser is locked to the cavity, no adjustment of the frequency via current, temperature or grating angle is possible, as the feedback system will act to resist such a change. Instead the laser frequency may be tuned over the mode-hop-free scanning range by changing the cavity length. The cavity is stable on short timescales, and hence locking to the cavity will eliminate high-frequency noise. The cavity is subject to drift due to thermal changes in the lab. Therefore a stable external reference is required to maintain a constant cavity length and laser frequency.

Saturation spectroscopy is carried out using a 75 mm caesium vapour cell with angled mirrors to prevent internal reflections. The caesium spectrum is an absolute frequency reference uniquely defined by the atomic properties of caesium, and is insensitive to environmental conditions. As the laser frequency is swept across the Cs D1 line resonance, a Doppler-broadened spectrum is observed. By driving the transition instead with two counterpropagating beams, one high power (above saturation) "pump" beam and one low power "probe" beam, a narrow spectral feature known as the *Lamb dip* may be extracted from the absorption spectrum of the probe. When the laser is red (blue) shifted, the pump and probe beams address different ions, which are moving toward (away from) the direction of each counterpropagating laser. On resonance, each laser addresses only atoms with no velocity component along the counterpropagating laser directions, and so compete for the same population. The high intensity pump laser saturates the transition, meaning that there is no population available to absorb photons from the probe beam, resulting in a dip (the Lamb dip) in the absorption spectrum as shown in figure 4.10. A PDH error signal is generated from the Lamb dip, using the same 10 MHz sidebands that the cavity lock PDH signal uses. P and I locking is engaged manually as the cavity length is slowly changed while the error signal is observed on an oscilloscope. This locks the laser. The

linewidth of the output laser is 50 kHz.

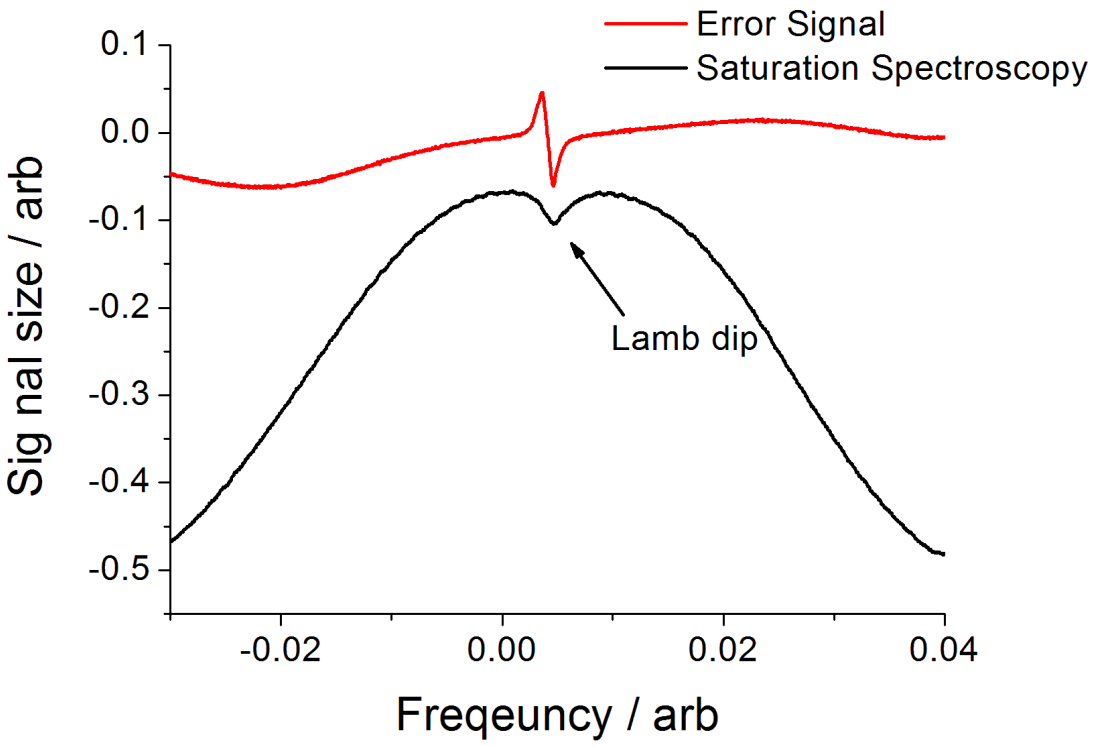

Figure 4.10: Saturation spectroscopy of the caesium D1 line.

The stable reference laser is collected by two fibre couplers, which conduct the light to the transfer cavity described in section 4.2.3, and into an Electro-Optical Modulator (EOM) which carries the light to the experimental cavity.

4.5 The experimental cavity

This cavity, as described in section 3.1.5, is situated deep within the trap. The mirrors are mounted on piezos controlled by voltages passing through the trap feedthroughs and filter systems 3.2.2, and optical access is afforded through the chamber windows and spaces included in the trap mount structure. Residing in vacuum, it has a very high stability, with a positional drift of 9 pm over 0.4 s. The cavity parameters are listed in table 4.1.

The cavity must be tuned to resonance with the transition of interest, and stabilised to within the linewidth of the Raman resonance (~ 1 MHz). It must also be possible to smoothly adjust the cavity length while maintaining a lock to an external reference. Light from the caesium reference laser is directed onto the low transmissivity (5 ppm) cavity

Cavity Parameter	Value
reflectivities	100 ppm and 5 ppm
radii of curvature	1”
length	5.25 mm
1 Free Spectral Range	28.6 GHz
$\mathcal{F}$	60,000
g	0.9 MHz on resonance
κ	475 kHz
Γ	23 MHz on resonance
Cooperativity	0.074

Table 4.1: Table of the experimental cavity parameters.

mirror, as shown in figure 3.12. It is possible to lock the cavity to this light, but only at a fixed frequency, which is unlikely to correspond to the resonance of the experimental transition. In order to be able to tune the locking frequency, and hence the cavity length, additional tunable sidebands are applied to the reference light by modulating its phase in the EOM fibre that conducts it to the experimental cavity. Sideband frequencies of up to 1 GHz are achievable and are limited only by the bandwidth of the amplifier used. The modulation is generated by a Rohde & Schwarz signal generator, which is controllable through a GPIB port, so that the scanning of the frequency of these tunable sidebands may be automated.

When selecting a transverse 894 nm mode to lock the cavity to, there are several considerations. It must fall within 1 GHz of the 866 nm TEM_{00} mode. The selected mode should preferentially have an antinode at the centre or be of high order to minimise its spatial overlap with the TEM_{00} mode, therefore reducing the background light that will be coupled to the detection system. It should yield a PDH error signal which crosses 0 V only once, and is otherwise regular enough to lock to repeatably. While we can access 6 free spectral ranges from one extreme of the piezos' extent to the other, it is preferable to use a mode close to the centre of this range to maximise the distance over which the locked cavity may be scanned in space (see section 6.2.4).

Weighing up the above factors for the mode available in our cavity, we have selected the symmetric TEM_{70} (figure 4.12) mode located close to the centre of the available range. In order to identify the overlap of this mode with the experimental transition TEM_{00} mode, an 866 nm laser tuned to the wavelength identified in section 5.6.1 is shone into the cavity

from the high transmissivity (100 ppm) side as the 894 nm laser enters from the other side. The output of the PDH mixer is shown in figure 4.11. The feature on the left is caused by the 866 nm transmission through the cavity interacting with the off-resonant 894nm light mixed with the local oscillator as the cavity is scanned over its resonant frequency. The feature on the right is the Pound-Drever-Hall error signal generated by the 894 nm reflection at its resonance frequency. The frequency of the tunable sidebands is adjusted until these two features overlap. At this setting, the 894 nm reference laser is co-resonant with the 866 nm laser in the cavity. Fine-tuning of the cavity length to match the $P_{\frac{1}{2}} \rightarrow D_{\frac{3}{2}}$ 866 nm photons will be achieved using Raman spectroscopy (section 6.1).

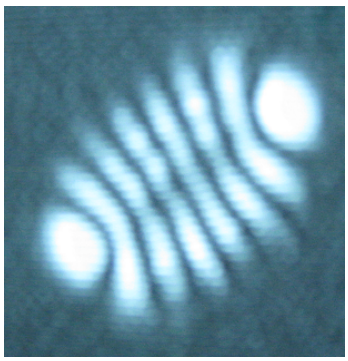

Figure 4.12: The TEM_{70} mode of the 894 nm laser used for locking the experimental cavity.

The tunable sidebands' only function is to define the frequency offset at which the experimental resonance is to be found; they do not contribute to the locking. Locking of the experimental cavity is performed using the PDH technique with the same 10 MHz sidebands which are used to lock the 894 nm laser to the reference cavity and the reference cavity to the caesium transition in the reference laser lock. The Rohde & Schwarz signal generator's amplitude is calibrated across 200 MHz around the central transition frequency to ensure that the sideband amplitude remains constant as the frequency is changed. At these amplitudes, the powers in the carrier and higher order sidebands are much less than the power in the first-order sidebands. Each of the first-order sidebands has an associated PDH error signal arising from the 10 MHz sidebands, which can be used to lock the cavity.

The cavity is locked to the 50 kHz linewidth reference signal, which is less than the cavity's own linewidth of 475 kHz.

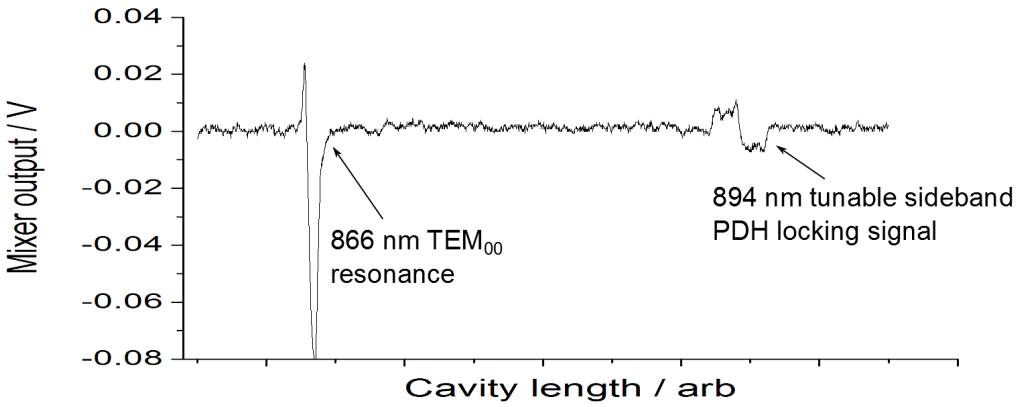

(a) 894 nm TEM_{70} tunable sideband lock signal 20 MHz from the 866 nm TEM_{00} mode resonance.

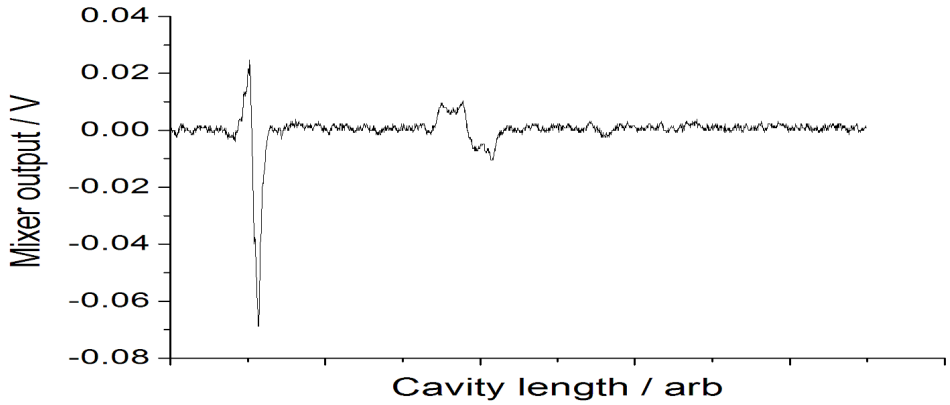

(b) 894 nm TEM_{70} tunable sideband lock signal 10 MHz from the 866 nm TEM_{00} mode resonance.

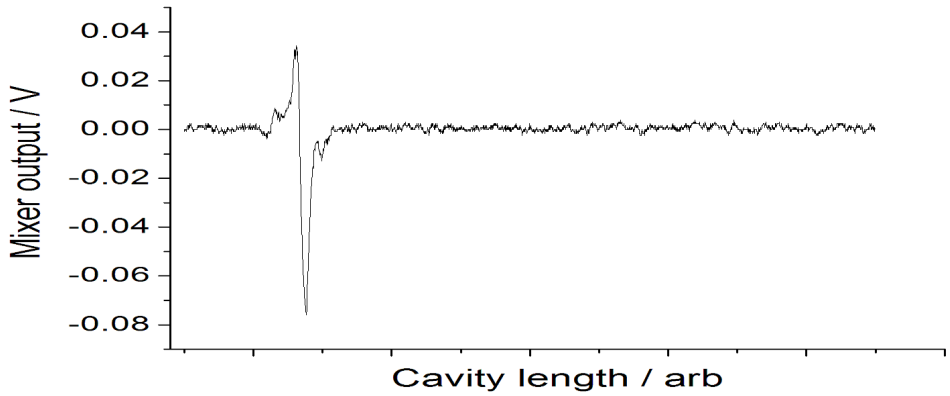

(c) 894 nm TEM_{70} tunable sideband lock signal overlapped with the 866 nm TEM_{00} mode resonance.

Figure 4.11: Overlap of the 894 nm tunable sideband with the 866 nm calcium resonance achieved by changing the sideband frequency.

Chapter 5

Operation and optimisation of the ion trap

The theory of ion trapping was discussed in section 2.1, the necessary hardware in chapter 3 and the requisite laser control systems in chapter 4. This chapter describes operation of the ion trap to load and store ions, and the measurements that can be performed to ensure the optimum ion stability and temperatures close to the Doppler temperature are being achieved. It begins with a discussion of loading and cooling ions before detailing the measurement of the trap secular frequencies, the compensation of stray electric and magnetic fields, and finishes with a description of the spectroscopic measurement of the full emission profile of the ion on either side of resonance.

5.1 Photoionisation of ^{40}Ca

In order to trap and position individual atoms to the degree required for our experiments, it is necessary to vaporise them from the bulk medium, and to ionise them so that they feel the electromagnetic force. Our atom source is the oven containing Calcium filings located within the trap beneath the vacuum chamber. The calcium is heated to the point of evaporation by passing a current of 1.4 A through a tungsten wire wrapped around the oven. The current heats the thin wire either side of the oven, which conductively heats the oven itself. The pressure within the vacuum chamber rises from $\sim 1 \times 10^{-10}$ mbar to $\sim 1 \times 10^{-9}$ mbar as calcium and impurities are evaporated. Once heating stops the pressure returns to the background level within ~ 1 s. It is preferable to run the oven at currents just high enough to load an ion in a reasonable amount of time - running at higher temperatures may lead to more ions than we want being loaded, some of which must then

be ejected. It also results in unnecessary coating of the electrodes in calcium deposits which leads to local DC potentials and micromotion (see section 5.4), and introduces the risk of quickly evaporating the entire contents of the oven requiring the trap to be opened, cleaned, and a replacement oven prepared.

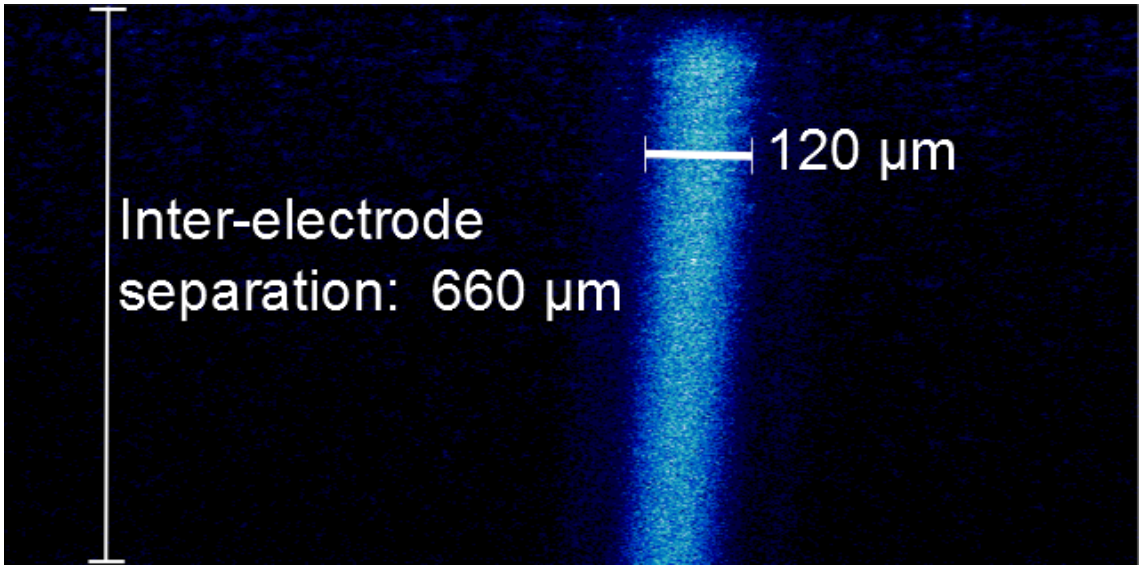

Figure 5.1: Fluorescence of the neutral ^{40}Ca $S_{\frac{1}{2}} \rightarrow 4P_{\frac{1}{2}}$ transition observed by shining the 423 nm first-stage photoionisation laser through the trap volume while the oven evaporates neutral calcium. The beam profile is visible throughout the extent of the trapping region, illustrating that the atomic cloud fills the trap. The 423 nm laser power is 4.5 mW, so it saturates the transitions of atoms close to the beam centre, so in this figure the Gaussian profile of the beam and the true beam waist are not apparent.

The evaporated calcium atoms are ionised by photoionisation once they have entered the trap region. This normally involves using a laser to impart a valence electron with sufficient energy to overcome the work function of the calcium atom and escape to the continuum. While most impurities would have the wrong charge to mass ratio to be trapped should they become ionised, the ^{44}Ca isotope is present in our sample with 2% natural abundance. If ^{44}Ca were to be ionised along with our ^{40}Ca, these would be trapped alongside our experimental ions, but would not be resonant with our cooling or state manipulation lasers due to the isotope shift. These "dark ions" are unwanted, as they do not fluoresce, and may jump around within a chain of ions resulting in an unpredictable and changing experimental structure.

In order to ensure only ^{40}Ca is ionised, a 2-step resonant photoionisation process is implemented using frequencies of readily available laser diodes. An excitation laser at 422.79167 nm is used to excite an outer electron of neutral ^{40}Ca from the $4S_{\frac{1}{2}}$ to the

$4P_{\frac{1}{2}}$ state. ^{44}Ca is not excited by light at this wavelength, and so remains in the ground state. A second laser at $\sim$ 375 nm non-resonantly promotes the excited ^{40}Ca valence electron to the continuum, leaving a singly-charged ion. The 423 nm and 375 nm lasers are overlapped before entering the trap, which they pass through at approximately the trapping centre, and are blocked by a mechanical shutter when they are not being used to avoid the possibility of charging components within the trap.

Figure 5.1 show the atomic fluorescence observed by removing the 397 nm notch filter in the fluorescence imaging system (figure 3.12) while atomic calcium is being vaporised in the oven and the 423 nm beam is passing through the trap centre. The atomic cloud fills the trap volume, and fluorescence from the resonant 423 nm transition can be observed throughout the laser volume. Observation of this fluorescence provides a simple confirmation that the oven and photoionisation stages of the experiment are working.

5.2 Cooling

Doppler cooling in a 2-level system by a single laser was described in section 2.2.2. However, in reality $^{40}Ca^{+}$ is not a 2-level system as the $4S_{\frac{1}{2}} \rightarrow 4P_{\frac{1}{2}}$ transition in Calcium is not a closed transition, but the P state may decay to the metastable $3D_{\frac{3}{2}}$ with a branching ratio of 8%. The D state has a lifetime of $\sim$ 1s, and if an ion becomes excited to this state it will not be cooled until it decays back to the $4S_{\frac{1}{2}}$ level. It is therefore necessary to "repump" the ion out of the D state and back into the cooling cycle. A laser at 866 nm could achieve this (and this repumper frequency is used, for example, in section 5.5,) but in our experiment repumping with 866 nm is undesirable as it may lead to an increased background or cause broadening of the transition. Instead, a laser at 850 nm is used to pump the ion from the $3D_{\frac{3}{2}}$ state to the $4P_{\frac{3}{2}}$ state. This state features a transition back to the $4S_{\frac{1}{2}}$ state with a lifetime of 7.7 ns, but it may also decay to the metastable $3D_{\frac{5}{2}}$ state. An 854 nm laser is used to repump ions from the $3D_{\frac{5}{2}}$ state to the $4P_{\frac{3}{2}}$ state, and the cycle is then closed and cooling may proceed indefinitely. A level diagram of the relevant transitions can be seen in figure 5.2 and a table of the relevant wavelengths is shown in 5.1. As described in section 4.1.1, the cooling laser passes through a double-pass AOM, and the repump lasers are passed through single-pass AOMs resulting in frequency shifts of 400 MHz and 200 MHz respectively. The wavelengths of all lasers involved in atomic transitions are described in table 5.1. The post-AOM frequencies listed are the true frequencies seen by the ion.

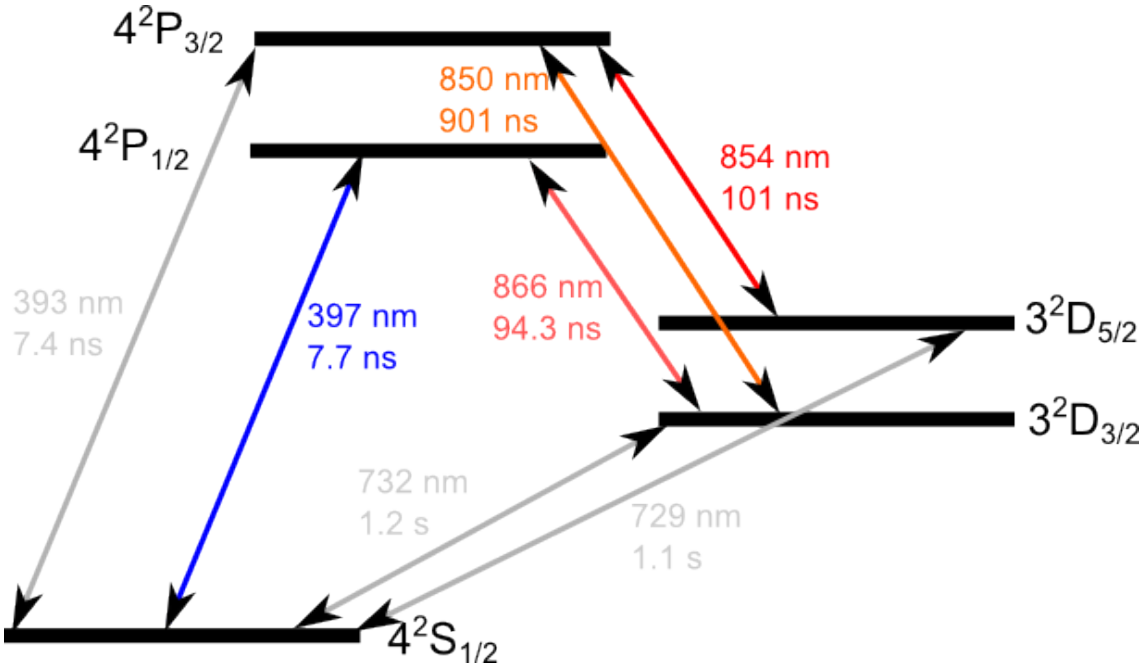

Figure 5.2: Level scheme of singly ionised $^{40}Ca^+$ showing the wavelength and lifetime of each transition. The laser-driven and cavity emission transitions are shown in colour. The 850 & 854 nm repumper scheme removes population from the metastable D states (lifetimes ~ 1 s) and puts them into the $4P_{\frac{3}{2}}$ state, which decays back into the $4S_{\frac{1}{2}}$ ground state of the cooling transition in 7.4 ns. [50]

When ions are trapped following evaporation, ionisation, and confinement by the RF field, the are initially at a high temperature and experience significant Doppler broadening. Therefore when loading, the cooling laser must be detuned from the optimal frequency of $\frac{\Gamma}{2}$ by an additional 70-100 MHz. This allows the ions to crystallise, and then the cooling frequency and power may be reduced to Doppler cooling levels.

Fluorescence from the $P_{\frac{1}{2}} \rightarrow S_{\frac{1}{2}}$ transition may be observed on the CCD and PMT. Figure 5.3 shows the various configurations of ions that may be trapped. Ion crystals occupy the most space and can be useful for aligning and focussing individual lasers at the trap centre.

Using secular frequency information obtained in the following section to determine the ion-ion separation, we can use these images to calibrate the camera scale: 1 pixel corresponds to a distance of 1 μm. This confirms previous measurements taken using the RF-electrode separation as a reference.

Laser	Wavelength / nm
Photoionisation	
1^{st} *stage*	422.79167
2^{nd} *stage*	<375
Cooling	
pre-doubling	793.91831-41
post-doubling	396.95916-20
post-AOM	396.95894-99
Repumpers	
$3D_{\frac{3}{2}} \rightarrow 4P_{\frac{3}{2}}$	850.03538
post-AOM	850.03490
$3D_{\frac{5}{2}} \rightarrow 4P_{\frac{3}{2}}$	854.44449
post-AOM	854.44400
$3D_{\frac{3}{2}} \rightarrow 4P_{\frac{1}{2}}$	866.45142
post-AOM	866.45092

Table 5.1: Table of the wavelengths used for the trapping of Calcium 40 in the cQED trap system.

5.3 Secular Frequencies

The confinement of the ions in the axial and radial directions can be described by the secular frequencies as described in equations (2.13) and (2.16). It is of interest to identify the q and a values involved, to determine where in the stable region of the Mathieu plot our ion lies, and to calculate the inter-ion separation which shall be important in section 6.2.4. The trap confinements are controlled by setting the endcap voltage ($U_{DC} = 0 - 650\,\mathrm{V}$), and the trap drive amplitude, which is proportional to a DAQ-controlled input voltage ($V_r = 0 - 5\,\mathrm{V}$). The secular frequencies are measured as these inputs are changed, and expressions for q and a can be obtained in terms of these voltages. As $q \propto U_{\mathrm{RF}} \propto V_r$ with a constant of proportionality dependent on the drive source, amplification, and trap-drive coupling, equations (2.7) and (2.8) can be rewritten as:

$$q = k_q V_r, \tag{5.1}$$

$$a = k_a \sqrt{U_{\mathrm{DC}}}. \tag{5.2}$$

The secular motion of an ion in the axial or radial direction may be driven by applying an oscillating voltage of the resonant frequency to the excitation plate described in section 3.1.4. The frequency of the oscillation is scanned until large amplitude secular motion of the ion is observed (figure 5.5). These measurements are carried out with a single ion to

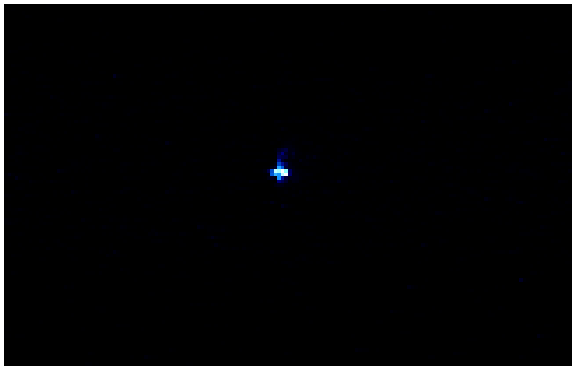

(a) A single trapped ion.

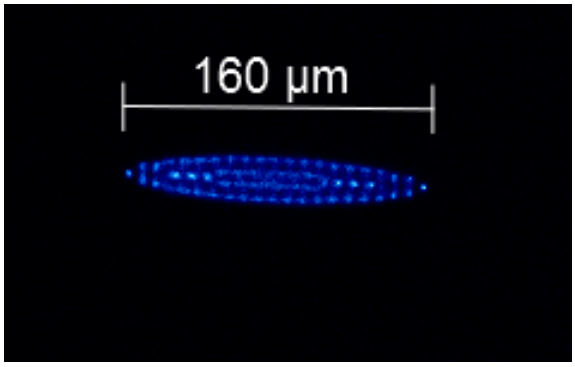

(b) A 3D ion crystal.

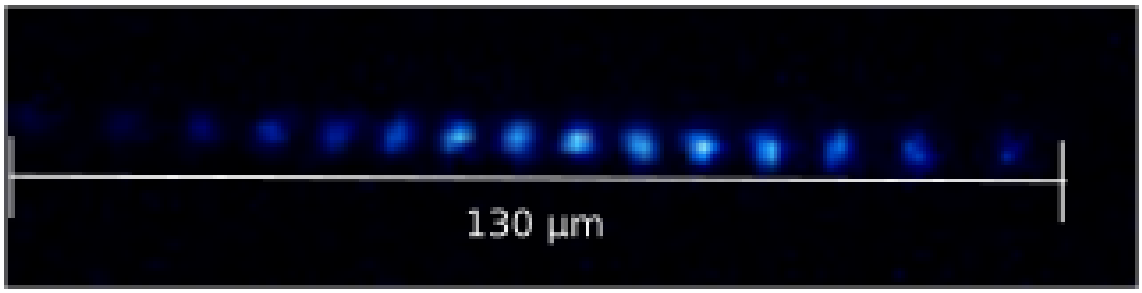

(c) A 1D ion string. The higher observable fluorescence of the ions at the centre of the string is due to the Gaussian profile of the cooling beam, which passes through the trap centre at an angle of 45°. Ions at the extremes experience a lower intensity of 397 nm light and hence fluoresce less.

Figure 5.3: Trapped ions in their three possible configurations. The images were taken with 0.1 s exposure time, EM gain of 255, and were scaled for a range of 0-1,500 counts per second. 1 pixel $\sim$ 1 μm.

avoid driving oscillations of higher frequency than the common mode motion, which would not provide an accurate measurement of the confinement. In general the radial confinement is much higher than the axial confinement, and so the axial secular frequencies of ~ 100 kHz are typically an order of magnitude lower than the radial frequencies of ~ 1 MHz.

These measurements are carried out across the range of available frequencies and the plots shown in figures 5.5(a) and (b) are obtained.

The additive constant of 22.2 V in plot 5.5b accounts for the contribution to the axial confinement from the radial trapping field's edge effects. Recalling equation 2.13 and assuming $a \ll q$, and using our trap drive frequency $\Omega_{RF} = 20.96$ MHz,

$$q = \frac{2\sqrt{2}\omega_r}{\Omega_{RF}}, \tag{5.3}$$

$$= \frac{2\sqrt{2}1.41V_r}{20.96}, \tag{5.4}$$

$$= 0.19V_r. \tag{5.5}$$

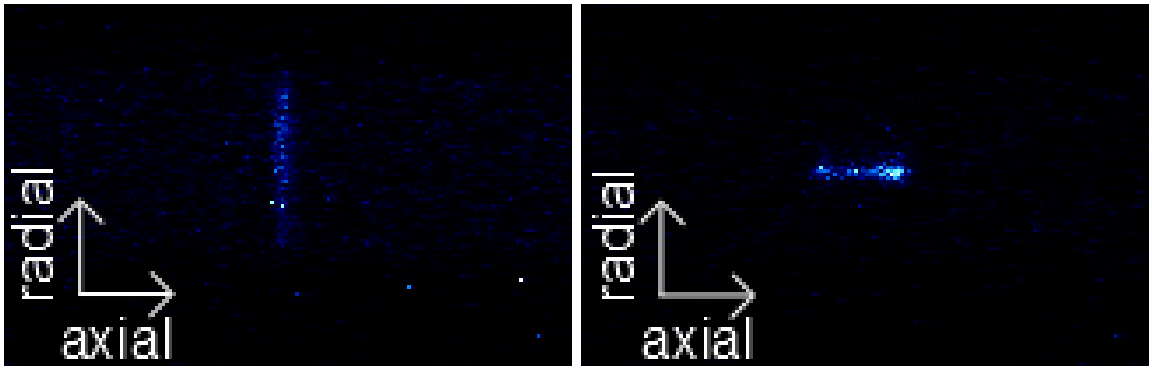

(a) A radially excited ion. (b) An axially excited ion.

Figure 5.4: Radial and axial oscillations being induced by a perturbation at the trap's secular frequencies.

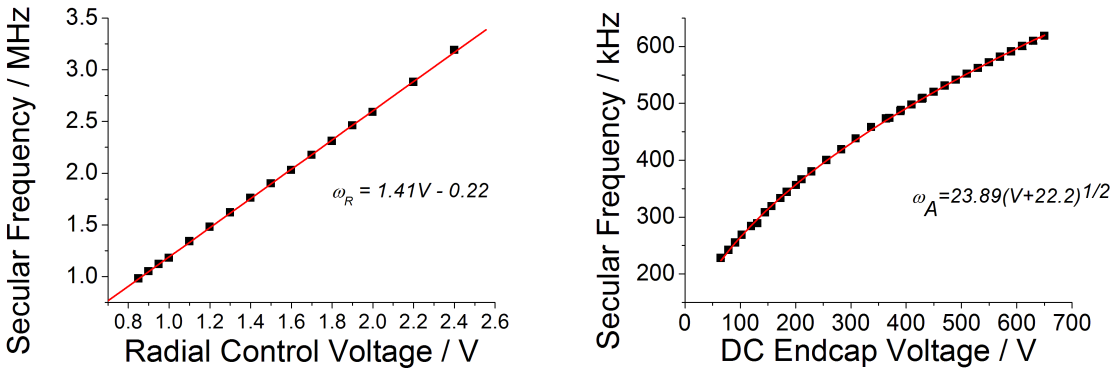

(a) The relationship between the radial secular frequency and the applied trap depth control voltage.

(b) The relationship between the axial secular frequency and the applied endcap voltage.

Figure 5.5: The trap secular frequencies in terms of the confinement voltages.

Therefore over the total range of $0 < V_r < 5\,\mathrm{V}$ we may set $0 < q < 0.96$.

From 2.16, we obtain

$$-a = 2\left(\frac{\omega_z^2}{\Omega_{RF}^2}\right), \tag{5.6}$$

$$= 2\left(23.89^2 \times \frac{(U_{DC} + 22.2)}{21960^2}\right), \tag{5.7}$$

$$= 1.2 \times 10^{-6}\,(U_{DC} + 22.2)\,. \tag{5.8}$$

The maximum U_{DC} value we can use without potentially damaging the trap feedthroughs is 650 V, therefore $-8 \times 10^{-4} < a < 0$.

5.4 Micromotion minimisation in 2 dimensions

We have seen from equations (2.11) and (2.12) that stray DC fields shift the ion from the trap centre and induce additional motion independent of the secular motion amplitude. This is known as micromotion. In order to minimise the amount of micromotion present, compensating DC fields must be applied to negate the effects of the stray fields and move the ion back to the RF trap centre. In our trap, each RF electrode is also connected to a DC input. By applying the correct voltage changes to all 4 electrodes, the ion may be translated horizontally and vertically (45° to the electrode directions) as this is what is most easily observed in the fluorescence detection coordinate system. As these stray fields result from charging of dielectrics by the lasers, coating of electrodes by effused calcium, and external sources in the lab, they are subject to vary on a daily basis, and so micromotion minimisation must be carried out before any experimental work can begin.

A number of schemes exist for detecting and minimising micromotion. The most intuitive is the visual scheme, in which the trap depth is oscillated at a few Hertz and the ion can be seen to move in phase with the oscillation as it is pushed toward the trap centre as the trap depth increases, and falls back outward as it decreases. If we view the trapped ion from above, we can adjust the horizontal DC offset until the ion no longer moves - once located at the centre of the trap, it does not see the effect of the increasing or decreasing trap depth. This scheme is fast and effective for minimising the horizontal component of the stray electric field, but as we cannot image our ion from the side we cannot use this to compensate the vertical offset of the ion from the trap centre.

5.4.1 Correlation measurement and minimisation of micromotion amplitude

The most quantitative method we have available for determining the degree of micromotion present involves taking a correlation measurement of the trap drive and the photon emission. In one dimension, an ion being accelerated toward and away from a laser by the trap drive will exhibit an emission profile based on its direction and the amplitude of the micromotion. While being accelerated toward the red-detuned cooling laser, the ion will see the light as blue shifted, and be more likely to scatter a photon. While being accelerated away from the red-detuned laser, it will see the light as further red-shifted and hence be less likely to scatter a photon. By measuring the time since the beginning of one trap drive oscillation until the collection of a scattered photon on our PMT, a profile may be built which describes the ion's velocity as a sine wave. One such profile, measured

across 4 periods of the trap drive, is shown in figure 5.6a.

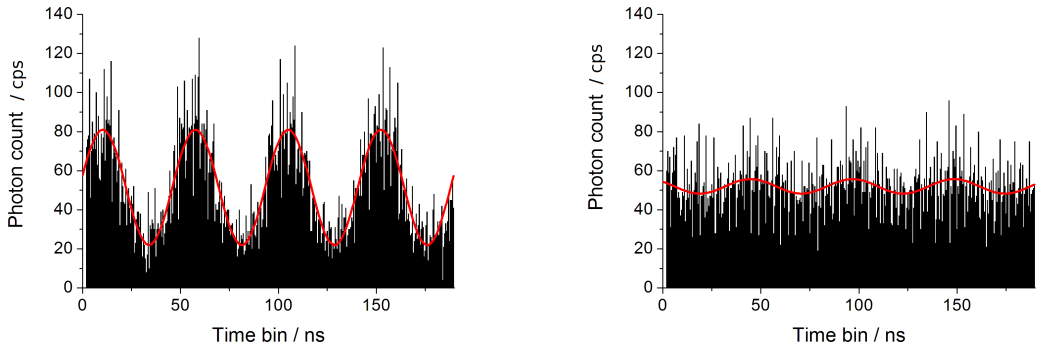

(a) Measurement of the correlation between the trap drive oscillation and the atomic fluorescence showing the presence of trap-driven micromotion in the direction of the laser.

(b) Measurement of the correlation between the trap drive oscillation and the atomic fluorescence once the driven micromotion has been reduced.

Figure 5.6: Detection of a micromotion using the correlation method.

Note the offset from the x-axis is caused by the fact that the scattering rate does not drop to zero even as the ion is accelerated away from the laser. The frequency of the oscillation matches the trap drive frequency. The larger the amplitude of the sine wave, the greater the micromotion. As the ion is brought toward the trap centre by a compensating field, the amplitude reduces to zero as in figure 5.6b, and if the ion should pass out of the trap centre in the other direction, the amplitude will grow but the oscillation will be π out of phase.

This scheme will only compensate the micromotion along the direction of the laser - that is, the micromotion due to the DC field perpendicular to the laser. No correlation amplitude will be observed if there is only micromotion perpendicular to the laser. Therefore, two non-parallel lasers are required to effectively compensate the micromotion in two dimensions using this scheme (and three for three dimensions - we assume the micromotion in the axial direction is small and so can be neglected.) At the point where no sine-wave can be observed in the correlation measurement when illuminating with the laser in either direction, the ion is located at the trap centre.

We may also automate the location of this point. By illuminating the ion with one laser at a time and applying a given horizontal potential, the applied vertical potential can be varied and the point where the amplitude of the micromotion crossed zero can be recorded. The horizontal potential is then increased incrementally, and the measurement is repeated for several steps. This produces a line defining the position of the micromotion

minimum in the direction of that laser. The ion is then illuminated with the other laser and the experiment is repeated to obtain a line defining the location of the micromotion minimum in the direction of the second laser. At the point where these lines cross, no micromotion can be observed in either direction, and as these lasers are not parallel (in our trap the maximum angle that could be achieved between the lasers was 14°), there is no micromotion in this plane and the ion is located at the trap centre. A plot demonstrating this is shown in figure 5.7.

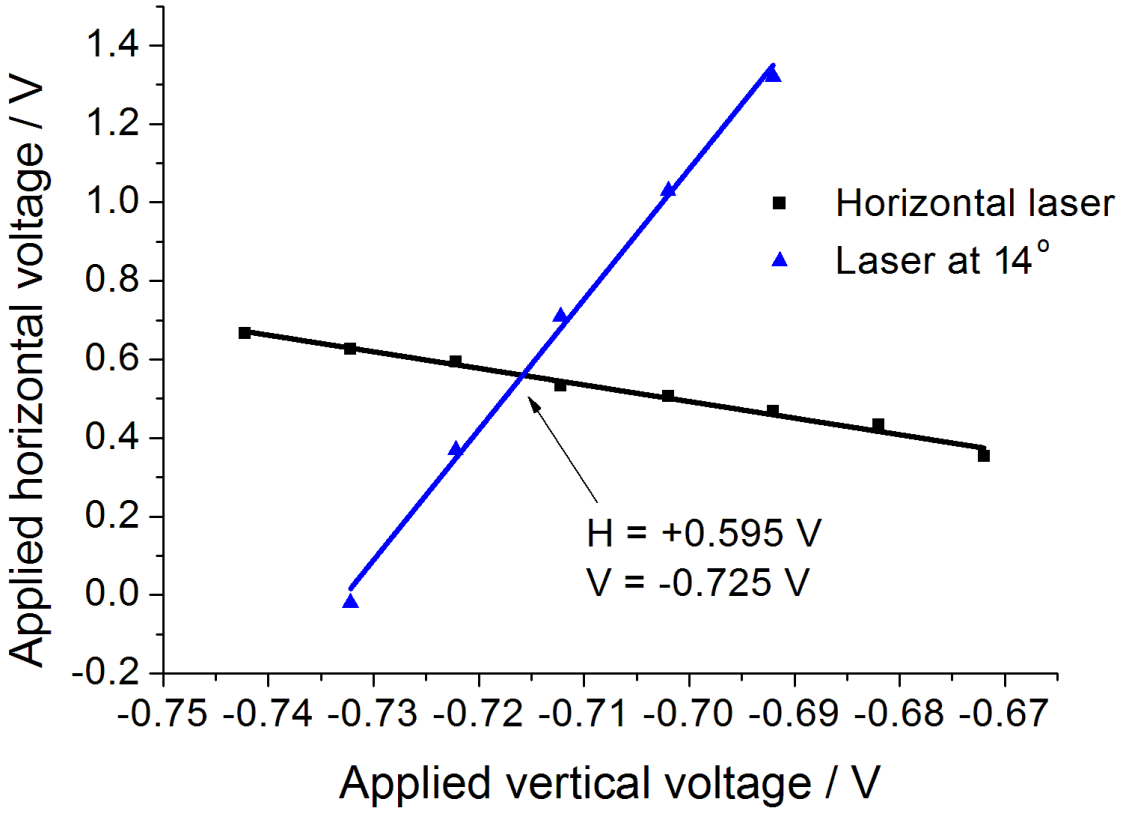

Figure 5.7: Locating the micromotion minimum in 2 dimensions by finding the point of intersection between the line of micromotion minima along two non-parallel lasers.

When the trap position was been adjusted in the radial direction by adjusting the RF electrode varcaps (sections 6.2.1 & 6.2.2), it was found that the correlation method no longer yielded a perfectly flat profile at the trap centre; similarly, when the amplitude inverted on passing through the trap centre, the phase difference in the sine wave was no longer π. This is attributed to a new unremovable micromotion component due to a phase mismatch between potentials on the four RF electrodes, and it renders the automated method described above unreliable. The minimum micromotion can still be found manually. It was found experimentally that locating the micromotion centre visually for the horizontal direction and manually finding the minimum micromotion in the vertical direc-

tion using the correlation method resulted in sufficiently low micromotion to cool the ion to close to the Doppler temperature so that it did not adversely impact the experimental results found in this work, and could be performed in a matter of minutes.

5.5 Compensating the Earth's magnetic field using the ground state Hanle effect

If a system with multiple magnetic sublevels is excited with by circularly polarised light, selection rules require that there is a corresponding change in the magnetic quantum number of the atom ($\Delta M = \pm 1$ for right or left circularly polarised light respectively.) As illustrated in figure 5.8, continually exciting an atom with one such polarisation will result in the entire population being pumped into a state from which no further excitation is possible, and fluorescence shall cease. This is known as optical pumping.

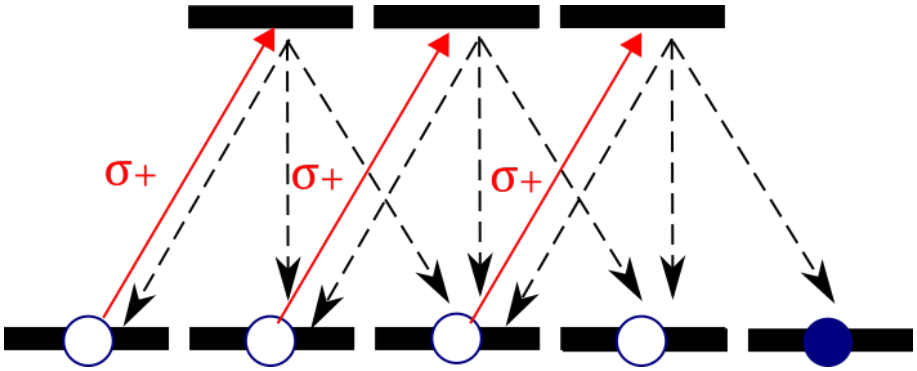

Figure 5.8: Optical pumping by a laser of pure $\sigma+$ polarisation. Once the ion reaches the state with the highest or second-highest angular momentum quantum number it can no longer be excited or decay to any other state, and so fluorescence ceases.

By rotating the measurement basis, we can see that for a general atomic manifold driven by an arbitrary fixed polarisation of light, if the magnetic sublevels of a given angular momentum state are completely degenerate, there exists a superposition of magnetic sublevels which will be a dark state for that given polarisation, and that the system will be driven into this dark state. If the magnetic sublevels are even slightly nondegenerate (due to the presence of a magnetic field for example), the different rate of phase-evolution of each state will result in the system leaving the dark-state superposition, and fluorescence resuming. This destabilisation of the dark state by a magnetic field is known as the ground-state Hanle effect [52, 53]. Note that if the dark state consists of a single level, it cannot be destabilised by a magnetic field as the phase of that level is the global phase of

the wavefunction. Pure polarisation states (σ_+,σ_- or π) will drive the system into such a state.

Linearly polarised light may be considered to have either π polarisation, $(\sigma_+ + \sigma_-)$ polarisation, or a combination of the two, depending on whether the polarisation vector is oriented parallel to or perpendicular with the B-field. If we use the pure π polarisation we can expect the system will be pumped into a dark state. Therefore we can null the magnetic field perpendicular to the polarisation of a linearly polarised laser by minimising the atomic fluorescence with respect to the applied magnetic field.

We implement this scheme on the $P_{\frac{1}{2}} \rightarrow D_{\frac{3}{2}}$ with an 866 nm laser acting as the repumper for $S_{\frac{1}{2}} \rightarrow P_{\frac{1}{2}}$ Doppler cooling. The polarisation is linearised in the y (horizontal along the trap and cavity axes) direction using a half- and quarter- waveplate. The magnetic field in z (vertical) and then x (horizontal perpendicular to the trap and cavity axes)) is scanned until minimum fluorescence is achieved in each direction (figures 5.9a and 5.9b). This implies that the repumper is now π polarised, and therefore the only magnetic field component is in the y direction. The repumper polarisation is then rotated by 90° so that it is perpendicular to the field in the y-direction, and the externally applied field amplitude is scanned until a minimum fluorescence is again achieved (figure 5.9c). At this setting, the field at the trap centre are nullified in all 3 dimensions, and the magnetic sublevels of the atom are degenerate. The count-rate has been reduced from 7 kcps to 1 kcps.

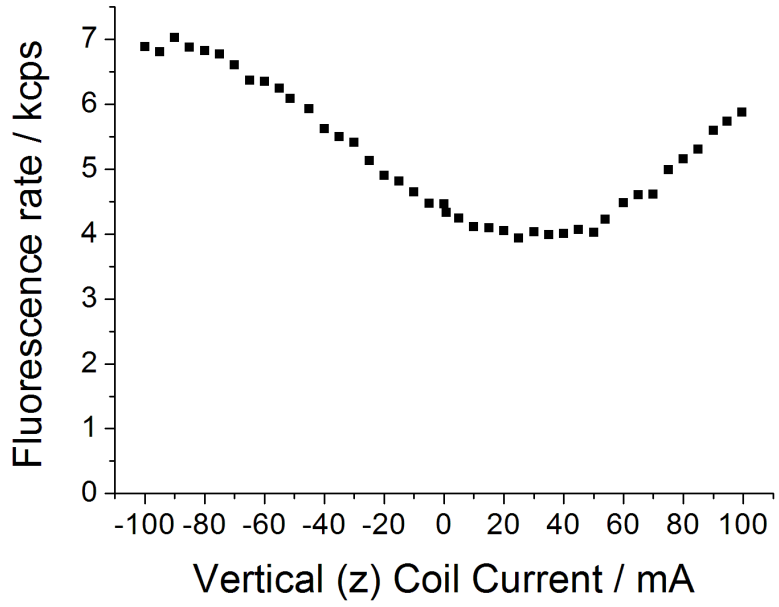

(a) Variation in atomic fluorescence with applied magnetic field in the vertical direction.

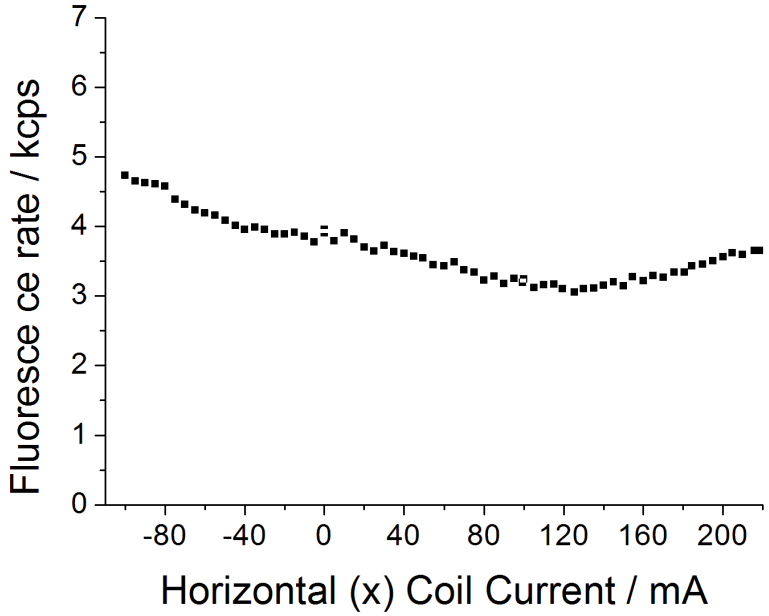

(b) Variation in atomic fluorescence with applied magnetic field in the vertical direction after minimising the stray field in the z direction.

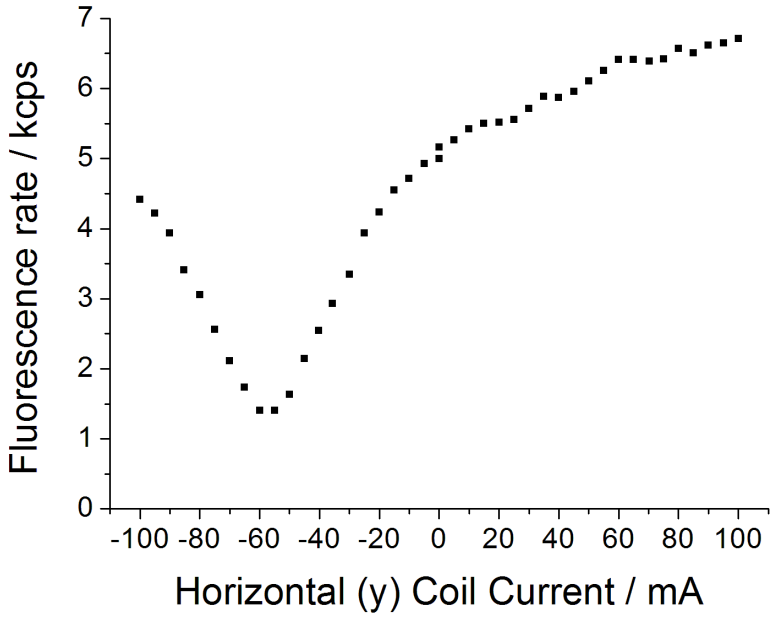

(c) Variation in atomic fluorescence with applied magnetic field in the y direction following nullification of the stray field in the $x - z$ plane.

Figure 5.9: Minimisation of the magnetic field at the trap centre using the ground state Hanle effect. Note that (c) features a sharper peak than (a) and (b) because minimising the field in the plane perpendicular to the y direction requires only compensation along one axis, while in the horizontal direction the field must be nullified in two steps.

The required currents to null the stray magnetic field at the trap centre are $I_x = 120$ mA, $I_y = -60$ mA, $I_z = 35$ mA. For most purposes, it is not necessary or desirable to have 0 magnetic field, which will severely curtail fluorescence and cooling. By applying no artificial field along any axis, we obtain a sufficient fluorescence rate for the work in this thesis with negligible field splitting. In the near future, these coils will be used in experiments in which the cavity will be detuned to match the splitting of a specific angular-momentum transition to generate photons of selected polarisation.

5.6 Spectroscopy of the 397 Transition

Spectroscopy is an essential tool of the atomic physicist, both in the identification of atomic resonance frequencies and in measuring the linewidth of a transition. The shape of the spectroscopic profile provides information on whether the ion is maximally cold (producing linewidth limited photons), the transition is being broadened by an excess of optical power, or if there is further structure due to the interaction of the angular momentum sublevels with a magnetic field (the Zeeman effect). Spectroscopy is the process of obtaining the emission spectrum for a given transition.

It is important for all experiments being carried out in this trap to assess that the ion is being cooled at close to the Doppler Temperature, and that we are cooling at an appropriate wavelength with an appropriate power. To this end, we perform spectroscopy on the cooling ($S_{\frac{1}{2}} \rightarrow P_{\frac{1}{2}}$) transition. Normally, spectroscopy is carried out by scanning a laser's frequency over the ionic resonance, and as such spectroscopy on cooling transitions has traditionally been limited due to the fact that once the cooling laser frequency reaches the blue side of the transition, the ion is no longer cooled but heated, and quickly leaves the trap. We make use of a novel technique fully described in [47] to measure both the red and blue parts of the atomic spectrum and to therefore obtain a conclusive measurement of the atomic linewidth.

In this technique we make use of the fact that it requires some time for the ion to heat up and become broadened, even when driving the ion on the blue side of resonance. We employ a short (5 μs) pulse of probe light to scan the frequency profile of the atom, while using a longer (15 μs) cooling pulse with a constant detuning to recool the ion and prevent it leaving the trap or becoming thermally broadened. These pulses are produced by feeding two VCOs into an RF switch's inputs, controlled by a pulse generator. The switch's output is then sent to the 397 nm laser's AOM. One VCO oscillates at a constant frequency, while the frequency of the other is scanned. An external program sets the probe

frequency, and measures the PMT signal during periods when the probe frequency is being applied to the ion.

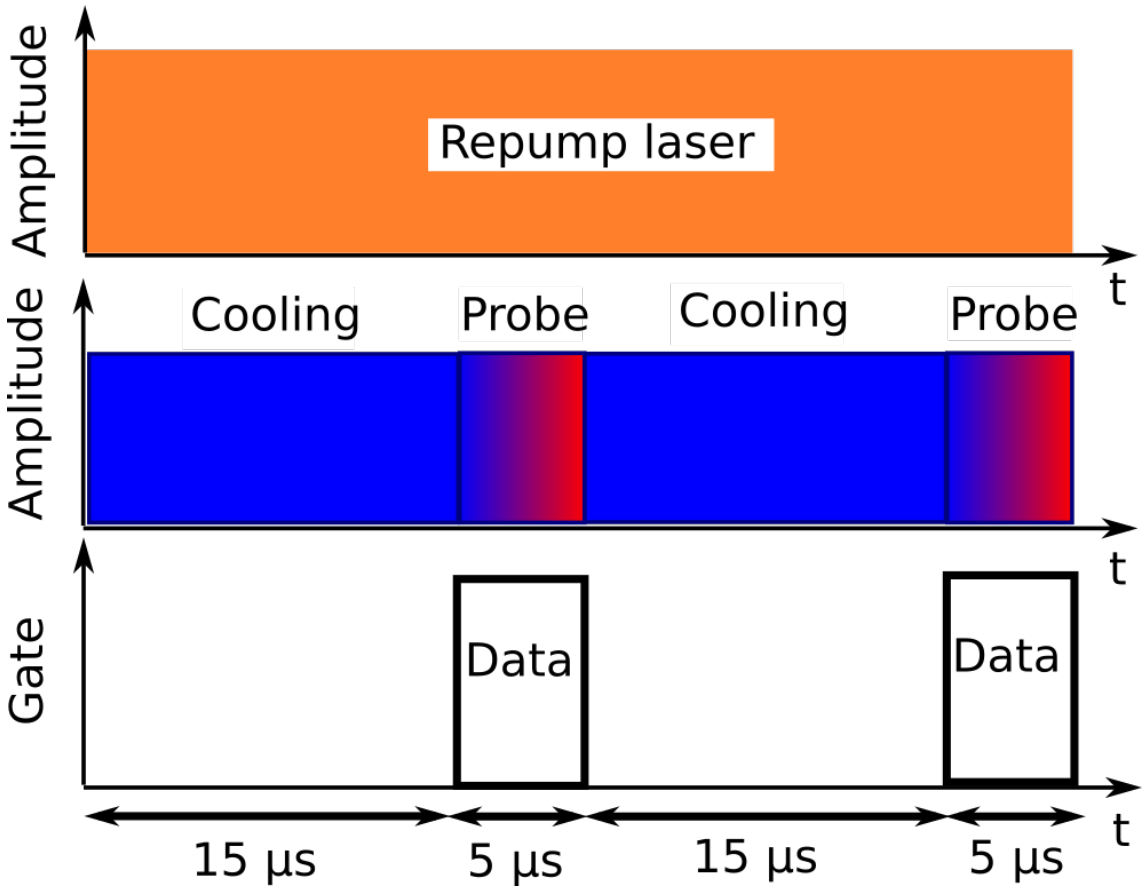

Figure 5.10: The pulse sequence used in full-profile spectroscopy. The atom is interrogated at the probe frequency for 5 μs, and then is cooled for 15 μs. Data is taken only during the 5 μs interrogation period. An optional recooling laser may be present if performing spectroscopy on an ion crystal which may melt due to background collisions and need to be recooled from a cloud. Not shown: repumping at 850 and 854 nm is constantly applied.

This presents a further challenge: as the frequency input of the AOM is varied, the output amplitude and laser-fibre coupling varies with it. Further control is required to maintain a constant laser intensity during the scan, which is essential to extract a meaningful count rate from the ion and to prevent power broadening at high intensities. The amplitude of the laser intensity as the frequency input is scanned with the amplitude input at its maximum value (1 V) is shown in figure 5.11a.

A calibration is carried out to measure the laser power versus amplitude output. This is used to identify the amplitude input value which gives a chosen laser output intensity. An example of this file and the laser power profile it results in are shown in figure 5.11b and 5.11c.

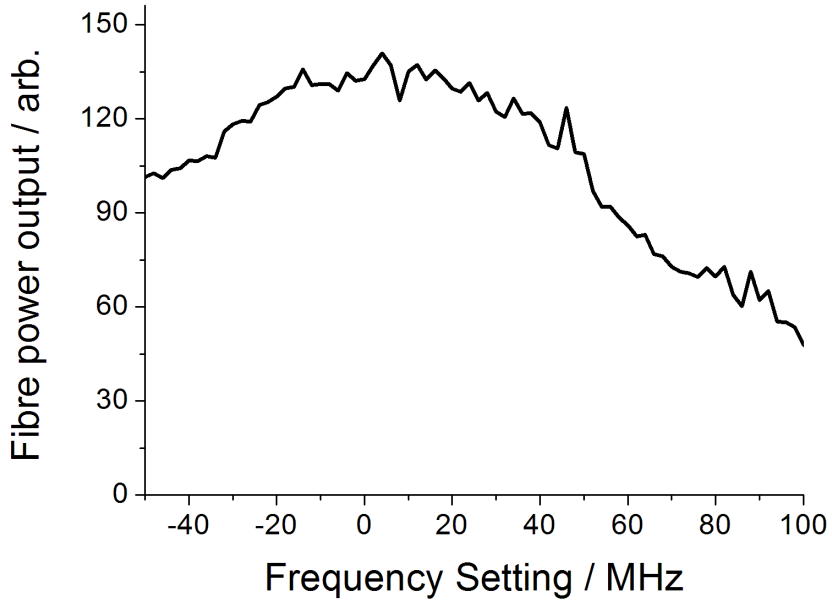

(a) The variation in the probe laser's fibre output power as the VCO's frequency input is scanned with the amplitude input held at a constant voltage.

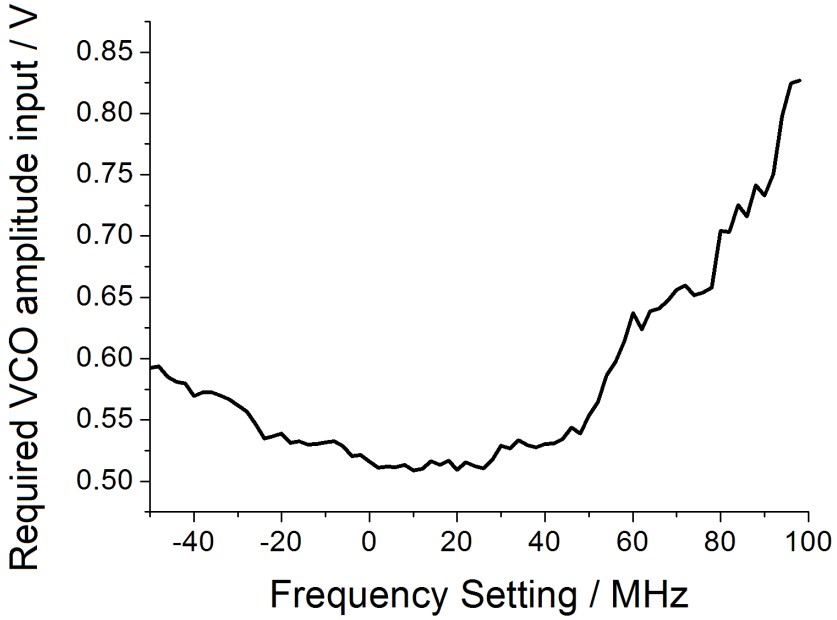

(b) The variation required in the VCO's amplitude input voltage to ensure the probe power remains constant as the frequency setting is scanned.

We must also ensure that the cooling laser power matches the probe laser power, so that we know that the spectrum of the ion we are probing is the one it has as we are cooling it, so we can set the cooling laser to the optimal cooling point and be sure we aren't power broadening it the rest of the time. This also avoids any kicks due to changes

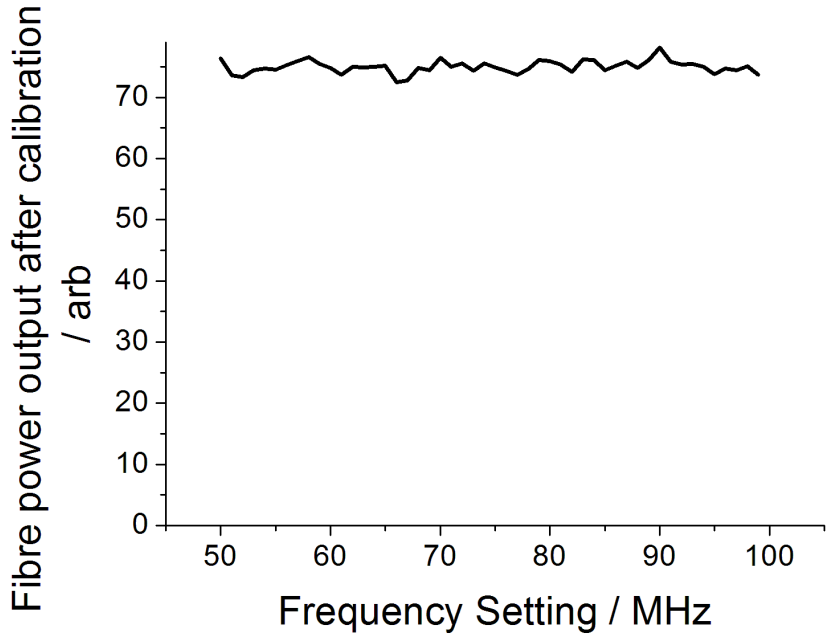

(c) The fibre output power as the laser is scanned after calibration. The variation in power is $< 2\%$.

Figure 5.11: Calibration of the VCO frequency and amplitude inputs to maintain a constant probe power during spectroscopy.

in light pressure as the spectroscopy changes from low intensity to high intensity. The output intensity of the laser may be viewed on a sufficiently fast photodiode so that the cooling power may be matched to the probe power.

The pulse sequence described above allows us to obtain spectra such as that shown in figure 5.12 showing the ion's linewidth, using a probe power of 1 μW which corresponds to an intensity of $1.98 \times 10^{-14}\,\mathrm{Wm}^{-2}$.

The frequency shift given on the y-axis is the offset of the probe laser from the cooling laser; it can be seen that in this instance the cooling laser is red-detuned by 12.5 MHz from linecentre, and the linewidth of the transition is measured at 23.3 MHz, in good agreement with the theoretical value of 21 MHz for $^{40}Ca^{+}$ convolved with the linewidth of our laser (~ 1.5 MHz). A Lorentzian provides a good fit, showing that there is no significant thermal broadening component, which would be expressed as a Gaussian contribution to the width, giving it an overall Voigt profile. Similarly, we can see that the ion is not power broadened. It is therefore possible to identify the cooling transition resonance frequency as being 12.5 MHz blue of the cooling laser, at a wavelength of 396.95895 nm.

Spectroscopy is always performed on the ion to confirm it is stable and well cooled before performing any experiment.

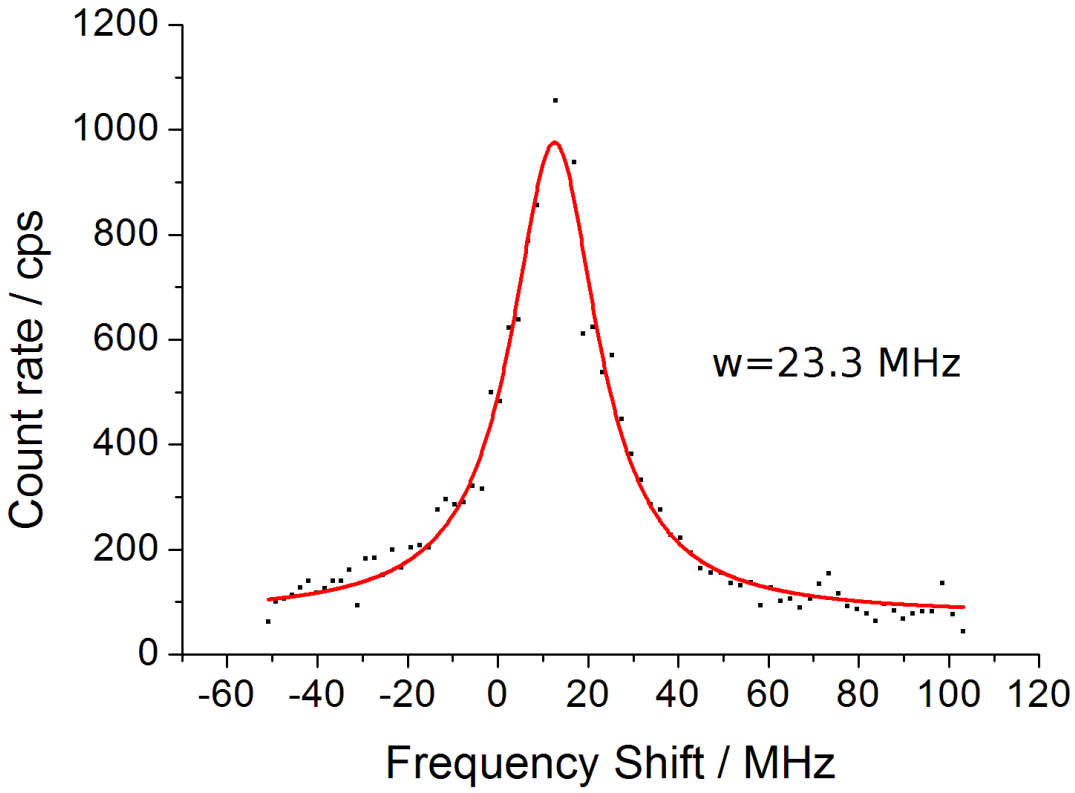

Figure 5.12: Spectroscopy of single ionised $^{40}Ca^{+}$.

5.6.1 Dark Resonance Spectroscopy and identification of the 866 nm frequency

In this section we take advantage of the $S_{\frac{1}{2}} \rightarrow D_{\frac{3}{2}}$ dark resonance to determine the linecentre of the $P_{\frac{1}{2}} \rightarrow D_{\frac{3}{2}}$ transition and hence the zero-detuning wavelength of the experimental photons. A dark resonance occurs when two lasers couple two atomic levels in Raman resonance. This leads to a coherent dark state, in which even though the lasers couple the two ground states to an excited state, the excited state is never populated. The population is therefore transferred between the ground state of each laser transition without involving a decay from the excited state. This results in a vanishing fluorescence. Driving $^{40}Ca^{+}$ with 397 nm light and 866 nm light simultaneously can cause an $S_{\frac{1}{2}} \leftrightarrow D_{\frac{3}{2}}$ dark state without populating the $P_{\frac{1}{2}}$ level.

The population of the $P_{\frac{1}{2}}$ state is dependent on the Rabi frequencies and detunings of the 397 nm cooling laser and 866 nm repumping laser in the following way [55]:

$$N_p = \frac{4(\delta_C - \delta_R)^2 \Omega_C^2 \Omega_R^2 \cdot (\Gamma_C \Gamma_R)}{Z}, \tag{5.9}$$

where N_p is the $P_{\frac{1}{2}}$ state population, Ω_C and Ω_R are the cooling and repump Rabi frequencies respectively, δ_C and δ_R are the cooling and repump detunings, Γ_C and Γ_R are

the decay rates to the $S_{\frac{1}{2}}$ and $D_{\frac{3}{2}}$ states, and Z is given by

$$\begin{aligned} Z =& 8(\delta_C - \delta_R)^2\Omega_C^2\Omega_R^2(\Gamma_c + \Gamma_R) + 4(\delta_C\delta_R)^2(\Gamma_c + \Gamma_R)^2(\Omega_C^2\Gamma_R + \Omega_R^2\Gamma_C) \\ &+ 16(\delta_C - \delta_R)^2[\delta_C^2\Omega_R^2\Gamma_C + \delta_R^2\Omega_C^2\Gamma_R]) \\ &- 8\delta_C(\delta_C - \delta_R)\Omega_R^4\Gamma_C + 8\delta_R(\delta_C - \delta_R)\Omega_C^4\Gamma_R \\ &+ (\Omega_C^2 + \Omega_R^2)^2(\Omega_C^2\Gamma_R + \Omega_R^2\Gamma_C). \end{aligned}$$

It is clear from equation (5.9) that when $\delta_C = \delta_R$, the population of the $P_{\frac{1}{2}}$ state drops to 0, and therefore so does the 397 nm fluorescence.

To observe this, we perform spectroscopy as described in section 5.6 while also illuminating the ion with 866 nm light. We use high power (120 μW) cooling beam, with an intensity of $2.38 \times 10^{-12}\,\mathrm{Wm}^{-2}$, and a relatively high detuning of 50 MHz to give a broad spectral profile so that the dark resonance may be more easily located. The 866 nm laser power is 128 μW, or intensity $1.58 \times 10^{-12}\,\mathrm{Wm}^{-2}$. A dip in the spectrum is observed where the probe photons have the same detuning from the $S_{\frac{1}{2}} \rightarrow P_{\frac{1}{2}}$ transition as the 866 nm photons have from the $P_{\frac{1}{2}} \rightarrow D_{\frac{3}{2}}$ transition. This can be seen in figure 5.13a. By aligning the dark resonance dip with the peak of the cooling transition spectroscopy as in figure 5.13b, we can identify the $P_{\frac{1}{2}} \rightarrow D_{\frac{3}{2}}$ resonant wavelength as 866.45092 nm.

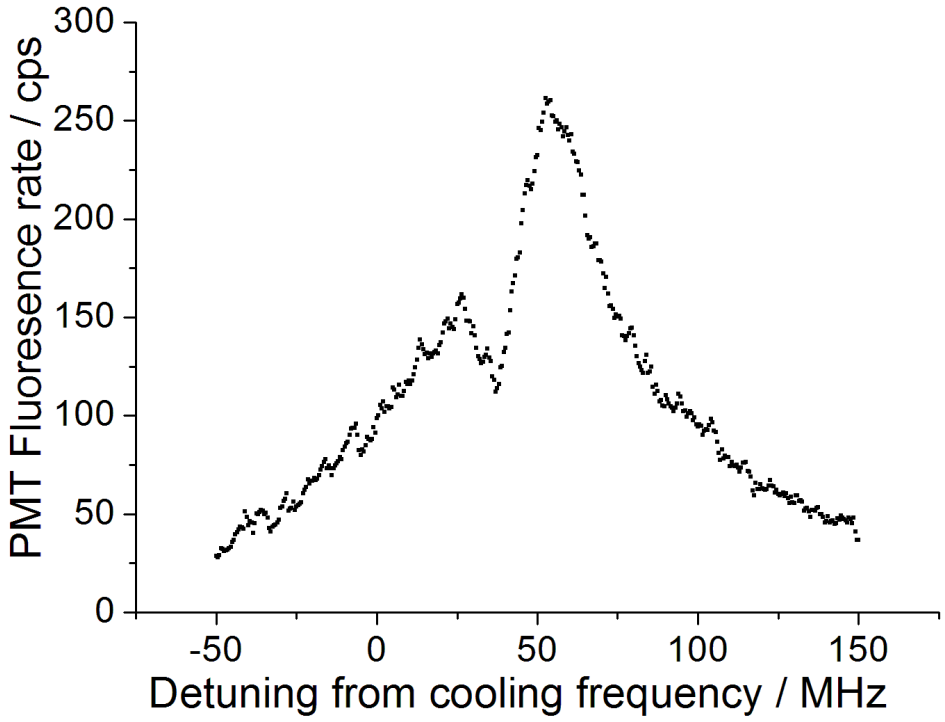

(a) Dark resonance dip visible on the red side of the $^{40}Ca^{+}P_{\frac{1}{2}} \rightarrow S_{\frac{1}{2}}$ resonance.

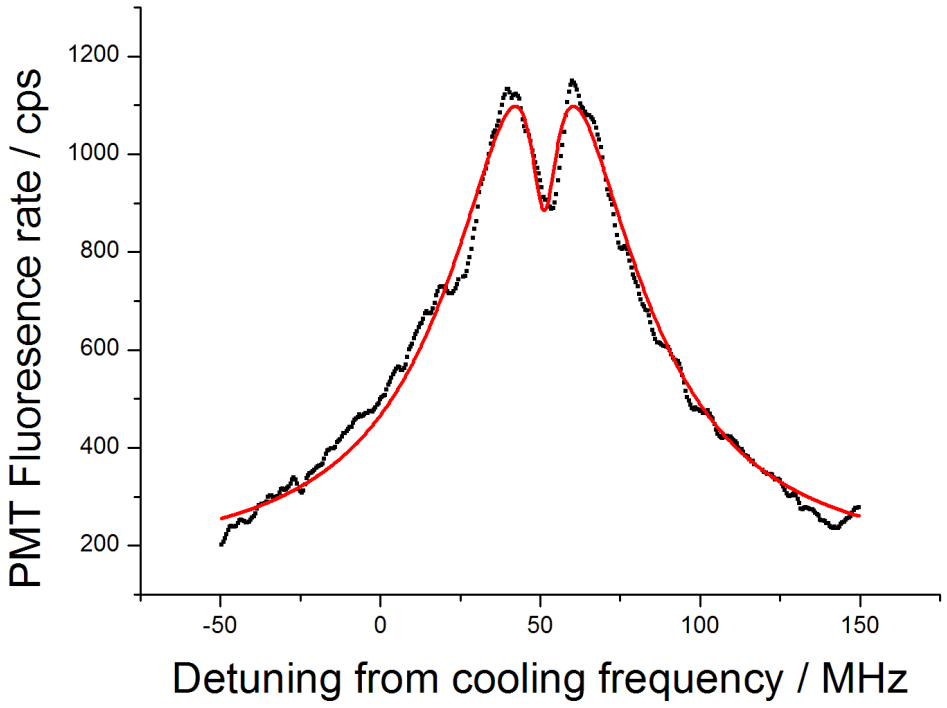

(b) Dark resonance overlapped with the $^{40}Ca^{+}P_{\frac{1}{2}} \rightarrow S_{\frac{1}{2}}$ resonance by bringing the repumper frequency into resonance with the $^{40}Ca^{+}P_{\frac{1}{2}} \rightarrow D_{\frac{3}{2}}$ resonance.

Figure 5.13: Identification of the $^{40}Ca^{+}P_{\frac{1}{2}} \rightarrow D_{\frac{3}{2}}$ transition wavelength using dark resonance spectroscopy.

Chapter 6

Optimisation of ion-cavity coupling and single photon emission

In this chapter, we bring together the ion and cavity systems described so far in this work to form a cQED system which can deterministically couple multiple ions to the cavity mode with optimal efficiency.

6.1 Raman spectroscopy

For cQED experiments, it is important that we can stabilise the cavity's length to be resonant with the atomic emission. The resonance frequency of the cavity is defined by its length. As such, by varying the cavity length while it is close to resonance with a coupled ion, we may observe a Lorentzian resonance like that observed in section 5.6. Alternatively, the cavity length may remain fixed and the frequency of the laser driving the ion may be scanned such that a cavity resonance is observed when the detuning of the laser from the atomic resonance matches the detuning of the cavity from the resonance. As our driving laser is also the cooling laser, we will adopt the former approach.

Following the identification of the correct FSR to lock the cavity to (see section 4.5), we lock the cavity to one of the tunable sidebands introduced by the fibre EOM. As these sidebands may be tuned by adjusting the frequency supplied to the EOM, the cavity length may be changed, as the locking circuit will feed back to the cavity piezo to keep the system on resonance. A single ion well coupled to the cavity exhibits a cavity emission profile like that in figure 6.1 as the cavity length is scanned over resonance.

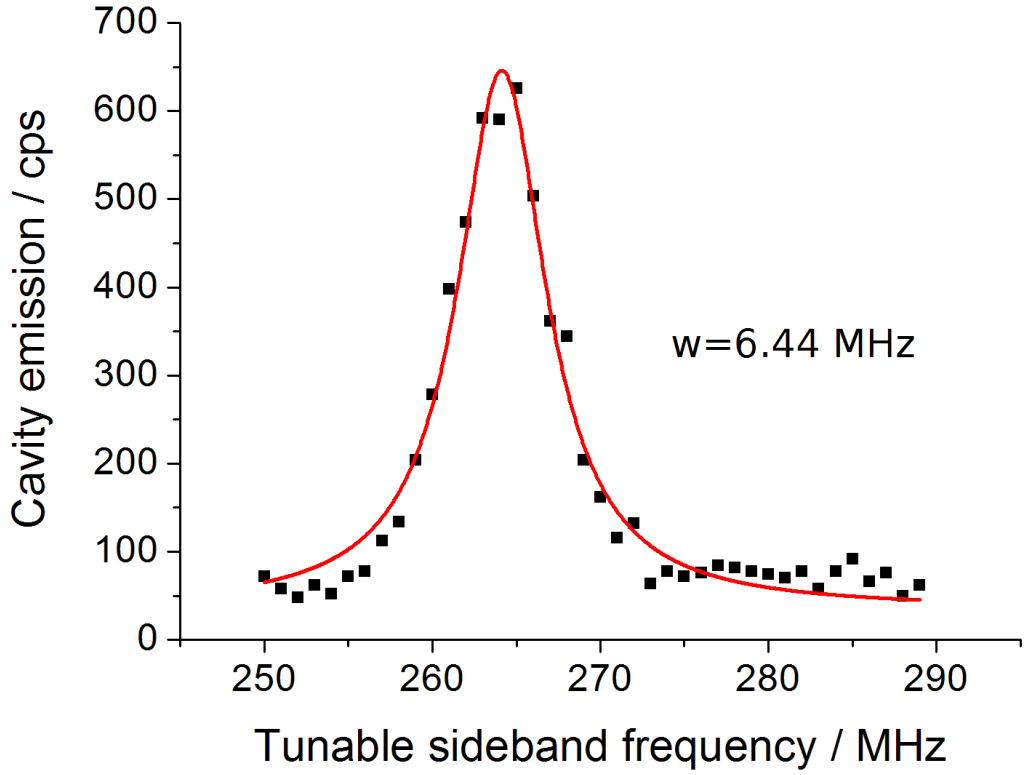

Figure 6.1: Cavity fluorescence rate as the cavity length is scanned over resonance.

This scan allows us to accurately fix the cavity length on resonance with the atomic transition. It also provides an absolute frequency reference for the cooling laser - as the tunable sideband frequency is relative to the Cs reference, locking to the sideband at a given frequency will repeatably yield the same cavity length. By placing an ion in the trap and tuning the cooling laser so that the cavity emission rate is maximised for a given sideband frequency, we can repeatably select the same cooling detuning over subsequent iterations of the experiment.

6.2 Ion-cavity overlap

The cavity emission is strongly dependent on the coherent coupling g, and thus it is crucial that g be optimised. g is position dependent and proportional to the cavity mode distribution function. As the TEM_{00} mode is radially symmetric, the ion's position must be optimised radially and axially. The radial mode shape is Gaussian with a 36 μm waist. The axial field varies sinusoidally with a period of that of the wavelength of the light; the distance between a field node and antinode is 216.5 nm. Radial coupling will be discussed in section 6.2.2, and axial coupling of a single ion and then ion strings will be discussed in 6.2.4.

6.2.1 Radial overlap using cavity-mode repumping

As described in section 3.2.1, four variable capacitors are included in series between the trap's resonance transformer and the RF electrodes. As the position of the cavity is fixed with respect to the trap hardware, to optimise the radial coupling of the ions to the trap we must move the trap centre. This can be achieved by adjusting the capacitance of each varcap to maximise coupling between the ion and the trap. Increasing or decreasing the capacitance of one varcap will move the trap centre diagonally with respect to the horizontal and vertical axes.

This process begins with a visual observation of the overlap of the trap and cavity mode using the CCD focussed at the trap region. The trap centre may be sufficiently off-axis that little or no coupling of light from the atoms into the cavity will be observed. The cavity is locked to a low level of 866 nm light, which is used as a repumper for a large ion crystal.

Section 5.6.1 detailed the dark resonance effect which causes a drop in UV fluorescence when the cooling and repumper detunings are equal, and equation (2.45) described linewidth broadening due to a high driving intensity. At sufficiently high repumper powers, power broadening of the repumper transition causes broadening of the two-photon dark resonance to the degree that it overlaps the cooling resonance. At the minimum level of 866 nm light required to lock the cavity to the TEM_{00} mode, the fluorescence of the crystal begins to increase toward the trap centre as the ions see a greater repumper intensity, and then drops dramatically as the $4S_{\frac{1}{2}} \rightarrow 3D_{\frac{3}{2}}$ dark resonance becomes driven due to the high 866 nm laser powers at the centre of the mode. However, the TEM_{00} mode does not offer a high enough spatial resolution and it is not possible to lock the cavity with 866 nm laser power at a low enough level to see any fluorescence at all from a crystal close to the cavity centre. We therefore use the TEM_{20} mode, which has a more complex structure and allows us to more accurately position the ion crystal at the trap centre, as illustrated in Figure 6.2.

Fluorescence from the crystal is observed on the CCD and its position with respect to the cavity centre determined. We begin with all varcaps fully closed with a layer of Kapton preventing them from short-circuiting. Two varcaps can then be slowly opened to move the crystal in the correct direction horizontally, while moving it in opposite directions vertically. The trap drive frequency, position of the cooling beam, and micromotion minimisation (section 5.4) voltages must be regularly adjusted in order to ensure the ions remain stably trapped. This process allows the trap centre to be moved to overlap with

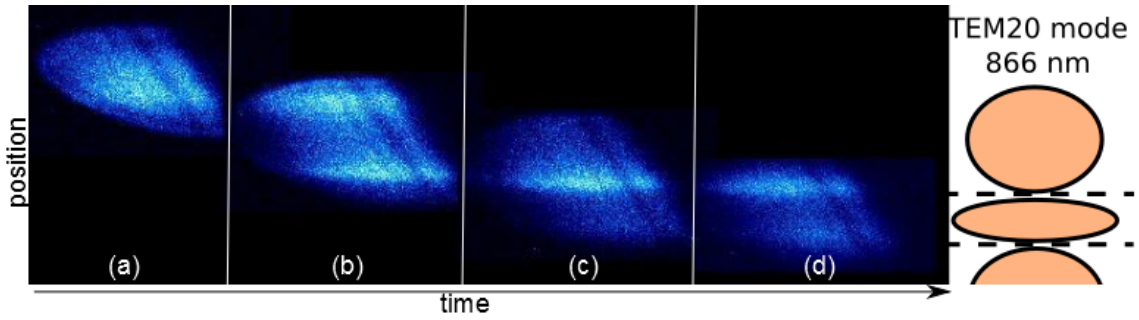

Figure 6.2: Overlapping the trap and cavity axes using the UV fluorescence observed on the CCD. The dark areas in the figure are areas of high 866 nm power, where the $4S_{\frac{1}{2}} \rightarrow 3D_{\frac{3}{2}}$ resonance is being driven. The lighter areas are the nodes of the radial mode shape or regions at the edge of the mode where the power is lower.

the cavity mode centre in the horizontal plane, but it is less certain how well positioned the crystal is vertically. We take it in turns adjusting the variable capacitors of the two adjacent electrodes to ensure we displace the crystal minimally in the vertical direction while moving it in the horizontal direction.

Figure 6.2 presents a series of images of a large ion crystal as it is moved through the 866 nm TEM_{20} mode, while being repumped only by the cavity mode. In (a), the crystal is repumped by the outer side of the outer antinode of the TEM_{20} mode, and fluorescence begins to drop in the lower part of the image due to dark resonance effects. In (b), the crystal is roughly centred (in the focal plane) on the outer antinode - two bright bands can be seen where lower intensity light effectively repumps the transition, while at the maximum 866 nm light intensity at the centre of the crystal there is low fluorescence. In (c), the crystal is now centred on the node between the outer and inner antinodes, and we see a maximum of fluorescence at the crystal centre where the repumper intensity is weakest. Finally in (d) the crystal has been centred around the central antinode of the TEM_{20} mode in the focal plane. Fluorescence is low from the entire crystal as the repumper intensity is highest here, but we see an increase in crystal fluorescence toward the nodal regions to either side as the repumper intensity drops. The cartoon on the right illustrates the shape and position of the TEM_{20} mode observed here, with the mode shown in orange and the nodal lines drawn as dashed lines.

Once the crystal has been roughly aligned with the centre of the mode, fluorescence into the cavity mode from a crystal may be used to further optimise the ion-cavity overlap in the radial plane.

6.2.2 Radial overlap using cavity emission

The cavity can now be locked to the 894 nm TEM_{70} mode co-resonant with the 866 nm TEM_{00} mode. Raman spectroscopy (section 6.1) can be performed to locate the cavity length which yields the fluorescence maximum. Ion-cavity coupling may now be optimised by maximising the fluorescence rate observed by the cavity-output APD. Extreme care in minimising the micromotion must be taken before making any reading, as small increases in micromotion resulting from the shift in the trap position dramatically affect the linewidth and hence cavity emission rate. By scanning the ion position the fluorescence maximum can be found independently along the directions of the orthogonal electrodes (at 45° to the horizontal and vertical axes.)

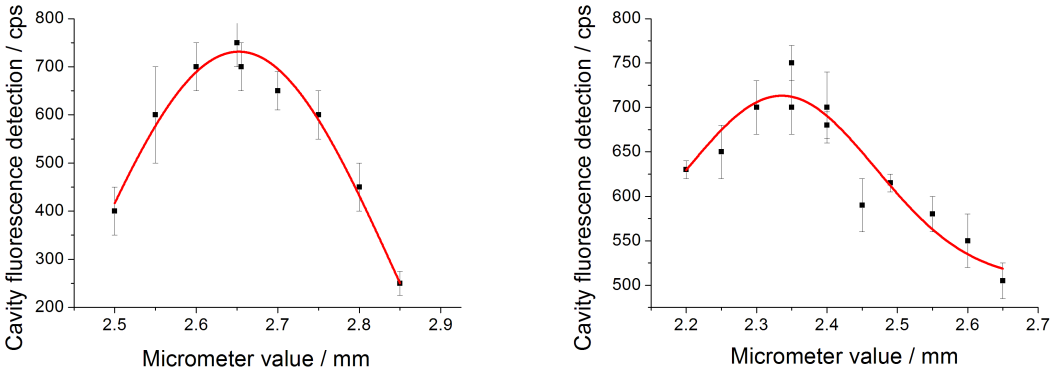

(a) Variation in cavity output as varcap #3 is adjusted.

(b) Variation in cavity output as varcap #2 is adjusted.

Figure 6.3: Optimisation of the ion-cavity overlap using cavity emission from a single ion.

Figures 6.3a and 6.3b show the variation in cavity emission as two varcaps are opened and closed. The x-values are the micrometer scale units at which the datapoints were read. We see that the ion-cavity coupling is optimised in the radial direction when these capacitors are set to 2.65 mm and 2.34 mm.

6.2.3 Axial coupling of a single ion

The cavity field varies axially on much shorter lengthscales ($\sim$ 200 nm) than radially ($\sim$ 36 μm). In order to maximise the ion-cavity coupling, the ion must be localised to within half a wavelength (the *Lamb-Dicke* regime,) and positioned at an antinode of the cavity field. The colder the ion, the less it will deviate from the antinodal position and the higher the average coupling will be. While optimal radial coupling was achieved by translating the ion relative to the radially fixed cavity, axial coupling may be optimised by

translating the cavity with respect to the ion. The ion may be translated by adjusting the endcap potentials, but as this will also change the axial confinement, which will change not only the spatial confinement of the ion but the inter-ion separation in ion strings, it is significantly simpler to optimise the axial coupling by translating the cavity.

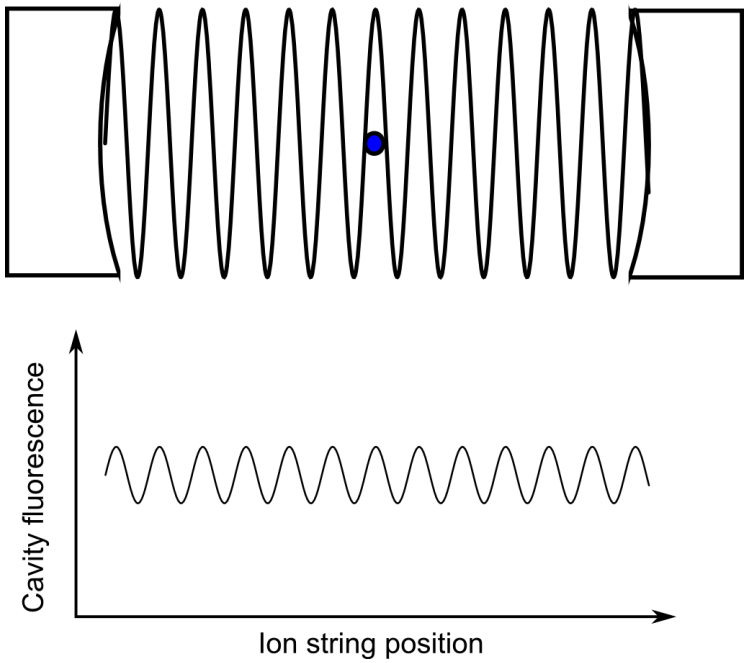

Figure 6.4: Cavity emission expected as a single ion is moved axially along the cavity.

The spatial distribution of a single ion in the harmonic axial potential can be described by a Gaussian distribution $< x >$, while the intensity of the cavity field I is simply proportional to the square of a sinusoid:

$$\text{defining } b = \sqrt{\frac{2k_B T}{m_{\mathrm{Ca}}\omega_{sec}^2}}, \tag{6.1}$$

$$< x > \propto e^{-\frac{x^2}{b^2}}, \tag{6.2}$$

$$I \propto \cos\left[\frac{2\pi(x)}{\lambda}\right]^2. \tag{6.3}$$

m_{Ca} is the mass of ^{40}Ca, ω_{sec} is the axial secular frequency, T is the temperature, λ is the wavelength of the cavity resonance and x is position in space.The cavity output fluorescence rate and hence g^2 is proportional to the convolution of the ion's position and the cavity field intensity:

$$g^2 \propto \int_{-\infty}^{+\infty} e^{-\frac{x^2}{b^2}} \cdot \cos^2\left[\frac{2\pi(x - x_0)}{\lambda}\right]. \tag{6.4}$$

where x_0 simply defines the position of the centre of the cavity relative to the ion. Using

$$\cos^2(k \cdot x + kx_0) = \frac{1}{2}\left[1 - \sin(2k \cdot x - 2k \cdot x_0)\right], \tag{6.5}$$

and letting $k = 2\pi/\lambda$ (6.4) becomes

$$g^2 \propto \int_{-\infty}^{+\infty} e^{-\frac{x^2}{b^2}} \cdot \frac{1}{2}\left[1 - \sin\left(2k \cdot x - 2k \cdot x_0\right)\right]. \tag{6.6}$$

The first term evaluates via a standard integral as

$$\frac{1}{2}\int_{-\infty}^{+\infty} e^{-\frac{x^2}{b^2}} dx = \frac{\sqrt{\pi}}{4b}, \tag{6.7}$$

a constant, giving a constant background to the cavity emission as the cavity is moved relative to the ion. The second term may be evaluated as:

$$\frac{1}{2}\int_{-\infty}^{+\infty} e^{-\frac{x^2}{b^2}} \cdot \frac{1}{2}\left[\sin\left(2k \cdot x - 2k \cdot x_0\right)\right] = \frac{1}{2}\mathrm{Re}\left\{\int_{-\infty}^{+\infty} e^{-\frac{x^2}{b^2}} \cdot e^{2ik(x-x_0)} dx\right\} \tag{6.8}$$

$$= \frac{1}{2}\mathrm{Re}\left\{\int_{-\infty}^{+\infty} e^{-\frac{x^2}{b^2}+2ik(x-x_0)} dx\right\} \tag{6.9}$$

$$= \frac{1}{2}\mathrm{Re}\left\{\int_{-\infty}^{+\infty} e^{-b^2\cdot k^2-2ikx_0} \cdot e^{\left[\frac{ix}{b}+\sqrt{2ik(x-x_0)}\right]^2} dx\right\}. \tag{6.10}$$

As the inside of the integral in (6.10) has no poles, the imaginary part does not contribute to the solution and the integral simplifies to

$$\frac{1}{2}e^{-b^2\cdot k^2-2ikx_0}\int_{-\infty}^{+\infty} e^{\left[\frac{-x^2}{b^2}\right]} dx \tag{6.11}$$

$$= \frac{\sqrt{\pi}e^{-b^2\cdot k^2}}{4b}\sin(2kx_0). \tag{6.12}$$

this term is an oscillation in x_0, the offset of the ion and cavity field positions. We can therefore state

$$g^2 \propto \frac{\sqrt{\pi}}{4b}[1 + e^{-b^2\cdot k^2}\sin(2kx_0)]. \tag{6.13}$$

The visibility, defined as the ratio of the amplitude of the oscillatory part of the signal to the constant part of the signal is given by

$$\mathrm{Vis} = \frac{\text{amplitude}}{\text{offset}} = \frac{\sqrt{\pi}e^{-b^2\cdot k^2}}{4b} \cdot \frac{4b}{\sqrt{\pi}} = e^{-b^2\cdot k^2} \tag{6.14}$$

$$= e^{\frac{8\pi^2 k_b T}{\lambda^2 m_{\mathrm{Ca}}\omega_{sec}^2}}. \tag{6.15}$$

A schematic of a single ion in a cavity and the cavity emission as it is translated relative to the ion is shown in figure 6.4. The output from the cavity while scanning its position relative to the ion over $\sim 1\mu$m is shown in figure 6.5b. The endcaps are held at 650 V to provide the highest confinement, yielding an axial secular frequency of 620 kHz.

The coupling of the TEM_{00} mode to the optical fibre 30 cm away is not constant over the full scanning range; therefore a calibration is taken using the emission of a large, warm

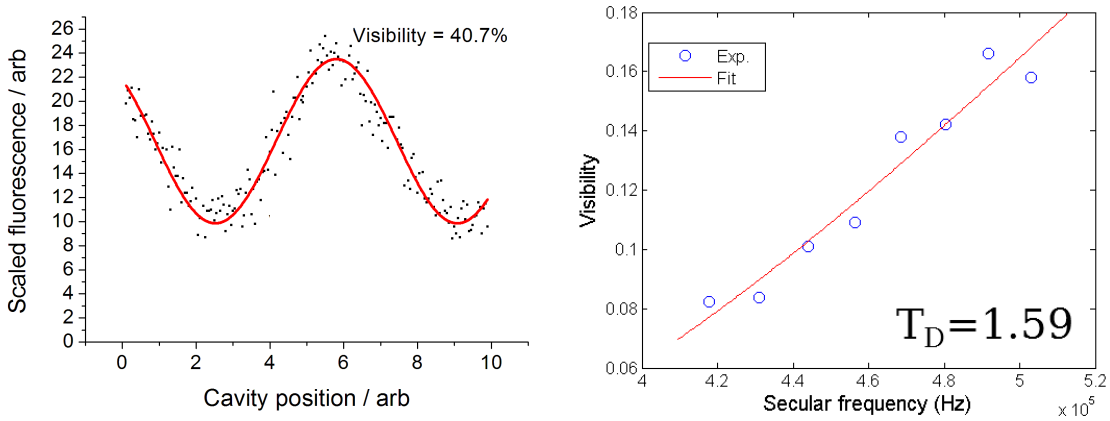

(a) Cavity fluorescence as the position of the cavity is scanned relative to the ion. A visibility of 40.7% is observed, indicating a temperature of $< 1.1 T_D$.

(b) The variation of single-ion visibility over the range of parameters that will be used to investigate the couplings of longer ion strings.The ion's temperature can be extracted from this fit as $1.59\,T_D$.

Figure 6.5: The visibility of a single ion a) at the highest achievable axial confinement in our trap and b) over the range of confinements that will be investigated for the coupling of multiple ions. The error bars are smaller than the data points.

crystal to normalise the collected emission rate. This is why the y-axis scale is expressed as an arbitrary ratio. A background calibration is also taken to remove the varying signal from the 894 nm TEM_{70} locking mode.

The ion temperature may be extracted from the data shown in figure 6.5b using equation (6.15) as a fitting function. Cooling with a 23 MHz linewidth, we obtain a Doppler temperature $T_D = \frac{\hbar\Gamma}{2k_B} = 552\,\mu\mathrm{K}$. An observed visibility of 41%, determines that the ion's temperature is $< 1.1 T_D$. The spread of the ion's wavefunction can be determined from the visibility as $\sigma_x = \sqrt{< x^2 >} = b^2 = \sqrt{-\frac{\lambda^2}{8\pi^2}\ln[\mathrm{Vis}]} = 163\,\mathrm{nm}$ [56].

6.2.4 Axial coupling of multiple ions

In order to generate large-scale entangled states in the trap, the coupling of multiple ions to the cavity must be simultaneously optimised. It is not sufficient to simply translate the cavity around the ions, the ion spacing must be varied to ensure that all ions can be simultaneously located at antinodes in order to achieve the highest coupling. As the node-node distance in the cavity cannot be changed without changing the resonant frequency, the ion-ion spacing must be changed by varying the endcap potentials. This can be characterised by the axial secular frequency of the trap. We have seen that the ion's visibility varies as the exponential of the inverse square of the secular frequency. The

range of confinements to be used in these experiments has been selected to be one over which strings of up to 5 ions show good coupling to the cavity. The visibility of a single ion across this range of secular frequencies is shown in figure 6.5b.

In order to trap longer chains of ions in the trap stably, we must apply an additional off-resonance laser that may recool the ions if they become an excited cloud by the result of, for example, a background collision. A laser detuned 150 MHz from resonance with a power of 2.1 μW helps maintain the stable ion string. For consistency of measurement, this additional laser is present during the measurement of 6.5b, which contributes to the ion's higher temperature.

The visibility of longer ion chains will vary dependent on the degree of overlap of the ions with cavity antinodes, the secular frequency, and the ions' temperature. Note that for ion strings, the centre-of-mass motional mode does not solely define the spread of the atomic wavefunction; higher order modes will contribute higher secular frequency components with greater confinements. The total spread is given by a weighted quadrature sum of the spreads of all contributing modes. Therefore it is possible to achieve a higher degree of ion-localisation and ion-cavity coupling for a longer ion string than for a shorter string or single ion. A numerical simulation of the cavity coupling with varying ion position and confinement that takes these effects into account is used to fit the data.

The cavity emission during a visibility measurement involving multiple ions will always take the form of a sinusoid with a constant offset, as the sum of two sinusoids with the same frequency is always another sinusoid with the same frequency. The amplitude of this sinusoid is given by the difference between the optimal and pessimal couplings of the ion chain to the cavity mode. It is greatest when all ions are spaced by an integer multiple of half wavelengths, so that they may all sit simultaneously at a node or an antinode, and least when the ions are spaced such that translating the cavity does not change the output fluorescence. The situations are illustrated in figures 6.6a and 6.6b.

This allows a plot of visibility against secular frequency to be produced so that the confinements permitting the highest axial couplings may be identified. The variation in ion visibility with confinement for 2 and 3 ions are shown in figures 6.7a and 6.7b respectively.

We can observe in the case of 2 ions that the variation in visibility repeats as the spacing between the ions varies between $n \times 433\,\text{nm}$ and $(n+1) \times 433\,\text{nm}$. This variation is modulated by an envelope that comes from the changing spatial distribution of the individual ions. For 3 ions, the pattern is more complex, with a large peak when the spacing between the ions is equal to $n \times 433\,\text{nm}$ and a small peak when the spacing is

$(n + \frac{1}{2}) \times 433\,\text{nm}$, where the two outer ions may be optimally coupled to cavity antinodes while the central ion is located at a node.

For strings of 2 and 3 ions, the axial confinement and ion-cavity relative position allow precise overlap of each ion with a cavity antinode. For longer ion strings, the spacing between ions is not equal so it is not guaranteed that a confinement and position may be found where all ions are coupled to the cavity equally. Fortunately, as the node-node distance of 433 nm is much shorter than the typical ion-ion separation of $\sim 8\,\mu$m at 500 kHz axial secular frequency, it is still possible within the range of accessible confinements to find spacings between each pair of ions that are an integer n multiple of half wavelengths,

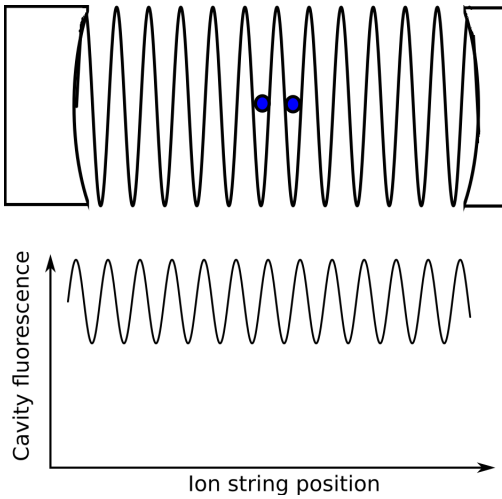

(a) Two ions optimally confined for cavity coupling. The ions are separated by an integer number of half wavelengths.

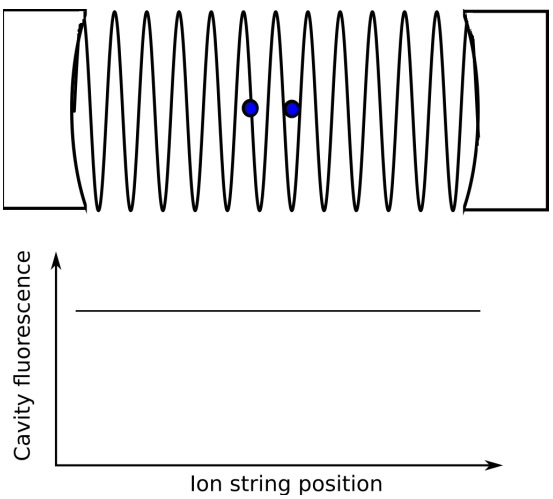

(b) Two ions pessimally confined for cavity coupling. The ions are separated by a half-integer number of half wavelengths.

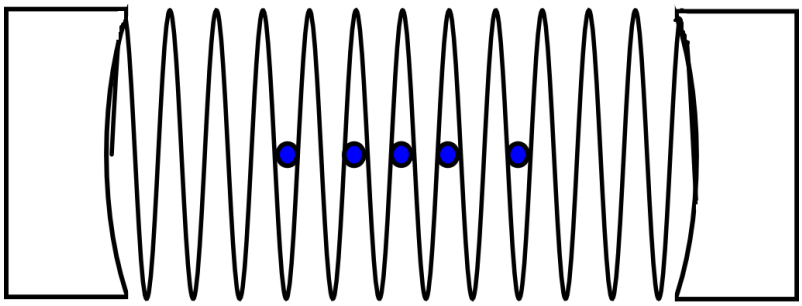

(c) Optimal coupling of longer chains of ions relies on each ion being positioned close to a cavity antinode, however the distances between ions will not be equal. As the ion-ion distance is $O(8\,\mu\text{m})$ at the secular frequencies used while the node-node distance is only 433 nm, appropriate confinements can be found that will optimise the coupling of many ions in a string simultaneously.

Figure 6.6: Schematic of the coupling of multiple ions to the cavity mode.

even if n is different for different pairs of ions. This is shown schematically in figure 6.6c. The variation of the cavity florescence visibility with 4 and 5 ions is shown in figures 6.7c and 6.7d.

These plots demonstrate that despite a more complex variation in g with axial confinement, it is still possible to couple multiple ions to the cavity mode simultaneously with a greater degree of coupling than a single ion at the same confinement, with visibilities of up to 40% achieved for 3, 4, and 5 ions despite the greatest visibility observed for a single ion in this range being only 16.9%. The predictive power of the simulation has been demonstrated, and should generalise to optimally coupling even larger strings to the cavity mode. The resolution of the DC confinement voltage source is $5\times$ greater than that used to generate the plots in figure 6.7, so accurately setting the confinement to yield the optimal coupling is not a limiting factor.

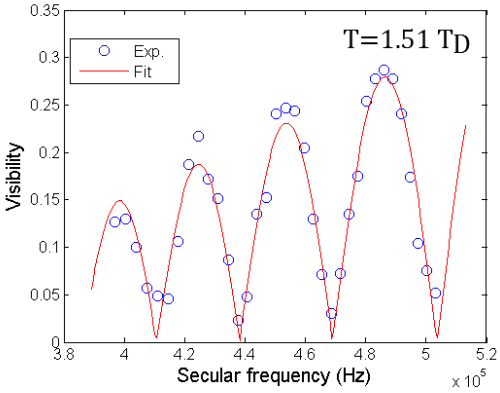

(a) The variation in the combined coupling of 2 ions to the cavity. The inter-ion spacing increases by 433 nm between maxima as the ions are optimally coupled when separated by an integer number of half wavelengths.

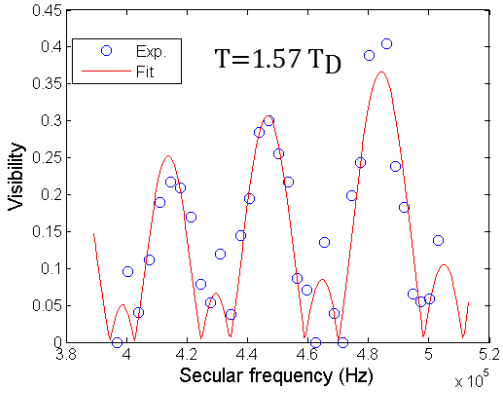

(b) The variation in the combined coupling of 3 ions to the cavity. Large maxima occur where all 3 ions are spaced by an integer number of half wavelengths; subsidiary maxima occur when the outer two ions are separated from the central ion by a half-integer number of half wavelengths.

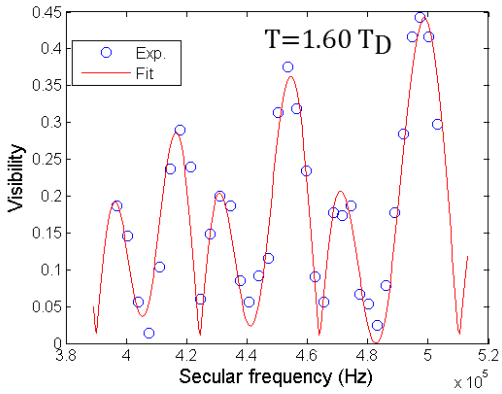

(c) Variation in the coupling of 4-ion strings to the cavity.

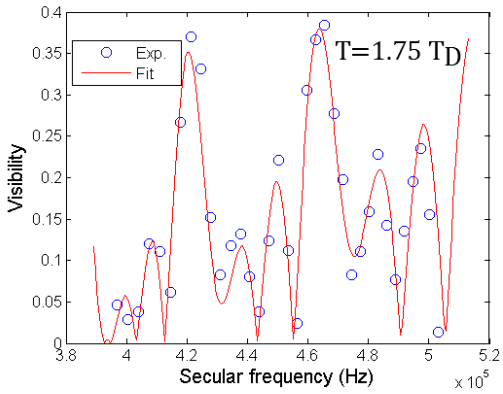

(d) Variation in the coupling of 5-ion strings to the cavity.

Figure 6.7: The variation in coupling of strings of 2-5 ions to the cavity mode as their confinement in the axial direction is changed.

Chapter 7

Conclusions and Outlook

7.1 Conclusion

In this work, a series of optimisations have been implemented to enhance the axial cavity-QED trap in the ITCM group lab at the university of Sussex. Chapter 1 describes the motivation for the project and current state of the field, while chapter 2 introduces the basic theory required. In chapter 3 I describe reconstruction and improvements made to the trap, chapter 4 details the laser and cavity systems used to drive the necessary transitions and act as frequency references, and chapter 5 describes the new controls implemented to enable cooling of the ion to the Doppler limit and precise control over the atomic environment. This enabled a thorough characterisation of the trap and the atom, including a precise measurement of the $^{40}\mathrm{Ca}^{+} S_{\frac{1}{2}} \rightarrow P_{\frac{1}{2}}$ and $P_{\frac{1}{2}} \rightarrow D_{\frac{3}{2}}$ transition wavelengths. Chapter 6 described the combination of the ion trap and cavity systems to explore the realms of cQED, and how to optimise the interaction between the ions and the cavity in frequency and in space.

This work has explored previously uncharted territory in deterministic optimisation of the axial coupling of more than two ions a cavity mode. The theoretical model which predicts the optimal confinement to couple a string of N ions has been confirmed, and the system has proved capable of comfortably being able to achieve the optimal confinement for strings of up to five ions, a strong indication that still longer strings may be coupled with all ions well confined close the cavity antinodes. It has been shown that for ion strings, enhanced localisation of each individual ion may be obtained due to the contribution of higher-order motional modes to the atomic wavefunction. All these factors demonstrate that the axial-trap-cavity design is an extremely attractive candidate for QIP either as a quantum register [13] or as a system for generating multi-ion entangled states by means

of probabilistic measurement-based entanglement schemes.

7.2 Outlook

As the experiment can now deterministically be set up to couple Doppler-temperature ion strings optimally to the cavity, a raft of possible experiments has opened up for novel applications on the way to generating multi-particle entanglement. A pulse scheme for generating single photons has already been implemented and need only be optimised to run the system as a single photon source. The setup can be modified to perform a Hanbury-Brown and Twiss correlation measurement by placing a beamsplitter at the cavity output and using a second APD to monitor the other output port. By applying a magnetic field and selecting an appropriate detuning, a deterministic source of single polarised photons may be produced. This will have applications to experiments in transporting information between optical cavities over a "quantum internet". By inserting a delay-fibre, or driving Raman transitions in two cavity-coupled ions simultaneously, the identicality of produced photons may be measured in a Hong-Ou Mandel measurement.

Single-ion addressing must be implemented to allow individual qubit phase manipulations and measurements. An electro-optic deflector will be used to target the ions. Additional pulse schemes for state preparation and detection will be implemented. Once all this is in place, two-ion probabilistic entanglement may be carried out by placing a polarising beamsplitter on the cavity output and looking for simultaneous detections of cavity photons as described in 2.4.3. The state detection scheme can be used to perform metrology on the ions and allow the fidelity of the entanglement operation to be determined. Once two ions can be repeatably entangled, the operation can be expanded to fuse sets of entangled pairs to generate a cluster state.

The deterministic coupling of many ions to the cavity mode simultaneously also opens up the possibility of performing collective-coupling effects and of using the ion string itself as a reliable storage register for quantum information.

Bibliography

[1] R. P. Feynmann. Simulating Physics with Computers. *Int. J. Theor. Phys.* 21 : 467–488 , 1982.

[2] D. Deutsch. Quantum theory, the Church-Turing principle and the universal quantum computer. *Proc. R. Soc. A.* 400 : 97–117, 1985.

[3] P. W. Shor. Polynomial-time algorithms for prime factorization and discrete logarithms on a quantum computer. *SIAM J. Comput.* 26 : 1484–1509, 1997.

[4] D. S. Abrams. Simulation of Many-Body Fermi Systems on a Universal Quantum Computer. *Phys. Rev. Lett.* 79 : 2586–2589, 1997.

[5] I. Kassala, S. P. Jordan, P. J. Love, M. Mohsenia, and A. Aspuru-Guzika. Polynomial-time quantum algorithm for the simulation of chemical dynamics. *Proc. Natl. Acad. Sci. U.S.A.* 105 : 18681–18686, 2008.

[6] H. J. Briegel, T. Calarco, D. Jaksch, J. I. Cirac, and P. Zoller. Quantum computing with neutral atoms. *J. Mod. Opt.* 47 : 415–451, 2000.

[7] Y. Makhlin, G. Schön, A. Shnirman. Quantum-state engineering with Josephson junction devices. *Rev. Mod. Phys.* 73 : 357–400, 2001.

[8] D. Loss and D. P. DiVincenzo. Quantum computation with quantum dots. *Phys. Rev. A* 57 : 120–126, 1998.

[9] P. F. Herskind, A. Dantan, J. P. Marler, M. Albert, and M. Drewsen. Realization of collective strong coupling with ion Coulomb crystals in an optical cavity. *Nature Physics* 5 : 494–498, 2009.

[10] W. Lange. Cavity QED: Strength in numbers. *Nature Physics* 5 : 455–456, 2009.

[11] J. I. Cirac and P. Zoller. Quantum Computations with Cold Trapped Ions. *Phys. Rev. Lett.* 74 : 4091–4094, 1995.

[12] D. P. DiVincenzo. The Physical Implementation of Quantum Computation *Fortschr. Phys.* 48 : 9–11, 771–783, 2000.

[13] T. Pellizzari, S. A. Gardiner, J. I. Cirac, and P. Zoller. Decoherence, Continuous Observation, and Quantum Computing: A Cavity QED Model. *Phys. Rev. Lett.* 75 : 3788–3791, 1995.

[14] P W. Shor and J. Preskill. Simple Proof of Security of the BB84 Quantum Key Distribution Protocol. *Phys. Rev. Lett.* 85, 441–444, 2000.

[15] P. Walther, K. J. Resch, T. Rudolph, E. Schenck, H. Weinfurter, V. Vedral, M. Aspelmeyer, and A. Zeilinger. Experimental one-way quantum computing. *Nature* 434, 169–176, 2005.

[16] H. J. Briegel and R. Raussendorf. Persistent Entanglement in Arrays of Interacting Particles. *Phys. Rev. Lett.* 86 : 910–913, 2001.

[17] M. Hein, J. Eisert, and H. J. Briegel. Multiparty entanglement in graph states. *Phys. Rev. A* 69 : 062311–062331, 2004.

[18] R. Raussendorf, D. E. Browne, and H. J. Briegel. Measurement-based quantum computation on cluster states. *Phys. Rev. A,* 68 : 022312–022344, 2003.

[19] Y. Li, X. Li, and Y. Nie. Generation of a Five-Atom Cluster State in Cavity QED. *Int. J. Theor. Phys.* 52 : 84–87, 2013.

[20] Y. Li and Y. Nie. Preparation of Six-Atom Cluster State via Cavity Quantum Electrodynamics. *Int. J. Theor. Phys.* 52 : 788–792, 2013.

[21] A. Kuhn, M. Hennrich, and G. Rempe. Deterministic single-photon source for distributed quantum networking. *Phys. Rev. Lett.*, 89 067901–067905, 2002.

[22] J. McKeever, A. Boca, A. D. Boozer, R. Miller, J. R. Buck, A. Kuzmich, and H. J. Kimble. Deterministic generation of single photons from one atom trapped in a cavity. *Science*, 303 : 1992–1994, 2004.

[23] M. K. Keller, B. Lange, K. Hayasaka, W. Lange, and H. Walther. Continuous generation of single photons with controlled waveform in an ion-trap cavity system. *Nature* 431 : 1075–1078, 2004.

[24] C. Russo, H. G. Barros, A. Stute. F. Dubin, E. S. Phillips, T. Monz, T. E. Northup, C. Becher, T. Salzburger, H. Ritsch, P. O. Schmidt, and R. Blatt. Raman spectroscopy of a single ion coupled to a high-finesse cavity. *Appl Phys B* 95 : 205–212, 2009.

[25] M. Albert, J. P. Marler, P. F. Herskind, A. Dantan, and M. Drewsen. Collective strong coupling between ion Coulomb crystals and an optical cavity field : Theory and experiment. *Phys. Rev. A,* 85 : 023818–023831, 2012.

[26] B. Casabone, A. Stute, K. Friebe, B. Brandstätter, K. Schüppert, R. Blatt, and T. E. Northup. Heralded Entanglement of Two Ions in an Optical Cavity. *Phys. Rev. Lett.* 111 : 100505–100510, 2013.

[27] A. Kuhn and D. Ljunggren, Cavity-based single-photon sources, *Contemporary Physics*, 51 : 289–313, 2010.

[28] J. R. Kuklinski, U. Gaubatz, F. T. Hioe, and K. Bergmann. Adiabatic population transfer in a three-level system driven by delayed laser pulses. *Phys. Rev. A*, 40: 6741–6744, 1989.

[29] L. S. Brown and G. Gabrielse. Geonium theory : Physics of a single electron or ion in a Penning trap. *Rev. Mod. Phys.* 58 : 233–311, 1986.

[30] E. L. Raab, M. Prentiss, Alex Cable, Steven Chu, and D. E. Pritchard. Trapping of Neutral Sodium Atoms with Radiation Pressure. *Phys. Rev. Lett.* 59 : 2631–2634, 1987.

[31] D. Leibfried, R. Blatt, C. Monroe, and D. Wineland. Quantum dynamics of single trapped ions. *Rev. Mod. Phys.* 75 : 281–324, 2003.

[32] S. Earnshaw. On the Nature of the Molecular Forces which Regulate the Constitution of the Luminiferous Ether. *Trans. Camb. Phil. Soc.* 7 : 97–112, 1842.

[33] G. W. Hill. On the part of the motion of the lunar perigee which is a function of the mean motions of the sun and moon. *Acta math.* 8 : 1–36, 1886.

[34] D. M. Lucas, A. Ramos, J. P. Home, M. J. McDonnell, S. Nakayama, J. P. Stacey, S. C. Webster, D. N. Stacey, and A. M. Steane. Isotope-selective photionization for calcium ion trapping. *Phys. Rev. A*, 69: 012711–012724, 2004.

[35] M. A. Wilson. Quantum State Control of a Single Trapped Strontium Ion. PhD Thesis, The University of Strathclyde, 2001.

[36] R. Raußendorf. Measurement-based quantum computation with cluster states. PhD Thesis, Ludwig-Maximilians-Universität München, 2003.

[37] F. T. Arecchi and R. Bonifacio. Theory of Optical Maser Amplifiers. *IEEE J. Quantum Electron* 1 : 169–178, 1965.

[38] D. Crick. Manipulation of Ca+ Ions in Penning Traps. PhD Thesis, Imperial College London, 2009.

[39] Y. Wu. Effective Raman theory for a three-level atom in the Λ configuration. *Phys. Rev. A* 54 : 1586–1592, 1996.

[40] C. Russo. Photon statistics of a single ion coupled to a high-finesse cavity. PhD Thesis, Leopold-Franzens-Universität Innsbruck, 2008.

[41] E.T. Jaynes and F.W. Cummings. Comparison of quantum and semiclassical radiation theories with application to the beam maser. *Proc. IEEE,* 51 : 89–109 1963

[42] C. K. Law and H. J. Kimble. Deterministic generation of a bit-stream of single-photon pulses. *J. Mod. Opt.* 44 : 2067–2074, 1997.

[43] H. G. Barros, A. Stute, T. E. Northup, C. Russo, P. O. Schmidt and R. Blatt. Deterministic single-photon source from a single ion. *New J. Phys.* 11: 103004-103014, 2009.

[44] A. Stute, B. Casabone, B. Brandstätter, K. Friebe, T. E. Northup and R. Blatt. Quantum-state transfer from an ion to a photon. *Nature Photonics* 7: 219–222, 2013.

[45] L. M. Duan and H. J. Kimble. Efficient Engineering of Multiatom Entanglement through Single-Photon Detections. *Phys. Rev. Lett.* 90, 253601–253605, 2003.

[46] N. R. Seymour-Smith. Ion-trap cavity QED system for probabilistic entanglement. PhD Thesis, University of Sussex, 2011

[47] K. T. Sheridan. Experimental Techniques for Cold Chemistry and Molecular Spectroscopy in an Ion Trap. PhD Thesis, University of Sussex, 2012

[48] N. Seymour-Smith, P. Blythe, M. K. Keller, and W. Lange. Fast scanning cavity offset lock for laser frequency drift stabilization. *Rev. Sci. Instrum.,* 81 : 075109–075114, 2010.

[49] R. W. P. Drever, J. L. Hall, F. V. Kowalski, J. Hough, G. M. Ford, A. J. Munley, and H. Ward. Laser phase and frequency stabilization using an optical resonator. *Appl. Phys B,* 31 : 97–105, 1983.

[50] D. F. V. James. Quantum dynamics of cold trapped ions with application to quantum computation. *Appl. Phys B,* 66 : 181–190, 1998.

[51] D. J. Berkeland, J. D. Miller, J. C. Bergquist, W. M. Itano, and D. J. Wineland. Minimization of ion micromotion in a Paul trap. *J. Appl. Phys,* 83 : 5026–5033, 1998.

[52] W. Hanle. The magnetic influence on the polarization of resonance fluorescence. *Z. Physik* 30 : 93–99, 1924

[53] J. Alnis, K. Blushs, M. Auzinsh, S. Kennedy, N. Shafer-Ray, and E. R. I. Abraham. The Hanle effect and level crossing spectroscopy in Rb vapour under strong laser excitation. *J. Phys. B: At. Mol. Opt. Phys.* 36 : 1161–1173, 2003.

[54] D. W. Preston. Doppler-free saturated absorption: Laser spectroscopy. *Am. J. Phys.* 64 : 1432–1436, 1996.

[55] G. Janik, W. Nagourney, and H. Dehmelt. Doppler-free optical spectroscopy on the Ba^+ mono-ion oscillator. *J. Opt. Soc. Am. B*, 2 : 1251–1257, 1985.

[56] M. Keller, B. Lange, K. Hayasaka, W. Lange, and H. Walther. Deterministic coupling of single ions to an optical cavity. *Appl. Phys. B* 76 : 125–128, 2003.